



TAMPEREEN TEKNILLINEN YLIOPISTO
TAMPERE UNIVERSITY OF TECHNOLOGY

Alba Ávalos del Río

Experimental Testing and Characterization of High Velocity Impacts on Novel Ultra High Strength Steels

Master's thesis

Examiners: Associate Professor Pasi Peura
Postdoctoral Researcher Matti Isakov

The examiner and topic of the thesis
were approved by the Council of the
Faculty of Engineering Science on
May 6th 2015

ABSTRACT

TAMPERE UNIVERSITY OF TECHNOLOGY

ALBA AVALOS DEL RIO: Experimental testing and characterization of high velocity impacts in novel ultra high strength steels

Master of Science Thesis, 88 pages

May 2015

Major subject: Mechanical Engineering

Examiner: Associate Professor Pasi Peura, Dr. Matti Isakov

Keywords: Ultra High Strength Steel, impact wear, strain rate, adiabatic shear band, work hardening

The main aim of this work was to study the performance against high velocity impacts of two novel ultra high strength steels. Different impact velocities and testing conditions were studied to recreate the actual working environment. Lubrication and low temperature tests were performed and compared to dry-conditions impact testing. The effect of surface work hardening taking place during service was studied as well.

Mechanical behavior of the materials was studied at strain rates ranging from 10^{-3} to 3600 s^{-1} using a quasi-static testing machine and the Split Hopkinson Pressure Bar technique. High velocity impact tests were performed at different conditions using spherical projectiles at different velocities for a constant impact angle of 30° . The influence of impact energy and environmental conditions were studied. Wear was analyzed based on volume loss taking into consideration also the material plastically deformed and cut-off from the surface through the cutting-to-plasticity ratio. The energy dissipated during the impact was also studied. Characterization of the impact craters and their cross-sections was performed to identify failure and damage mechanisms.

Impact wear was found to be strongly dependent on impact energy and testing conditions. Higher impact energies lead to higher wear rates likely caused by the appearance of adiabatic shear bands. Lubrication was observed to lead to higher volume loss due to more material cut-off from the surface instead of plastically deformed. Work hardening prior to testing produced an increase of hardness of 45-80 %, which resulted in a decrease of wear rate except in the case of the highest impact velocities. Adiabatic shear bands were more present on dry-impact testing than in any other type of test case.

PREFACE

The work presented in this thesis was carried out at the Tampere Wear Center, Department of Material Science, Tampere University of Technology, during the years 2014-2015, under the guidance of the Associate Professor Pasi Peura.

I am deeply grateful to Dr. Kati Valtonen and Professor Pasi Peura for proposing me this interesting research subject and giving me the chance to finish my studies in Finland in a motivational environment.

Also, I would like to express my deepest gratitude to M. Sc. Matti Lindroos and M. Sc. Marian Apostol for helping from the beginning to the end of this project, for their guidance, their advices and the fruitful discussions. Without them working with me, this project could have never been possible.

I also would like to thank Dr. Matti Isakov for his help, his advice and all the valuable information receive from him.

Dr. Mikko Hokka deserves my gratitude for the construction and update of the work hardening device for the High Velocity Particle Impactor samples.

All the colleagues working at the Department of Material Science are acknowledged for being always available to help and for creating a great atmosphere in which it is a pleasure to work.

My deepest gratitude is to my parents, Alicia and Alberto, and my family, who have supported and encouraged me throughout my whole life, making my benefit always a priority. Special thanks to Alejandro, for his love, his encouragement and for making easier every path I take. My school friends, Julia and my two Martas, and my home university friends deserve my thanks as well, because even in the distance I can feel their love and support. Finally, I want to express my gratitude to all the friends I have made in Finland, for becoming my family and making me feel home being so far.

Tampere, May 2015

Alba Ávalos del Río

CONTENTS

ABSTRACT.....	i
PREFACE	ii
CONTENTS.....	iii
LIST OF SYMBOLS AND ABBREVIATIONS.....	v
1. INTRODUCTION	1
2. INFLUENCE OF STRAIN RATE AND TEMPERATURE ON THE MECHANICAL BEHAVIOR OF METALS	3
2.1. Thermally activated dislocation motion.....	5
2.2. Dislocation drag.....	7
3. IMPACT WEAR ON METALS AND INFLUENTIAL PROPERTIES.....	8
3.1. Solid particle erosion on ductile metals	9
3.1.1. <i>Influence of particle properties on impact wear</i>	10
3.1.2. <i>Influence of operating parameters on impact wear</i>	11
3.1.3. <i>Influence of microstructure and properties of the target material on impact wear.....</i>	12
3.2. Adiabatic shear bands	13
3.2.1. <i>Qualitative description</i>	13
3.2.2. <i>Metallurgical aspects</i>	14
3.2.3. <i>Elemental constitutive model.....</i>	16
4. MARTENSITIC WEAR STEEL	19
4.1. Martensite : microstructure and mechanical properties.....	20
4.1.1. <i>Martensitic transformation.....</i>	20
4.1.2. <i>Morphologies of martensitic microstructures.....</i>	22
4.2. Manufacturing of wear resistance steels	23
4.2.1. <i>Hot Rolling</i>	24
4.2.2. <i>Direct quenching</i>	25
5. METHODS OF MATERIAL TESTING AT DIFFERENT STRAIN RATES	27
5.1. Split Hopkinson Pressure Bar system	29
5.1.1. <i>Description of the Split-Hopkinson Pressure Bar technique</i>	29
5.1.2. <i>Description of the Split Hopkinson Pressure Bar equipment at TUT</i>	30

5.1.3.	<i>Theory of the Split-Hopkinson Pressure Bar</i>	32
5.1.4.	<i>Dispersion of elastic waves</i>	37
5.1.5.	<i>Effect of specimen geometry</i>	39
5.2.	High Velocity Particle Impactor system	41
5.2.1.	<i>Description of the HVPI equipment at TUT</i>	41
5.2.2.	<i>Crater characterization</i>	42
6.	EXPERIMENTAL PROCEDURES	43
6.1.	Test materials	44
6.2.	Quasi-static compression testing	45
6.2.1.	<i>Sample preparation</i>	45
6.2.2.	<i>Test procedure</i>	45
6.3.	Split-Hopkinson Pressure Bar system	47
6.3.1.	<i>Sample preparation</i>	47
6.3.2.	<i>Test procedure</i>	47
6.4.	High Velocity Particle Impactor	48
6.4.1.	<i>Sample preparation</i>	49
6.4.2.	<i>Test procedure for dry tests</i>	49
6.4.3.	<i>Test procedure for oil layer tests</i>	51
6.4.4.	<i>Test procedure for work hardened tests</i>	52
6.4.5.	<i>Test procedure for -20°C tests</i>	58
6.4.6.	<i>Profiling and crater characterization</i>	58
7.	RESULTS AND DISCUSSION	60
7.1.	Mechanical behavior results and strain rate dependence	60
7.1.1.	<i>Compressive properties</i>	60
7.1.2.	<i>Impact testing</i>	63
7.2.	Damage and failure mechanisms	71
7.2.1.	<i>Compression testing</i>	71
7.2.2.	<i>Impact testing. Cross-sectional study</i>	72
7.2.3.	<i>Impact testing. Crater three-dimensional study</i>	78
8.	CONCLUSIONS	81
9.	REFERENCES	84

LIST OF SYMBOLS AND ABBREVIATIONS

A	Cross sectional area of the bar of the SHPB
A_n	Coefficient in the Fourier transformation
A'_n	Modified coefficient in the Fourier transformation
A_S	Cross sectional area of the specimen used in SHPB
B_n	Coefficient in the Fourier transformation
B'_n	Modified coefficient in the Fourier transformation
b	Burgers vector of a dislocation
c	Specific heat capacity
C_f	Wave velocity in the pressure bar at the fundamental frequency
C_n	Phase velocity of frequency component n
C_0	Longitudinal elastic wave velocity
C_V	Heat capacity
d_0	Reference displacement of the spring during work hardening
d_i	Displacement registered by the tensile testing machine during work hardening
d_s	Diameter of the specimen for SHPB
E	Young's modulus
F_0	Force registered by tensile testing machine at the initial moment of work hardening
F_1	Existing force at the incident bar in SHPB
F_2	Existing force at the transmitted bar in SHPB
F_a	Actual force applied against the sample during work hardening
F_C	Compression force
F_m	Force measured by tensile testing machine during work hardening
F_s	Spring force (Hooke's Law)
k_s	Spring constant (Hooke's Law)
kT	Thermal energy provided by the thermal vibration of the atoms
L_s	Length of the specimen for SHPB
p_B	Probability that a dislocation has enough thermal energy to overcome a thermal obstacle
t_r	Running time of a dislocation
t_w	Waiting time of a dislocation
u	Displacement
u_1	Displacement of the end of the incident bar in SHPB

u_2	Displacement of the end of the transmitted bar in SHPB
u_i	Displacement of the incident wave in SHPB
u_r	Displacement of the reflected wave in SHPB
u_t	Displacement of the transmitted wave in SHPB
v_1	Particle velocity in the incident bar in SHPB
v_2	Particle velocity in the transmitted bar in SHPB
ν_s	Poisson's ratio in the specimen of SHPB testing
\bar{v}	Average velocity of a dislocation
t	Time
T	Temperature
T_0	Initial temperature
T_c	Critical temperature
T_m	Melting point
W	Work
x_0	Initial deformation suffered by the spring during work hardening
x_s	Deformation suffered by the spring (Hooke's Law)
z	Distance between the strain gage and specimen in SHPB
ΔG	External energy needed for a dislocation to overcome a thermal obstacle
ΔT	Temperature increase
$\Delta \sigma$	Increase in stress
β	Fraction of mechanical energy transformed into heat
ε	Strain
ε_1	Strain at the incident bar in SHPB
ε_2	Strain at the transmitted bar in SHPB
ε_i	Strain of the incident wave in SHPB
ε_r	Strain of the reflected wave in SHPB
ε_t	Strain of the transmitted wave in SHPB
ε_c	Critical strain for shear band formation
ε_E	Engineering strain
ε_T	True strain
$\dot{\varepsilon}$	Strain rate
ρ	Density
ρ_m	Density of mobile dislocations
τ	Shear stress
τ^*	Thermal part of the flow stress
τ_A	Athermal part of the flow stress
τ_T	Shear stress at temperature T
τ_{T0}	Shear stress at initial temperature

σ	Stress
σ_E	Engineering stress
σ_T	True stress
φ	Phase shift
ω	Fundamental frequency
Av.	Average
BCC	Body-Centered Cubic
BCT	Body Centered Tetragonal
BM	Bulk material
CCT	Continuous Cooling Transformation
DASB	Deformed Adiabatic Shear Band
DM	Deformed Matrix
FCC	Face-centered cubic
FFT	Fourier transformation
HCP	Hexagonal Closed Packed
HVPI	High Velocity Particle Impactor
IT	Isothermal Transformation
M_s	Martensite start temperature
M_f	Martensite finish temperature
RT	Room Temperature
SEM	Scanning Electron Microscope
SHPB	Split Hopkinson Pressure Bar
TASB	Transformed Adiabatic Shear Bands
TUT	Tampere University of Technology
TWC	Tampere Wear Center
UHSS	Ultra High Strength Steel
WH	Work hardened
WSL	White Surface Layer

1. INTRODUCTION

A large number of materials are continuously developed to withstand different types of loadings. In the mining, construction and heavy machinery context, the development of materials with enhanced properties against impact and abrasion loads has lately become a priority. High Strength Steels have been widely studied and used for wear resistance applications. A step forward has been taken with the appearance of a new generation of Ultra High Strength Steels (UHSS). UHSS are characterized by a good balance of strength, toughness and ductility, combined with an enhanced wear resistance. These properties are the result of an adequate chemical composition, in combination with an accurate control of the manufacturing process. UHSS are commonly obtained by quenching followed by tempering. However, direct quenching (DQ) is starting to be used as a more effective alternative process, leading to UHSS with superior properties. DQ consists on cooling down the steels right after hot rolling. Controlling the final rolling temperature and time before cooling starts, it is possible to cool the steel down within the non-recrystallization region, which results in better mechanical properties. [1]. UHSS have been proved to have excellent properties under solid particle impacts at laboratory scale [2]. However, more studies need to be performed to achieve a further understanding of their mechanical behavior as well as damage and failure mechanisms under different loading conditions.

Moreover, the real working conditions of the wear resistant materials can vary considerably in terms of working temperature, presence of lubrication and even work hardening of the surface after some operation time. Those aspects can remarkably affect the mechanical properties and wear rate. A large number of studies regarding impact wear have been performed in “normal” conditions, such as room temperature with the material in its original state. [3, 4] . However, it is crucial to understand how material’s behavior is influenced by changes in its environment.

In this work, a theoretical basis on solid particle erosion is presented, based on studies made by Zum-Gahr. [5, 6]. As the impacts involve high amounts of energy, the material is exposed to high strain rates. Therefore, it is also important to understand the influence of strain rate on the mechanical behavior of the test materials. High strain rate deformation can lead to the formation of the so-called adiabatic shear bands (ASB), due to the insufficient transfer of generated heat away from the deforming material. ASBs are considered as precursors to failure and lead to higher levels of wear rate since microcracks are likely to grow within them.

Studies performed on solid particle erosion are usually based on particles of very small size. [7, 8, 9]. However, in this current work the projectiles used for the high velocity impacts were spheres of 9 mm diameter. The larger particle size was used for several reasons. Firstly, larger particles enable recording the impact with a high speed camera. By post-processing of the images, more information regarding the energy involved in the impact can be obtained. Secondly, larger impinging particles produce larger craters allowing better characterization of the surface dent. Wear rates produced by an oblique impact are influenced by several factors, such as impact angle, impact velocity as well as size, hardness and angularity of the impacting particle. The effect of impact angle has been found to be a strong influence, since the amount of energy consumed in deforming the material depends on it. [3]. Impact velocity is, as expected, another of the parameters of impact wear.

Wear has been usually characterized by volume loss. In the current study, wear was determined through a study of volume loss in combination with the results regarding the energies involved in the impact. One of the most important parameters in studying damage caused by an impacting particle is the cutting-to-plasticity ratio. [5] This ratio allows determining the amount of material that has been removed from the surface and that the amount that has been deformed. The study of the cross sections of the craters gives information on the damage mechanisms, resulting in a better understanding of the material behavior.

In the current work, two different novel ultra high strength steels were tested using a High Velocity Impactor (HVPI) equipment to study their impact resistance. Four different working conditions were simulated in a controlled environment: room temperature tests, tests in lubricated conditions, work hardening of the surface prior to testing and tests at -20°C. Each series of tests were performed for 4 different impacts velocities.

2. INFLUENCE OF STRAIN RATE AND TEMPERATURE ON THE MECHANICAL BEHAVIOR OF METALS

Plastic deformation of a material is a permanent deformation as a result of an applied stress, and it has a strong influence on its mechanical properties, such as strength or hardness. Most of metals commonly deform by slipping and/or twinning.

Slip is the process that causes plastic deformation due to dislocation motion. A dislocation is a defect present in a material due to the misalignment of some atoms within a certain line, termed as dislocation line. There are two types of dislocations, edge and screw, both presented in Figure 1. However, many dislocations are considered as mixed, since both types of components are present. Figure 2 presents a schematic of the dislocation motion. When a shear stress is applied, an edge dislocation moves within a direction parallel to the stress, while screw ones have a motion perpendicular to the stress direction. However, the amount and direction of plastic deformation caused by both dislocation types is the same. The mechanical properties of the materials are strongly affected by the characteristics of the dislocations, such as their mobility and their ability to multiply. Those aspects are affected by the strain fields present around the dislocation line. Due to the presence of different amount of adjacent atoms around the dislocation line, some regions with compressive, tensile or shear strains appear. The magnitude of the strain decreases with squared distance. Adjacent dislocations, with their strain regions close enough, can interact by attracting or repulsing each other, mechanism that has a great influence on strengthening of the materials. [10]

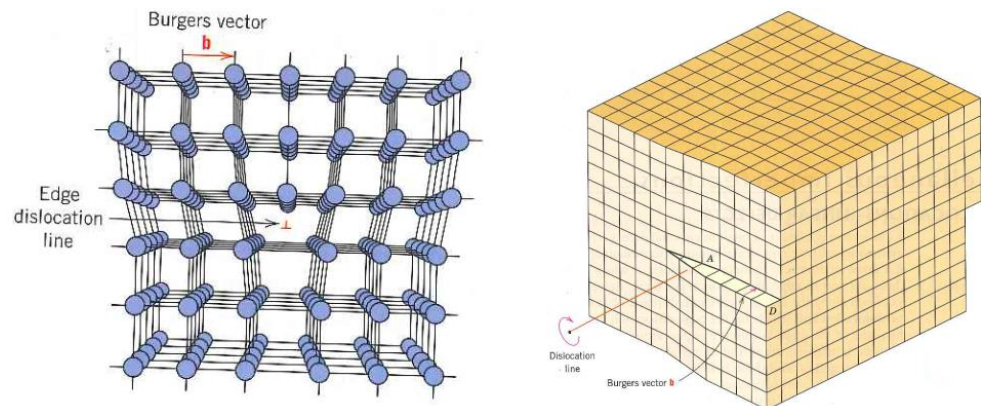


Figure 1. Schematic of an edge and screw dislocation. [10]

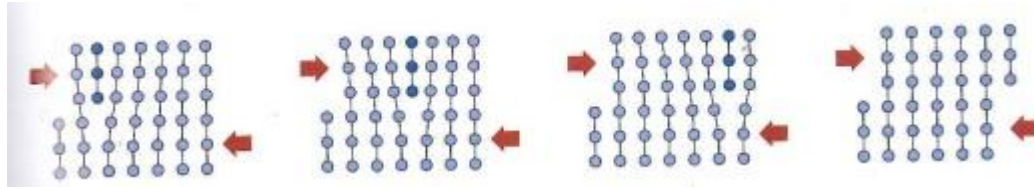


Figure 2. Schematic of dislocation motion. [10]

However, the movement of dislocations is partially blocked by obstacles, such as other dislocations, grain boundaries, vacancies or inclusions. To overcome those obstacles energy is required, which can be provided by an externally applied stress and/or by the internal thermal vibration of the atoms. Sometimes both energy sources can contribute together to dislocation motion.

In a material, two different types of obstacles can be found, thermal and athermal obstacles. In the case that the temperature of the material is high enough, thermal or short range obstacles can be overcome only by thermal energy, without external stress. However, athermal or long-range obstacles need a bigger energy to be overcome, which has to be supplied by externally applied stress. According to Isaac and Granato [11], there are three different regions of material behavior regarding the kind of obstacles that limit the movement of dislocations. In the first region, at low and intermediate strain rates, the flow stress needed is low and it increases only moderately with increasing strain rate. Thus, below 10^3 s^{-1} strain rate, part of the energy needed for dislocation motion can be provided by thermal energy. Therefore, this region is known as thermally activated dislocation motion. For strain rates higher than 10^3 s^{-1} , the flow stress required increases more rapidly with increasing strain rate. Hence the dislocation motion becomes drag controlled and considerable increase in the stress needed to maintain a high dislocation velocity. Finally, there is a third region for even higher strain rates, in which dislocation velocity is near that of the transverse sound wave. Figure 3 illustrates the strain rate dependence of flow stress on an AISI 304 stainless steel. [12, 13, 14].

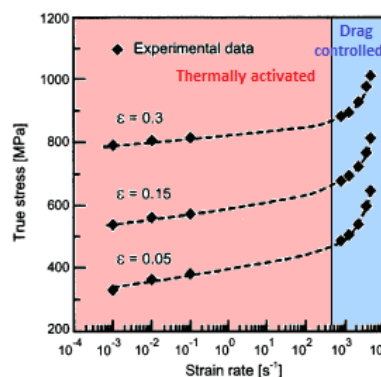


Figure 3. Dependence on strain rate of the flow stress of AISI 304 stainless steel. [15].

As mentioned, also twinning contributes to plastic deformation. Twinning occurs when atoms are displaced to a mirror-image position of atoms on the other side of a certain plane named as twin boundary, as shown in Figure 4. The motion of the atoms occurs following a specific direction and within a crystallographic plane, and it results in a reorientation of the atoms. Usually, plastic deformation caused by twinning is not great compared to that caused by slipping. However, twinning becomes especially important in metals with BCC structures at low temperatures and under shock loading, which involves high strain rates. In those conditions slipping is limited due to very few slip systems available. Twinning may also reorient the atoms in a way that slipping can occur more easily. [10]

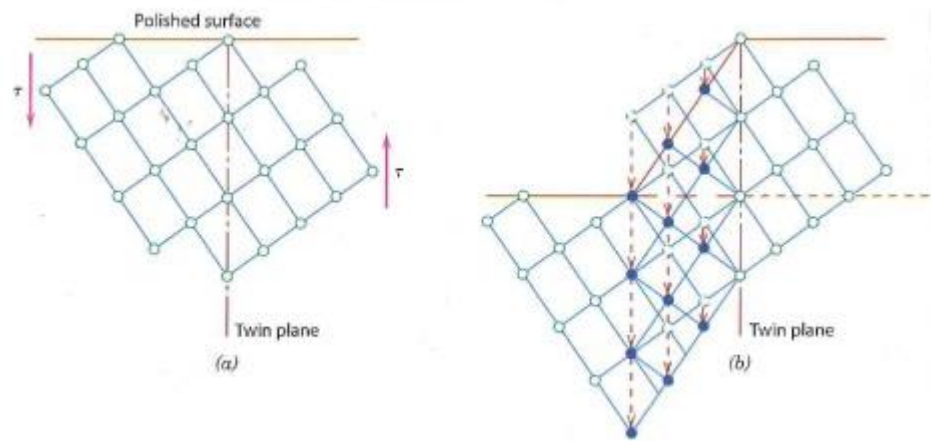


Figure 4. Schematic of twinning mechanism. [10]

2.1. Thermally activated dislocation motion

The external flow stress required to maintain the plastic flow can be divided into two components, the thermal part of the stress τ^* and the athermal one, τ_A . Equation 1 shows the expression of the flow stress.

$$\tau = \tau^* + \tau_A \quad (1)$$

Figure 5 shows the temperature and strain rate dependence of the flow stress. As it can be observed, the thermal component of the flow stress is the difference between the flow stress at 0 K and at any temperature. As the temperature increases the thermal component decreases, and becomes zero at a certain temperature, named as critical temperature T_c , which depends on the strain rate. When T_c is reached all the thermal obstacles can immediately be overcome by the thermal energy, without any external stress. Consequently

all the remaining obstacles are athermal. Below T_c the amount of thermal energy is not enough to overcome by itself all the thermal obstacles. In that case, an extra external applied stress is needed. Therefore, above T_c the external applied stress is only necessary to overcome the athermal obstacles that thermal energy cannot surmount because of their nature. As it is also shown in Figure 5, when strain rate increases, the critical temperature increases as well. [12, 13].

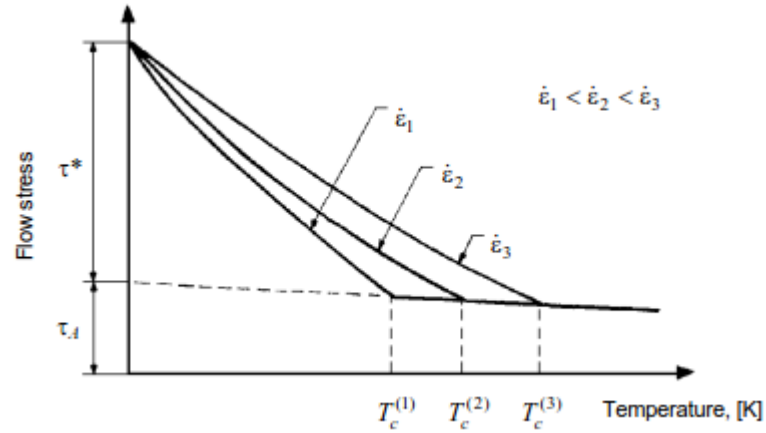


Figure 5. Temperature and strain dependence of the flow stress. [16].

When a dislocation encounters a thermal obstacle, it stops in front of it waiting to have enough thermal energy to overcome it. Thermal activation is a probability process that depends on the extra energy needed to overcome the obstacle ΔG and the thermal energy provided by the vibrations of the atoms, kT . The probability p_B that the thermal energy is high enough to surmount the obstacle is expressed in equation 2:

$$p_B = e^{-\frac{\Delta G}{kT}} \quad (2)$$

The waiting time t_w in front of the obstacle depends on p_B . Usually this waiting time is notably larger than the running time t_r , i.e., the time that the dislocation spends travelling between obstacles. Higher values of external stress result in less extra energy required (ΔG becomes smaller). Therefore, higher values of external stress lead to higher probabilities to overcome the obstacle and less waiting time. Strain rate is related to the velocity of dislocations as it can be observed in equation 3, where ρ_m is the density of mobile dislocations, b is the Burgers vector of the dislocation and \bar{v} is the average velocity of the dislocation.

$$\dot{\epsilon} = \rho_m b \bar{v} \quad (3)$$

Therefore, high strain rates lead to higher dislocation velocities and less waiting time to overcome obstacles and consequently to higher stresses, as it can be observed in Figure 6. For the highest external stress σ_2 the dislocations need less waiting time to overcome the obstacles than for lower external stresses, such as σ_1 . [12, 16].

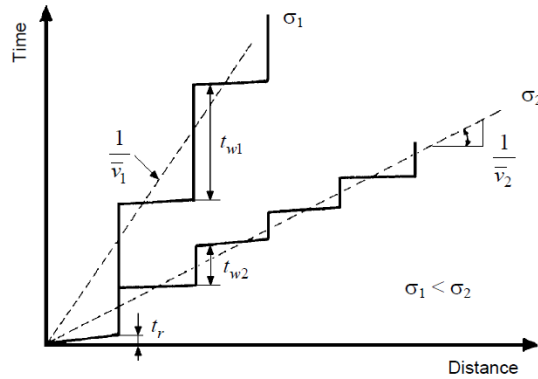


Figure 6. Distribution of running and waiting times for a dislocation at two stress levels. [16].

2.2. Dislocation drag

For strain rates higher than about 10^3 s^{-1} , an “upturn” appears in the flow stress – strain rate curve, as it can be observed in Figure 3. This effect is due to the so-called viscous drag mechanisms, which interferes with dislocation motion reducing the velocity of the dislocations. One explanation for this phenomenon is that these mechanisms act simultaneously with the thermal obstacles dissipating energy of the dislocations. Consequently more energy is needed to keep the same flow rate. The main mechanisms are designated as phonon and electron viscosity. Phonon drag dominates at room temperature and consists of the emission of sound waves as a result of the frictional force, which accelerates and decelerates the dislocations dissipating part of their kinetic energy. At very low temperatures, electron viscosity, which consists of electron emissions, has more importance. There is also a minor effect, termed as thermoelastic effect, which converts acoustic energy into thermal. [12, 13].

3. IMPACT WEAR ON METALS AND INFLUENTIAL PROPERTIES

Wear is a phenomenon that results in material loss and/or surface damage. Figure 7 illustrates the four main wear modes, known as adhesive, abrasive, fatigue and corrosive wear. Due to changes in the properties and the response of the material the main wear mode can change. Each wear mode is caused by to different wear mechanisms and, commonly, more than one mechanism acts simultaneously. Adhesive wear occurs when two surfaces in contact have relative motion. If high pressure is present in the contact, junctions form in between the surfaces. As a result of the relative motion the junctions break and some material is transferred from one material to the other. Abrasion is caused by hard particles present between two surfaces with relative motion. The difference of hardness between the materials and the particles strongly influences the wear rate. Fatigue occurs when a repeated loading is applied against a surface. It results in crack formation and material removal in form of flakes. Finally, corrosive wear or tribomechanical reaction occurs when the surfaces in contact react with the environment. While abrasive and adhesive wear occur when plastic deformation takes place in the contact, fatigue and corrosive wear can take place under any conditions, i.e., without the need of notable plastic deformation. The amount of volume loss and the change in the state of the surface such as roughness or the amount of cracks, is used to evaluate the amount of wear produced. Impact wear, which is produced by high speed particles impacting the surface, can be studied like abrasive wear due the similarity of the wear mechanisms that both involve. [6, 17]

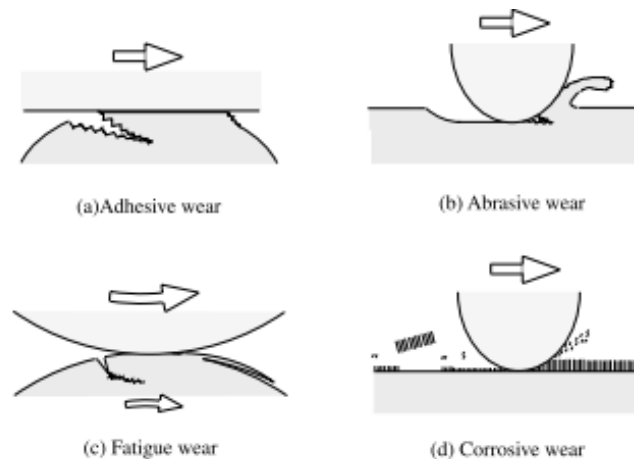


Figure 7. Schematic of main wear modes. [17]

3.1. Solid particle erosion on ductile metals

Solid particle erosion is produced by the impact of accelerated particles against the surface of a material, causing volume loss in it. The amount of material removed from the surface depends not only on the target material and particle characteristics, but also on some operating parameters, such as impact angle and velocity. In particle erosion there are different mechanisms involved that lead to wear, as it is shown in Figure 8. When a particle reaches a surface, some material is displaced to the sides and to the front due to deformation, a mechanism termed as ploughing, illustrated in Figure 8 (a). Different impact angles of the particle produce different levels of deformation and, therefore, different amounts of material are displaced. Figure 8 (b) shows some cracks produced on the surface as a result of an impact. As impact angle, particle size or particle velocity increases, surface cracking becomes more significant. Impacts also extrude some material at the exit end of the craters, forming the so-called pile-up region (Figure 8 c). According to Winter et al. [18, 19], in the pile-up region the localized strain is very high, leading to an increase of temperature, which results in formation of adiabatic shear bands below the surface. Consequently, higher volume losses are caused. In the moment of the impact, there is also some friction in the interface between the projectile and the target material due to their roughness. [5, 20].

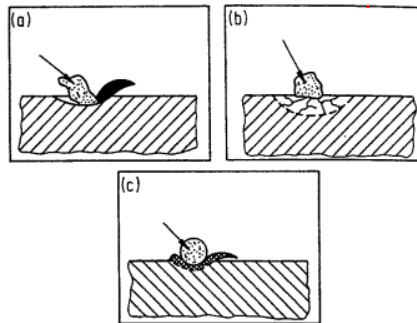


Figure 8. Processes that lead to volume loss due to a single impact of a particle: (a) ploughing, (b) surface cracking and (c) extrusion of material at the exit end of impact craters. [5]

Wear during multiple impacts of particles on the surface involves, additionally, some other mechanisms, which are illustrated in Figure 9. Figure 9 (a) shows how after multiple impacts a large number of cracks appear both on the surface and subsurface of the material. Cracking in combination with extrusion, as shown in Figure 9 (b), results in the formation of thin platelets that are removed from the surface.

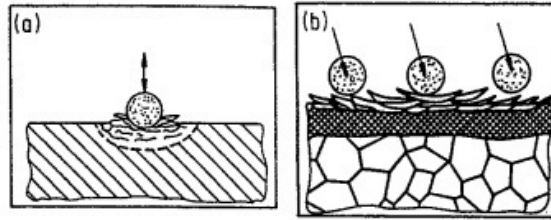


Figure 9. Processes that lead to volume loss due to multiple particle impacts: (a) surface and subsurface fatigue cracks, (b) formation of platelets due to extrusion and forging. [5].

3.1.1. Influence of particle properties on impact wear

Wear is highly influenced by the type of particle impacting the surface. Properties such as size, angularity or difference of hardness between the particle and the target material are decisive for volume loss. Figure 10 shows the wear produced as a function of the ratio of hardness of the particle and hardness of the target material for single-phase and multiphase particles. This graphic corresponds to the behavior of the material under abrasive wear. However, for erosion wear the tendency can be considered very similar. Wear increases abruptly when the hardness of the contacting materials become equal (ratio equal 1), and it keeps on increasing until the hardness of the particle is about 1.2 times the hardness of the material. [5].

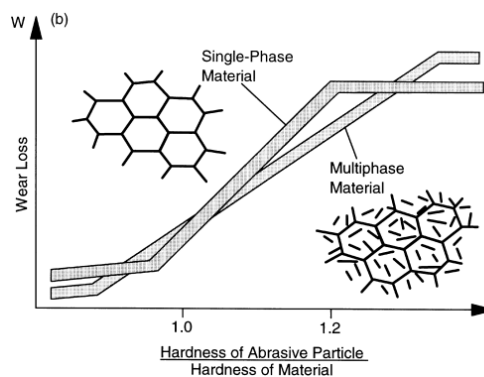


Figure 10. Wear vs particle hardness and phase to surface hardness ratio. [6].

As the size of the impacting particles increases, impact energy becomes higher, leading to higher levels of volume loss. Figure 11 illustrates the tendency of the erosion rate as a function of the particle size. Erosion rate is defined as the volume loss produced in a material divided by the mass of the impacting particle. Ductile materials are less affected

by impacting particle size than brittle ones. However, they also suffer higher volume losses as the particle size increases. This effect is more remarkable in the case of hard metals. Finally, also the shape or angularity of the particle has a significant influence. In general, for the same particle size, angular particles cause more volume loss than spherical particles. [5, 6].

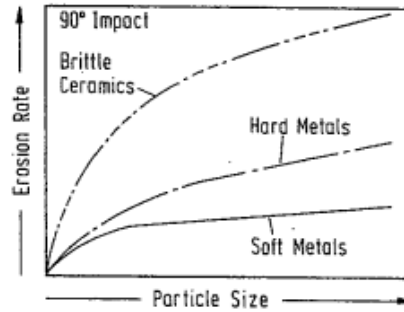


Figure 11. Erosion rate as a function of particle size. [5]

3.1.2. Influence of operating parameters on impact wear

Volume loss is also significantly influenced by parameters such as impact angle and impact velocity. The dependence of volume loss on the impact velocity, v , can be expressed as:

$$Vol = k * v^n \quad (4)$$

where k is a constant and n , is the velocity exponent. According to Finnie et al. [21], for ductile materials, mass loss is approximately proportional to the square of the impact velocity ($n=2$), as it can be observed in Figure 12 (a). Zum-Gahr [6] points out that velocity exponent for ductile materials ranges from 2 to 3, while for brittle materials it is higher (3-4). Impact velocity has a remarkable influence because impact energy is strongly dependent on it. Increase in impact velocity, leads to a square increase in impact energy and, therefore, similar increase in volume loss. Regarding impact angle, Figure 12 (b) shows its influence for different types of materials. The influence of the impact angle depends also on the parameters mentioned above. As it can be observed, for ductile metals volume loss is maximum for angles of about 30° or less. For bigger angles, volume loss decreases as the angle increases. By contrast, for brittle materials, higher impact angles lead to higher volume losses, being maximum for 90°. [5, 6].

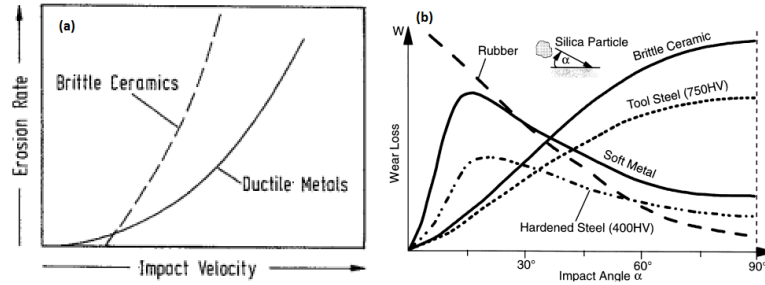


Figure 12. Erosion rate as a function of (a) impact velocity [5] and (b) impact angle. [6].

3.1.3. Influence of microstructure and properties of the target material on impact wear

Properties of the target material such as hardness, work hardening and capability of deformation, have a strong influence on impact wear characteristics. According to Finnie et al. [22], an increase in the hardness of the target material results also in an increase in the erosion resistance. In Figure 13 it is illustrated that the relation between hardness and erosion resistance is approximately linear for annealed metals. However, for steels this relation is strongly influenced by the impact angle, resulting in more volume loss for big impact angles. [5].

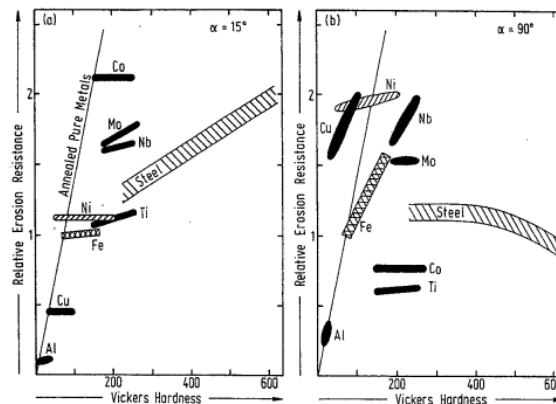


Figure 13. Impact resistance as a function of target material hardness for different materials and impact angles. [5].

According to Finnie et al. [21, 22], work hardening before the test does not lead to a high increase in erosion resistance. Naim et al. [23] also studied the relation between work hardening and erosion resistance for different levels of cold rolling reduction performed prior to testing. As cold rolling reduction increases, hardness increases too, but volume loss

also becomes higher. As it can be observed in Figure 14, a low work hardening level results in reduced volume loss. However, as the cold rolling reduction increases, volume loss increases abruptly. This feature is related to the capability of the target material to deform. Work hardening reduces the capability of the material to deform during the impact. Additionally, increasing the number of impacts results in higher erosion rate (i.e., volume loss per impact). Therefore, previous work hardening does not improve erosion resistance for multiple impacts. [5].

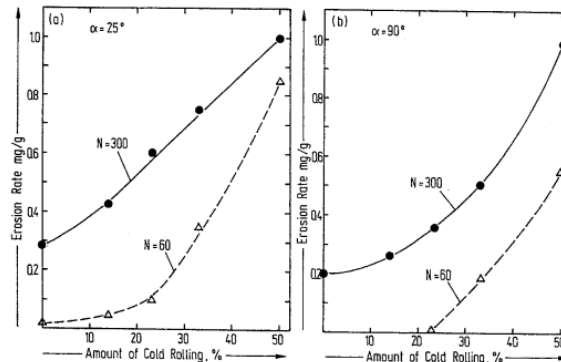


Figure 14. Erosion rate as a function of work hardening (cold rolling) for different impact angles and number of impacts. [5].

3.2. Adiabatic shear bands

3.2.1. Qualitative description

Adiabatic shear bands (ASB) are narrow regions where plastic deformation is highly concentrated. Their formation occurs when materials are deformed at high strain rates, and it is important because commonly they are precursors to fracture. According to K. Cho et al. [24], shear bands do not always produce fracture, but generally lead to failure of the structural component within the shear band because of loss of load-carrying capability. Adiabatic shear bands play an important role in dynamic deformation events, such as ballistic impacts or penetration of a target by a projectile. [16, 24]

A large number of materials are sensitive to shear band formation. According to K. Cho et al. [24], formation of shear bands is favored by low strain hardening rate, low strain rate sensitivity, low thermal conductivity and a high thermal softening rate. Thus, there are some favoring factors, such as thermal softening or geometrical softening, and some opposing factors such as strain rate hardening. Consequently, shear bands are commonly present in alloys of titanium, aluminum, copper and steels. Formation of shear bands is also highly

influenced by the microstructure of the material. Inhomogeneities, such as grain boundaries, precipitates and inclusions, lead to shear band formation due to stress concentrations in the vicinity of these regions. [16].

In 1943, Zener and Hollomon [25] presented an explanation for the shear band formation. According to their studies, the adiabatic shear bands are formed due to the fact that the effects of thermal softening become more important than the ones related to strain hardening. All theories that have been developed since then are based on the same principles. Figure 15 presents schematically the formation of a shear band. A parallelepiped is homogeneously deformed by a shear stress τ . When the strain reaches a certain value, referred as ε_c , deformation starts to be localized in a band, as it can be seen in (b). As it is shown in (c), initially the strain is homogeneous in the whole specimen. However, as soon as ε_c is reached, deformation starts to localize as the relative displacement of the sides of the specimen increases. Finally, Figure 15 (d) presents a stress-strain curve. It is possible to see that the stress is maximum for ε_c , and from that value on, softening starts to dominate.

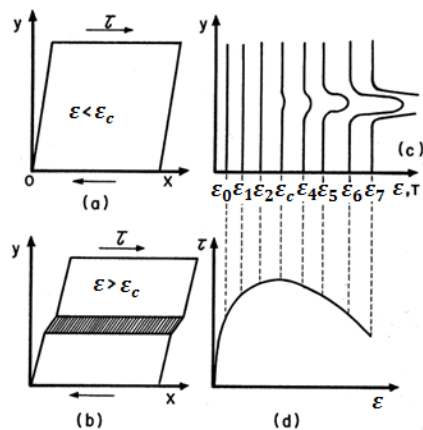


Figure 15. Schematic of the explanation for the formation of an adiabatic shear band. [16]

3.2.2. Metallurgical aspects

In the following, microstructural evolution and mechanical properties of shear bands are discussed. Shear bands can be classified in two different types, transformed and deformed, based on whether a phase transformation has occurred or not, respectively. In transformed adiabatic shear bands (TASB), the microstructure within them is different from that of the surrounding region. They are 5 to 10 μm wide and appear white in steels when etched with

a nital solution. Shear bands in quenched-and-tempered steels have usually this appearance. On the other hand, deformed adiabatic shear bands (DASB) have a dark appearance instead of white. This type of shear bands commonly appears in normalized and annealed steels. [16].

During plastic deformation adiabatic heating occurs within the shear bands because due to the involved short period of time, the heat is not conducted away. If the temperature in the shear bands reaches a limit value, a phase transformation may occur. A large number of studies have been performed on the structure of the transformed shear bands in steels. According to Beatty et al. [26], the microstructure is composed of numerous equiaxed grains with diameters ranging from 10 to 50 nm and with very low dislocation density within them. During plastic deformation, dynamic recrystallization occurs. Once ε_c is reached, new recrystallized grains begin to nucleate due to the adiabatic heating. Those new grains grow and are also deformed. Until the plastic deformation ceases new generation of grains continue appearing. As the strain rate increases, the size of the recrystallized grains decreases. Figure 16 illustrates the process of recrystallization. [16].

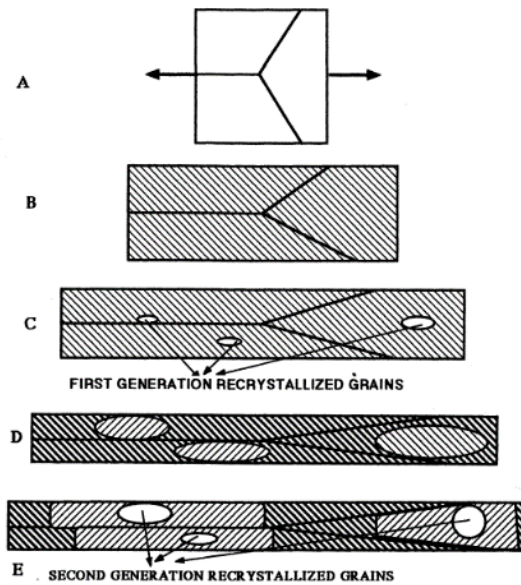


Figure 16. Schematic sequence of deformation-recrystallization steps in dynamic deformation. [16]

3.2.3. Elemental constitutive model

As discussed before, formation of adiabatic shear bands depends on the relationship between thermal softening and work hardening. That relationship can be expressed quantitatively according to Recht [27]. Generally, the shear stress depends on temperature, strain and strain rate. Considering that strain rate is constant during testing it can be assumed that the shear stress has not dependence on it. As shown in equation 6, it is possible to write this dependence in a differential way:

$$\tau = f(T, \varepsilon) \quad (5)$$

$$d\tau = \left(\frac{\partial \tau}{\partial T}\right)_{\varepsilon} dT + \left(\frac{\partial \tau}{\partial \varepsilon}\right)_T d\varepsilon \Rightarrow \frac{d\tau}{d\varepsilon} = \left(\frac{\partial \tau}{\partial T}\right)_{\varepsilon} \left(\frac{dT}{d\varepsilon}\right) + \left(\frac{\partial \tau}{\partial \varepsilon}\right)_T \quad (6)$$

where $\left(\frac{\partial \tau}{\partial T}\right)_{\varepsilon}$ represents the temperature sensitivity, $\left(\frac{dT}{d\varepsilon}\right)$ the changes of temperature and $\left(\frac{\partial \tau}{\partial \varepsilon}\right)_T$ the strain hardening. As it was shown in Figure 13, an adiabatic shear band forms when the material starts to soften, condition that is mathematically expressed by equation 7.

$$\frac{d\tau}{d\varepsilon} \leq 0 \quad (7)$$

Thus, the condition of instability is $\frac{d\tau}{d\varepsilon} = 0$. Applying this condition to equation 6 we obtain equation 8. This expression allows calculating the instability strain under adiabatic conditions. In order to calculate them, analytical expressions for the changes of temperature, the temperature sensitivity and the strain hardening are needed.

$$\left(\frac{\partial \tau}{\partial \varepsilon}\right)_T = -\left(\frac{\partial \tau}{\partial T}\right)_{\varepsilon} \left(\frac{dT}{d\varepsilon}\right) \quad (8)$$

First of all, the expressions for the change of temperature $\left(\frac{dT}{d\varepsilon}\right)$ is obtained. The adiabatic temperature rise in the material is computed by converting the work of deformation into an increase of temperature through the material heat capacity, C_V , its density and the efficiency of the conversion of work into heat, β , whose experimental value is 0.9-1. It is worth to note that the bulk C_V of the material is dependent on temperature and phase fractions (in the case that phase transformation occurs).

$$dT = \frac{\beta}{\rho C_V} dW \quad \text{where} \quad dW = \tau d\varepsilon \quad (9)$$

$$dT = \frac{\beta}{\rho C_V} \tau d\varepsilon \quad (10)$$

The shear stress is expressed using the expression presented in equation 11, where A , B and n are constants.

$$\tau = A + B\varepsilon^n \quad (11)$$

By substituting equation 11 into equation 10 the expression for $\left(\frac{dT}{d\varepsilon}\right)$ is obtained:

$$\frac{dT}{d\varepsilon} = \frac{\beta}{\rho C_V} (A + B\varepsilon^n) \quad (12)$$

On the other hand, the thermal softening component can be expressed by the linear relationship shown in equation 13, in which τ_T is the shear stress at temperature T , τ_{T0} is the shear stress at the initial temperature T_0 and T_m is the melting point.

$$\tau_T = \tau_{T0} \frac{T_m - T}{T_m - T_0} \quad \Rightarrow \quad \tau_T = (A + B\varepsilon^n) \frac{T_m - T}{T_m - T_0} \quad (13)$$

By differentiating equation 13 with respect to T and considering ε constant, we obtain the expression for $\left(\frac{\partial \tau}{\partial T}\right)_\varepsilon$.

$$\left(\frac{\partial \tau}{\partial T}\right)_\varepsilon = \frac{-(A + B\varepsilon^n)}{T_m - T_0} \quad (14)$$

Finally, differentiating equation 11 with respect to ε the expression for the strain hardening is obtained.

$$\left(\frac{\partial \tau}{\partial \varepsilon}\right)_T = nB\varepsilon^{n-1} \quad (15)$$

By the substitution of equations 12, 14 and 15 into equation 8, we obtain the expression that allows calculating the value of the instability strain ε_C , since the rest of the parameters are known.

$$\left(\frac{\partial \tau}{\partial \varepsilon}\right)_T = -\left(\frac{\partial \tau}{\partial T}\right)_\varepsilon \left(\frac{dT}{d\varepsilon}\right) \Rightarrow nB\varepsilon_C^{n-1} = \left[\frac{(A + B\varepsilon_C^n)}{T_m - T_0}\right] \left[\frac{\beta}{\rho C_V} (A + B\varepsilon_C^n)\right] \quad (16)$$

4. MARTENSITIC WEAR STEEL

Martensite is the hard microconstituent present in quenched steels. Martensite provides a great balance between strength and toughness. Consequently, it is widely used as the main microconstituent of steels for wear and high strain rate applications. The martensitic transformation (transformation of austenite to martensite) is diffusionless (iron and carbon atoms do not have time to diffuse), in contrast to other transformations in ferrous systems, such as the formation of ferrite or perlite. Thus, martensitic transformation takes place almost instantaneously, generally at the speed of sound in the material. In order to suppress the diffusion and obtain martensite, the cooling rate should be high enough, which is possible to be achieved through quenching. In contrast to diffusion, the martensitic transformation is controlled by a shear mechanism. [28]

Figure 17 shows the Isothermal Transformation (IT) and Continuous Cooling Transformation (CCT) diagrams for an AISI 4130 steel. Even though the composition of the steels studied in this work differ from the one shown in Figure 17, the behavior during cooling is expected to be similar. As it can be observed, in order to obtain only martensitic microstructure, high cooling rates are needed. Lower cooling rates lead to a mixture of bainite and martensite or even some ferrite can appear. Therefore, in order to get martensite as the main microconstituent water quenching is required because it provides high enough cooling rates. [29]

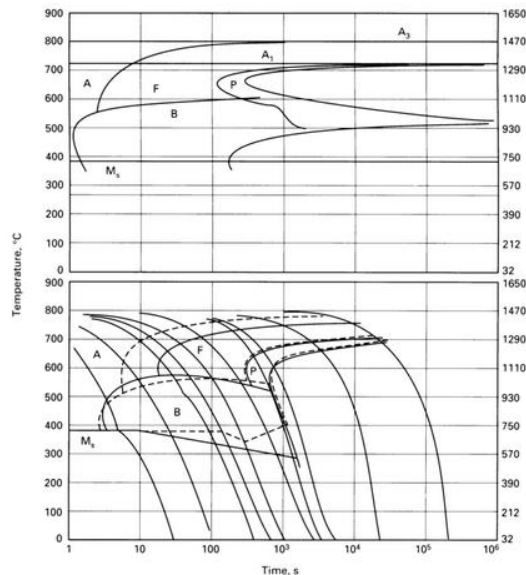


Figure 17. Isothermal transformation and CCT diagrams for AISI 4130 steel containing 0.30 %C, 0.64 %Mn, 1 %Cr and 0.24 %Mo. [29]

4.1. Martensite : microstructure and mechanical properties

As mentioned above, martensite is the metastable phase that forms upon rapid quenching of the austenite phase. Austenite has a Face Centered Cubic (FCC) crystal structure, while martensite has a Body Centered Tetragonal (BCT) structure. As it is shown in Figure 18, untempered martensite is the phase that has the highest hardness in steels. It is also characterized by being extremely brittle and by lacking toughness.

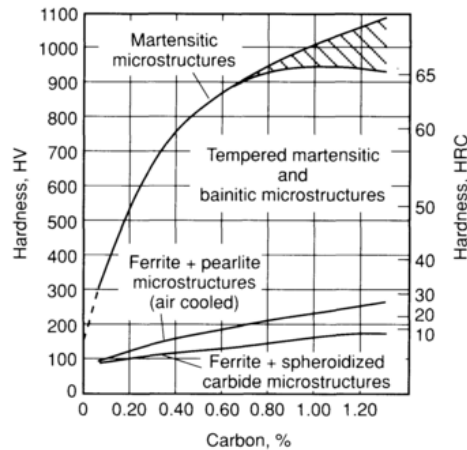


Figure 18. Hardness for different microstructures in steels [30]

4.1.1. Martensitic transformation

As mentioned above, martensite is formed from austenite through a diffusionless shear transformation. The diffusionless character of the martensitic transformation can be demonstrated: 1) Martensite can be formed at very low temperatures, at which diffusion is not possible; 2) The chemical composition of the martensite structure is identical to that of the parent austenite; 3) Martensite plates can grow at speeds close to that of the sound in metals, which would not be possible if diffusion was involved. The change from FCC-structure of austenite to BCT-structure of martensite is achieved by deformation of the parent phase due to a shear strain. Hence, during the transformation, numerous atoms move simultaneously in order to form the martensitic crystals. Figure 19 shows the process of formation of a martensitic crystal. During the transformation, the shears act parallel to a fixed crystallographic plane (called habit plane), producing a tilted surface. In this procedure two changes occur. Firstly, the crystal structure changes from FCC to BCC, change that is termed as the lattice deformation. In addition, another change, the so called lattice

invariant deformation, occurs. As a result, the transformed martensite is simultaneously deformed. As a consequence, a high density of dislocations is produced leading to the very high strength of as-quenched martensite. The carbon atoms trapped within the interstitial sites also contributes to the high strength. These trapped carbon atoms result in a distortion in the structure, so the real structure of martensite is a distorted BCC (referred as Body centered Tetragonal, BCT), instead of the common BCC. [28, 31, 32] .

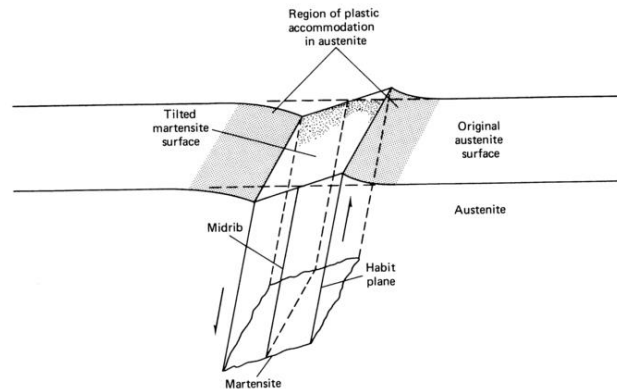


Figure 19. Schematic of the process of formation of a martensite plate. [28]

As a result of the martensitic transformation, twinned or slipped martensite can be formed. A schematic of both transformation are shown in Figure 20. According to Bhadeshia [32], in ordinary plastic deformations at low temperature or with high strain rates, twinning is more likely to happen than slipping. Some kinetic factors may be decisive to determine whether slipping or twinning occurs. However, the exact reasons for the formation of one or another are not deeply known. [32].

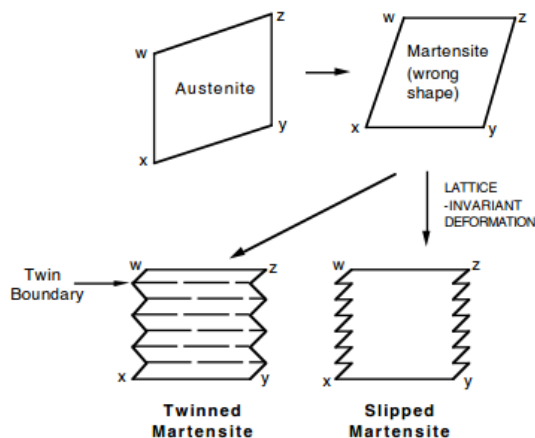


Figure 20. Schematic of the formation of twinned and slipped martensite. [32]

A critical temperature, known as martensite start temperature (M_s), needs to be reached to start the martensitic transformation. When the steel is cooled down to temperatures below M_s , the transformation starts and martensite begins to form. M_s depends on the carbon and alloy content. Therefore, numerous equations have been developed in order to calculate M_s based on the composition of the steel. Some of these equations can be found in reference [33]. According to these models, M_s decreases if the carbon and/or the amount of almost all alloying elements increases. This trend can be observed in Figure 21. If M_s is very low, incomplete martensite formation can occur, which causes the presence of retained austenite. Retained austenite affects the final mechanical properties and can cause dimensional instability as well as reduce hardness and strength [34, 35].

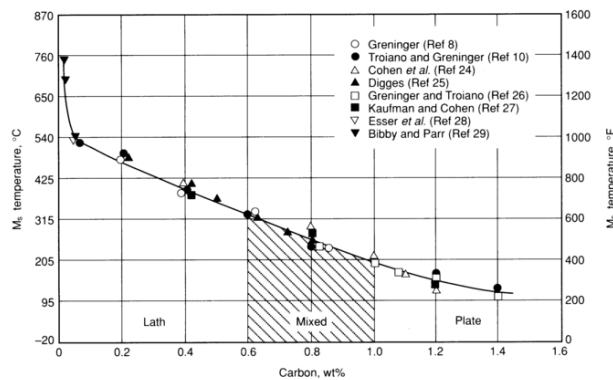


Figure 21. Martensite start (M_s temperature) as a function of carbon content in steels [28, 33].

4.1.2. Morphologies of martensitic microstructures

In iron-carbon alloys and steels two different morphologies of martensitic microstructures can be formed, known as lath and plate martensite. Their formation depends basically on the composition of the steel, mainly on the carbon content, as it is shown also in Figure 21. Figure 22 illustrates schematically both types of martensite and Figure 23 shows their micrographs. Lath martensite is formed in low and medium-carbon alloys, with a content of carbon ranging from 0 to 0.6 wt %C. Lath martensite is the structure that the hardest steels have. It is characterized by very fine lath-shaped crystals that are oriented in groups in the same direction. Between the laths there are small amounts of retained austenite. For an intermediate composition, ranging from 0.6 to 1 wt %C both morphologies are mixed. Finally, in high-carbon steels (1-1.6 wt %C), plate martensite forms. In this case, lenticular crystals are formed and they are non-parallel, but they form a zig-zag pattern. High-carbon

steels have lower M_s , therefore this microstructure contains large amounts of retained austenite. Hence, lath martensite is finer than plate martensite and it has significantly less amount of retained austenite. [28, 36].

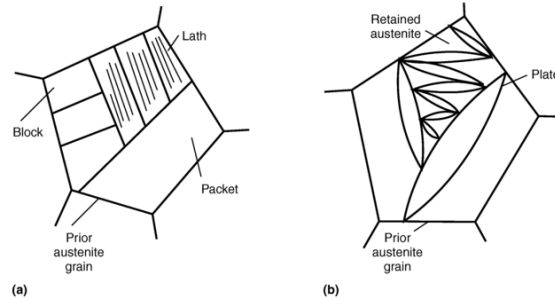


Figure 22. Schematic view of both morphologies of martensite.(a) Lath martensite (b) Plate martensite . [36, 37].

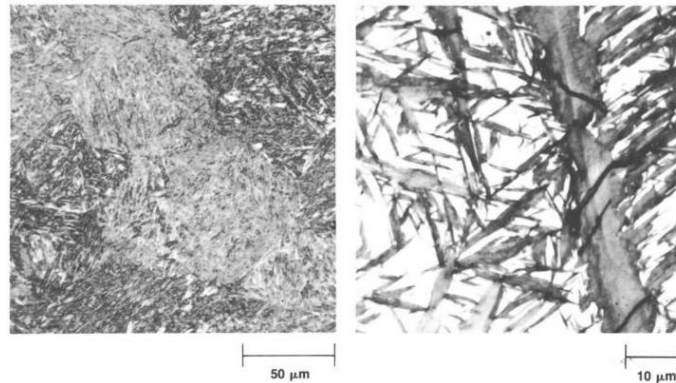


Figure 23. Micrograph of lath martensite (left) [28, 38] and plate martensite (right) [28, 37].

4.2. Manufacturing of wear resistance steels

Both Ultra High Strength Steels (UHSS) investigated in the present study were produced by a thermo-mechanical processing, consisting of controlled rolling integrated with direct quenching (DQ). During thermo-mechanical processing a thermal process is performed simultaneously to the deformation, in order to better control the resulting mechanical properties. Thermo-mechanical processing requires a strict control of initial composition of the material, temperature during deformation and cool-down process. As a result, it is possible to obtain uniform and fine grain structure as well as a specific content and distribution of different structures, such as martensite, bainite, austenite or ferrite. Consequently, the obtained product has the desired mechanical properties. [39]

In the case when direct quenching is combined with controlled rolling, the final properties are defined mainly by the final rolling temperature and quenching rate. The rolling temperature is strictly controlled to assure that the steel is within the non-recrystallization region during the last few rolling sticks, resulting in small austenite grain size before direct quenching. When the rolling is done below recrystallization temperature grain nucleation occurs not only on the grain boundaries, but also in the formed shear bands. As a result, a large number of fine grains are formed, resulting on better mechanical properties. Therefore, grain size and, consequently, the mechanical properties are defined by the final rolling temperature. In the following the different stages of the manufacturing process are explained.

4.2.1. Hot Rolling

Rolling is one the most common processes used in metal working, since it is utilized in almost 90 percent of the metal production. It consists of passing the material between two rolls. The turning rolls apply a compressive force against the trip, leading to a reduction of its thickness. Hot rolling is performed at high temperatures (ranging from 800 to 1200 °C for low-alloy steels), which often results in a change of the shape and size of the grains to a slightly elongated microstructure in respect to the rolling direction. The resulting microstructure is strongly influenced by the final rolling temperature. As it can be observed in Figure 24, before hot rolling the microstructure has coarse grain size. While passing through the rolls the grains are deformed, and also some new grains grow, leading to a resulting microstructure with small, uniform grains and enhanced ductility. [34, 39].

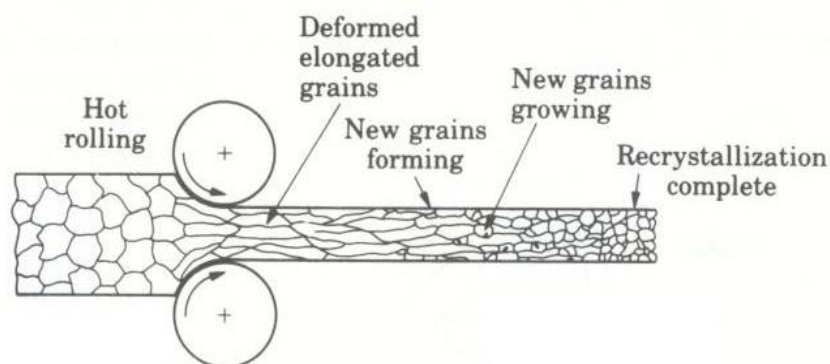


Figure 24. Changes in the grain structure due to rolling process. [34].

4.2.2. Direct quenching

Direct quenching is not very widely used but it is, nowadays, one of the most effective processes for wear resistant steels manufacturing. An accurate control of process parameters in combination with a controlled chemical composition of the steel leads to a good strength, toughness and ductility balance. In general, quenching of steel is a process in which the steel is rapidly cooled from an elevated temperature to achieve a martensitic microstructure. During the quenching, the steel develops an as-quenched microstructure that is typically martensite or martensite/bainite mixture depending on the carbon level and the cooling rate. Quenching is highly affected by the cooling characteristics of the quenching media, which determines the cooling rate, and the hardenability of the steel. [1, 40].

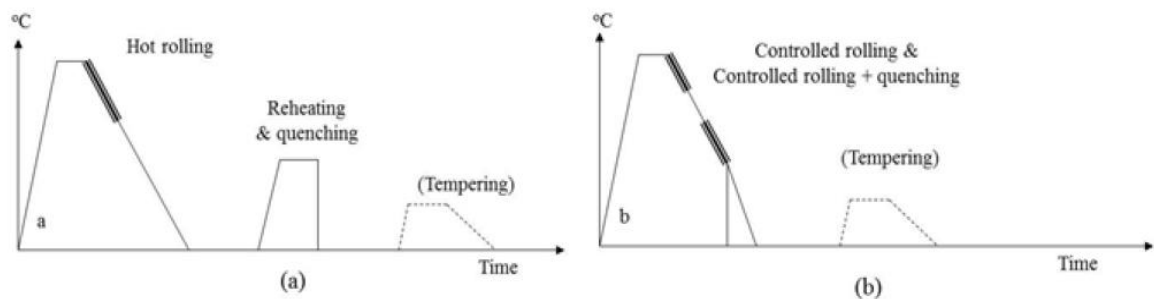


Figure 25. Temperature-time diagrams for (a) conventional rolling + quenching and (b) direct quenching [1]

Figure 25, shown above, illustrates the differences between conventional quenching and direct quenching. During the conventional process the plates are hot rolled and, afterwards, reheated and quenched. The steel is reheated to form austenite and water cooled, which leads to martensitic structure or a mixture of martensite and bainite. The martensitic microstructure formed upon rapid quenching of austenite is brittle. As a consequence, after quenching, tempering is also required to regain ductility and toughness. However, in direct quenching, water quenching is performed immediately after hot rolling as a part of the rolling process. [1]

According to Kaijalainen et al. [41], the austenite processing has a big influence on the mechanical properties of the direct quenched steels. The best combination of strength, toughness and ductility was found for direct quenched steels with auto-tempered lath martensite and lower bainite. This microstructure is more likely to be achieved for low carbon content and low alloyed steels, and it is enhanced when high fraction of the rolling process is performed in the non-recrystallization temperature range. Direct quenching

performed at non-recrystallization temperature range leads to finer grain size due to grain nucleation at shear bands formed during the previous rolling. As mentioned, chemical composition of the steel is essential to get the microstructure that leads to the targeted mechanical properties. Low carbon content prevents the need of tempering after direct quenching, because it assures high impact toughness of the obtained martensite and/or bainite microstructure obtained. Controlling other alloy elements, such as Cr, Cu, Ni, Mo, Nb, V or B, the required hardenability is achieved. Table 1 shows the composition limits of the different elements to achieve good properties by direct quenching. Steels with low carbon and alloy content processed by direct quenching can reach values of yield strength ranging from 900 to 1100 MPa. [1]

Table 1. Chemical composition limits of direct-quenched strength steels (wt%)

$$*CEV = C + Mn/6 + (Cr + Mo + V)/5 + (Cu + Ni)/15$$

	C	Si	Mn	P	S	Ti	CEV
S 900 DQ	0.10	0.25	1.15	0.02	0.01	0.07	0.51
S 960 DQ	0.11	0.25	1.20	0.02	0.01	0.07	0.52
S 1100 DQ	0.15	0.30	1.25	0.02	0.01	0.07	0.50

5. METHODS OF MATERIAL TESTING AT DIFFERENT STRAIN RATES

Characterization of materials requires testing at a wide range of strain rates, which it is not achievable with a single technique. Therefore, there are different setups that can be used depending on the desired strain rate range. In general, if a higher strain rate is needed, the procedure becomes more complicated. [42] Furthermore, conditions such as distribution of the stresses on the specimen or thermal conditions during testing also depend on the strain rate. Table 2 lists the different techniques for compression tests and their related strain rates. Also, Figure 26 shows the different techniques and their corresponding strain rate regimes, as well as the conditions during testing.

Table 2. Experimental methods for compression testing and related strain rates. [43].

Strain Rate, s^{-1}	< 0.1	0.1-100	0.1-500	200-10 ⁴	10 ³ -10 ⁵
Compression testing technique	Conventional load frames	Special servohydraulic frames	Cam plastometer and drop test	Hopkinson bar	Taylor impact test

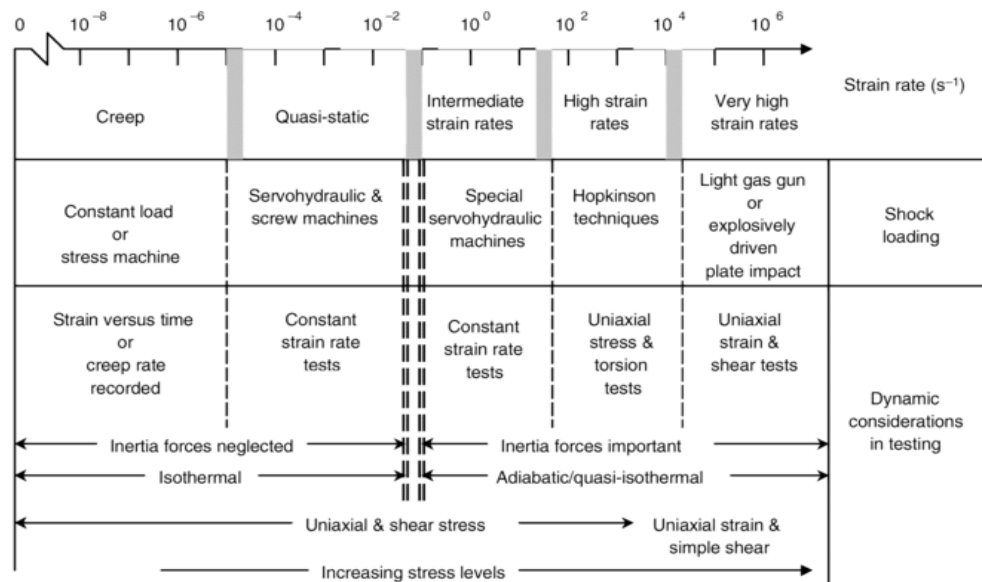


Figure 26. Experimental methods at different strain rates and conditions during testing. [43].

Creep and stress relaxation tests are used for testing at the lowest strain rates ($< 10^{-5} \text{ s}^{-1}$). These devices have a simple mechanical construction. They maintain constant load or strain over the sample for a long period of time. As a result, strain or elongation can be recorded as a function of time. Also the environment, regarding temperature and humidity, is totally controlled. For strain rates ranging from 10^{-5} to 10^{-1} s^{-1} , quasi-static tests are used. These techniques are easy to perform using servohydraulic and screw driven testing machines, which allow having control over load, strain or displacement. The maximum strain rate achievable with these devices is around 1 s^{-1} . Special servohydraulic machines can be used to achieve intermediate strain rates, ranging from 10^{-1} s^{-1} to 10^2 s^{-1} . The main problem in this range is that conventional testing techniques cannot be used because they are highly affected by the wave propagation effects, while test duration is too long to apply dynamical methods. Wave propagation effects create a large number of oscillations in the measured signal that results in oscillations in the stress-strain curve. At strain rates ranging from 10^2 to 10^4 s^{-1} , Split-Hopkinson Pressure Bar (SHPB) is the most commonly used technique. Its main feature is that it allows the deformation of a sample at a high rate while maintaining an uniform uniaxial state of stress in the sample. More detailed information about SPHB is presented in Section 5.1. Regarding high strain rates, Taylor impact testing is used to achieve values between 10^3 and 10^5 s^{-1} . This technique consists in shooting a cylindrical specimen against a rigid wall. Other techniques used to achieve the same strain rate for tension loading are the expanding rings and flying wedge techniques. Higher strain rates can be obtained with explosively driven devices or high velocity flying projectiles. [13, 44].

As mentioned before, concerning the test conditions, there are also some differences between low and high strain rate testing. At low and quasi-static strain rates, the stresses are uniformly distributed on the specimen, i.e., the specimen is in a state of static stress equilibrium. As a consequence of this equilibrium state, the sum of the forces acting on each element of the body is always zero. On the other hand, at higher strain rates there is no stress equilibrium because the stresses are irregularly distributed. Since the load is propagated as waves through the body, one part of it can be loaded before the rest does. Thermal conditions are also different. At low strain rate testing the heat generated during the deformation is conducted away from the specimen, so material temperature is not changed. In contrast to that, at high strain rate, thermal conditions become adiabatic because the test duration is so short that the heat generated during the deformation has not enough time to be conducted away. As a consequence, there is a rise in the temperature of the specimen, which leads to thermal softening. As a result of thermal softening, adiabatic shear bands can appear. [13, 44]. Adiabatic shear bands are further discussed in Section 3.2. Equation 17 provides an estimation of the increase of temperature of the material, ΔT , during the test.

$$\Delta T = \frac{\beta}{c\rho} \int \sigma d\varepsilon \quad (17)$$

In this equation, c represents the specific heat capacity of the material, while β is a parameter that gives the fraction of mechanical energy that is transformed into heat, and its value for metals varies from 0.9 to 1. σ is the stress, ε the strain and ρ the density of the material.

5.1. Split Hopkinson Pressure Bar system

5.1.1. Description of the Split-Hopkinson Pressure Bar technique

In the following, a description regarding SHPB device and its way of working is presented. SHPB technique is based on the propagation of one-dimensional pressure waves in solids. It is used for testing different materials at strain rates ranging from 10^2 to 10^4 s^{-1} . [13]. SHPB test equipment is composed of two pressure bars, called incident/input bar and transmitted/output bar, a striker bar, a compressed gas launcher, two strain gages located in the bars and a data acquisition system. A third bar, called momentum trap bar, can be added behind the transmitted one. Figure 27 shows the setup of the device. As it can be observed, the specimen is placed between the incident and transmitted bar. [45, 46].

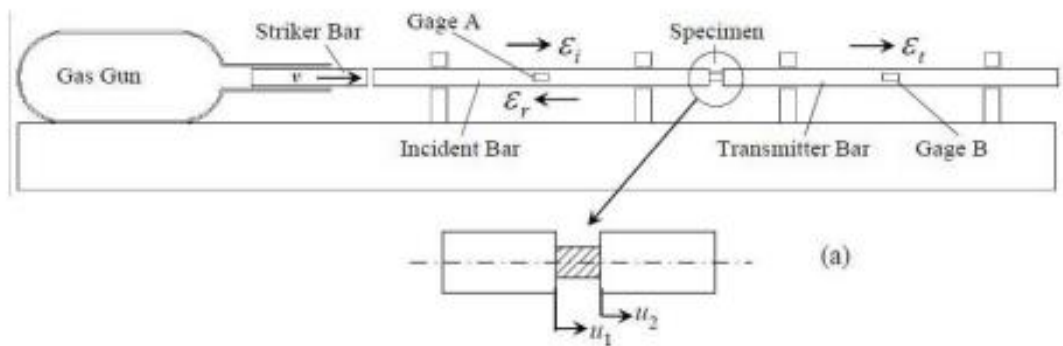


Figure 27. Setup of Hopkinson Split Bar device. [45].

The test procedure consists of impacting the striker bar against the incident bar. This generates a compressive wave that travels through the incident bar and reaches the bar-specimen interface. There, part of the pulse is reflected and the other part is transmitted to the output bar. That transmitted part of the wave can be trapped if the momentum bar trap is being used. The transmitted wave penetrates to the specimen and produces elastoplastic deformation in it. The three stress pulses (incident, transmitted and reflected) are measured using two strain gages located on the surfaces of the incident and transmitted bars. The signals are amplified and recorded using a digital oscilloscope. Figure 28 presents an example of the recorded signals, which are used to calculate the stress, strain and strain rate. A further explanation of the calculations based on the propagation of waves is presented in more details in Section 5.1.3. [13, 44, 46].

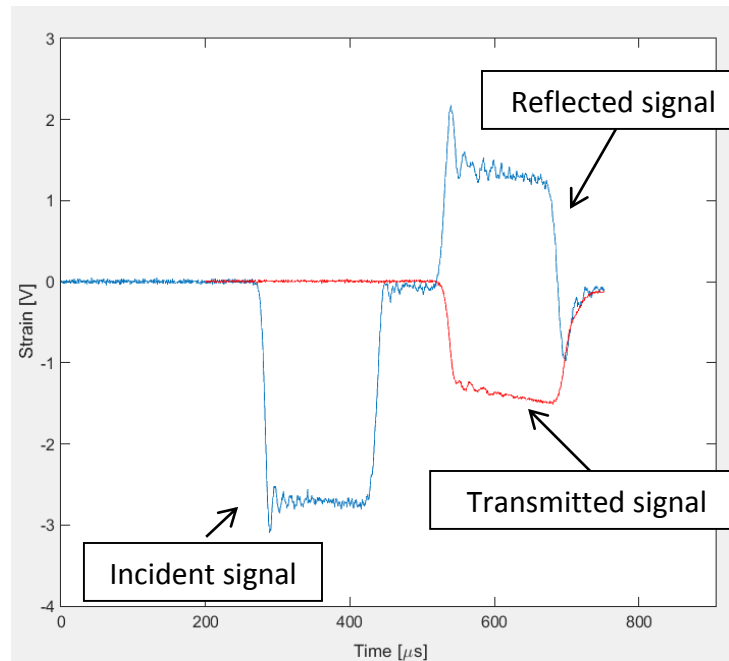


Figure 28. Typical signals recorded by strain gages in a SHPB test.

5.1.2. Description of the Split Hopkinson Pressure Bar equipment at TUT

In this section the equipment used in the current work is described in more details. This device is located at the Department of Material Science of Tampere University of Technology (TUT). Figure 29 shows an image of the actual equipment.



Figure 29. SHPB equipment used at TUT [12].

The design of the bars should satisfy several criteria in order to assure one-dimensional propagation and avoid distortion. Firstly, with a length-to-diameter ratio of about 20, one-dimensional propagation can be achieved. In addition, the diameter is also influenced by the strain-rate required. For higher strain rates, smaller specimens and also smaller bar diameters are required. Additionally, the bars must be straight and their axes must be perfectly aligned. The most important feature is that bars must remain in the elastic region during the test so the data obtained can be used to calculate the stress and the strain in the specimen. [44, 45].

These features were taken into consideration in the design of SHPB device used in the current work. According to [12], this apparatus has two or three bars (depending on whether the momentum bar trap is used or not) made of high strength steel AISI 4030, which have the properties presented in Table 3. The diameter of the bars is 22 mm and the length 1200 mm. The striker bar is also made of the same material and has the same diameter.

Table 3. Mechanical properties of Ultra High Strength Steel AISI 4030. [12]

Yield strength, σ [MPa]	Young's modulus, E [GPa]	Longitudinal elastic wave velocity, C_0 (m/s)
1100	209	5160

The striker bar is accelerated using an air gun. Its velocity can be controlled via the adjustment of the pressure of the gas cylinder. Regarding the recording of the stress pulses, pairs of Kyowa resistive strain gages are used in the incident and transmitted bar. The gages are placed on the opposite sides of each bar to exclude any bending effects. The signals from the strain gages are amplified by Kyowa CDV 700A amplifiers. The signals are recorded

by two 12-bit 10-Megasample Yokogawa DL 708 digital oscilloscopes. Finally, the digital oscilloscopes are connected to a computer where the results are calculated using a MATLAB® code. It is necessary to correct the measured strain pulses. For this reason, fast Fourier transformations and the Pochhammer-Chree frequency equation are used. [12].

5.1.3. Theory of the Split-Hopkinson Pressure Bar

The Hopkinson Split Bar is based on the one-dimensional wave propagation. Once the measured waves have been corrected to represent the actual waves, the uniaxial elastic stress wave theory can be applied to obtain the SHPB equations. A differential element of the bar, as shown in Figure 30, is going to be considered.

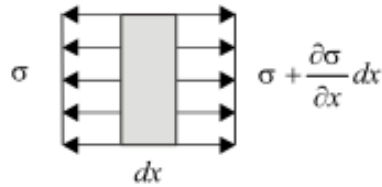


Figure 30. Differential element of a bar. [42].

Applying the momentum balance in the longitudinal direction we get:

$$-\sigma A + \left(\sigma + \frac{\partial \sigma}{\partial x} dx \right) A = \rho A dx \frac{\partial^2 u}{\partial t^2} \quad (18)$$

$$\frac{\partial \sigma}{\partial x} = \rho \frac{\partial^2 u}{\partial t^2} \quad (19)$$

where σ is the stress in the bar, u the particle displacement, A the cross sectional area and ρ the density of the bar, respectively.

The Hooke's Law gives the relation between stress σ and strain ε , where the strain can be expressed as $\varepsilon = \frac{\partial u}{\partial x}$ (20). Thus,

$$\sigma = E\varepsilon = E \frac{\partial u}{\partial x} \quad (21)$$

By substitution of equation 21 into equation 19 another expression is obtained:

$$E \frac{\partial^2 u}{\partial x^2} = \rho \frac{\partial^2 u}{\partial t^2} \quad (22)$$

where E represents the Young's modulus. In equation 23 the relation between E and ρ is presented, where C_0 represents the propagation velocity on the wave in the bar. By substituting equation 23 into equation 22 the governing equation for the elastic wave propagation is obtained:

$$C_0 = \sqrt{E/\rho} \quad , \quad \frac{\rho}{E} = \frac{1}{C_0^2} \quad (23)$$

$$\frac{\partial^2 u}{\partial x^2} = \frac{1}{C_0^2} \frac{\partial^2 u}{\partial t^2} \quad (24)$$

D'Alembert solution, shown in equation 25, satisfies equation 24:

$$u(x, t) = f(x - C_0 t) + g(x + C_0 t) \quad (25)$$

The process followed to obtain these same equations can be, as well, found in [42].

Based on that expression, the displacements of the bar ends are given as:

$$u_1(x, t) = f(x - C_0 t) + g(x + C_0 t) = u_i + u_r \quad (26)$$

$$u_2(x, t) = h(x - C_0 t) = u_t \quad (27)$$

where f , g and h are functions which describe the incident, reflected and transmitted waves, respectively. u_i , u_r and u_t represent the incident, reflected and transmitted displacements, while u_1 and u_2 are the displacements in the incident and transmitted bars. Based on equations 26 and 27 it is possible to have the expressions of u_i , u_r and u_t , shown in equations from 28 to 30.

$$u_i(x, t) = f(x - C_0 t) \quad (28)$$

$$u_r(x, t) = g(x + C_0 t) \quad (29)$$

$$u_t(x, t) = h(x - C_0 t) \quad (30)$$

Differentiating equations 28, 29 and 30 with respect to x , the expressions in equations 31, 32 and 33 are obtained:

$$\frac{\partial u_i}{\partial x} = f'(x - C_0 t) \quad (31)$$

$$\frac{\partial u_r}{\partial x} = g'(x + C_0 t) \quad (32)$$

$$\frac{\partial u_t}{\partial x} = h'(x - C_0 t) \quad (33)$$

Differentiating also equations 26 and 27 respect to t , and replacing the expressions of equation 31, 32 and 33 into them, the particle velocities v caused by the waves are obtained.

$$\frac{\partial u_1}{\partial t} = v_1 = -C_0 f'(x - C_0 t) + C_0 g'(x + C_0 t) = -C_0 \frac{\partial u_i}{\partial x} + C_0 \frac{\partial u_r}{\partial x} \quad (34)$$

$$\frac{\partial u_2}{\partial t} = v_2 = -C_0 h'(x - C_0 t) = -C_0 \frac{\partial u_t}{\partial x} \quad (35)$$

Taking into consideration equation 21 and by its substitution into equations 34 and 35 we obtain the expression for the bar end velocities v_i . In these expressions ε_i , ε_r and ε_t represent the incident, reflected and transmitted strain, respectively.

$$v_1 = -C_0 \frac{\partial u_i}{\partial x} + C_0 \frac{\partial u_r}{\partial x} = -C_0 \varepsilon_i + C_0 \varepsilon_r \Rightarrow v_1 = -C_0 (\varepsilon_i - \varepsilon_r) \quad (36)$$

$$v_2 = -C_0 \frac{\partial u_t}{\partial x} = -C_0 \varepsilon_t \Rightarrow v_2 = -C_0 \varepsilon_t \quad (37)$$

Differentiating equations 26 and 27 with respect to x and taking into account equation 21, ε_1 and ε_2 can be related to ε_i , ε_r and ε_t , as in equations 38 and 39:

$$\varepsilon_1 = \varepsilon_i + \varepsilon_r \quad (38)$$

$$\varepsilon_2 = \varepsilon_t \quad (39)$$

The development of these equations is based on the one presented in [45].

Above, it has been assumed that wave propagation occurs in a homogeneous medium. However, wave reflection and transmission at the boundary bar-sample occur. In equations 40 and 41 the expressions of the existing forces at incident and transmitted bars are presented.

$$F_1 = EA\varepsilon_1 = EA(\varepsilon_i + \varepsilon_r) \quad (40)$$

$$F_2 = EA\varepsilon_2 = EA\varepsilon_t \quad (41)$$

According to equilibrium assumption, both forces should be equal. As a consequence, a relation between the three different strains is obtained:

$$F_1 = F_2 \quad \Rightarrow \quad \varepsilon_i + \varepsilon_r = \varepsilon_t \quad (42)$$

Strain rate in the specimen, $\dot{\varepsilon}$, can be calculated using equation 43, where L is the length of the specimen.

$$\dot{\varepsilon} = \frac{v_1 - v_2}{L} \quad (43)$$

By substitution of the equations 36 and 37 into equation 43, equation 44 is achieved:

$$\dot{\varepsilon} = \frac{C_0(-\varepsilon_i + \varepsilon_r) + C_0\varepsilon_t}{L} = \frac{C_0}{L}(-\varepsilon_i + \varepsilon_r + \varepsilon_t) \quad (44)$$

Using the relation between the strains obtained in equation 42, the expression for calculating the strain rate is obtained:

$$\dot{\varepsilon} = \frac{2C_0\varepsilon_r}{L} \quad (45)$$

The strain can be calculated integrating equation 45:

$$\dot{\varepsilon} = \frac{2C_0}{L} \int \varepsilon_r dt \quad (46)$$

The stress can be calculated knowing that the force is the product of stress and area. Assuming that the specimen is deforming under force equilibrium, F_1 and F_2 are equal. To calculate the stress, F_2 is going to be used because the signal quality of F_1 is usually worse, since it is obtained as the addition of two large number with similar values but opposite signs. Hence, using F_2 (equation 41) the stress is obtained with equation 47:

$$F_2 = AE\varepsilon_t = A_S\sigma \Rightarrow \sigma = \frac{AE\varepsilon_t}{A_S} \quad (47)$$

where A_S is the initial area of the specimen. More detailed expressions are obtained in [42, 45].

5.1.4. Dispersion of elastic waves

In the equations presented above, some assumptions have been made. Firstly, it is considered that the stresses in the specimen are uniformly distributed. Secondly, Poisson's effect is not considered, therefore lateral expansions or contractions are ignored. In addition, it is assumed that the contact between the striker and the incident bar during the impact is perfect because the surfaces of the end of both bars are flat and made of the same material. As a consequence of this perfect contact, it is assumed that the stress wave generated is one-dimensional. Lastly, the equation of wave motion does not consider any alteration on wave motion, such as bar ends and sidewalls. [13, 44].

Nevertheless, in practice these assumptions cannot be considered totally valid. There are some lateral strains due to Poisson's effect, which generate an uniform stress distribution, leading to distortion. Moreover, the contact between the bars is not perfect. Consequently, there is some friction that produces a radial constraint. Additionally, there is always more than one single frequency component in the load pulse. Each frequency component travels at a different velocity in the material, so that the higher is the frequency component, the slower it travels. Thus, this variety of velocities leads to a dispersion of the propagation of the stress pulse. As a result, the stress waves are not perfectly trapezoidal. [13, 44]. In addition, the incident pulse is not measured at the interface incident bar-specimen but at some distance away. Similarly, the transmitted pulse is measured some distance after the interface specimen-transmitted bar. As a consequence, the pulses that are measured are different from the ones actually deforming the specimen, because their shape is modified when they travel in the bars.

Dispersion has to be minimized and corrected in order to get accurate results. Diverse methods, numerical and experimental, have been developed. There are numerous correction methods, such as those made by Bacon [47], Follansbee [48] or Gorham [49]. The correction proposed by Gorham is one of the most widely used and in the following it

is briefly explained. This procedure consists in, firstly, applying Fourier transformation (FFT) to convert the strain signal that is expressed in time domain to frequency domain. Once the signal is in the frequency domain, a phase shift (φ) is applied to each frequency component. Finally, the signal is converted back to time domain using an inverse Fourier transformation. Applying this procedure, the signals that have been measured at some distance away from the bars-specimen interfaces are extrapolated to them. This procedure can be illustrated using some equations, as it is shown in the following. The original time domain signal can be expressed with the following function $F(t)$:

$$F(t) = \sum_n [A_n \cos(2\pi n\omega t) + B_n \sin(2\pi n\omega t)] \quad (48)$$

where ω is the fundamental frequency. Applying the FFT to this function $F(t)$ the coefficients A_n and B_n are obtained. The dispersion effects can be corrected shifting the phase of each frequency component by $\varphi(\omega)$. That leads to a new expression $F'(t)$:

$$F'(t) = \sum_n [A_n \cos(2\pi n\omega t + \varphi) + B_n \sin(2\pi n\omega t + \varphi)] \quad (49)$$

This equation can also be written replacing coefficients A_n and B_n by A'_n and B'_n , which include the phase shift:

$$F'(t) = \sum_n [A'_n \cos(2\pi n\omega t) + B'_n \sin(2\pi n\omega t)] \quad (50)$$

where:

$$A'_n = A_n \cos(\varphi) + B_n \sin(\varphi) \quad (51)$$

$$B'_n = B_n \cos(\varphi) - A_n \sin(\varphi) \quad (52)$$

The phase shift for each frequency component can be calculated using equation 53 and it is related to the propagation distance (z). It depends also on the wave velocity in the pressure bar at the fundamental frequency, C_f , and on the phase velocity of each frequency component C_n , which are obtained by interpolation of the tabulated data of Bancroft [50] .

$$\varphi = 2\pi n\omega z \left(\frac{1}{C_f} - \frac{1}{C_n} \right) \quad (53)$$

For the incident signal a forward correction is needed, so the value of z is positive and it is the distance from the strain gage on the incident bar to the interface incident bar-sample. On the other hand, for the reflected and transmitted signal a backward correction should be used, therefore, the value of z is negative. Figure 31 shows the original and corrected signals.

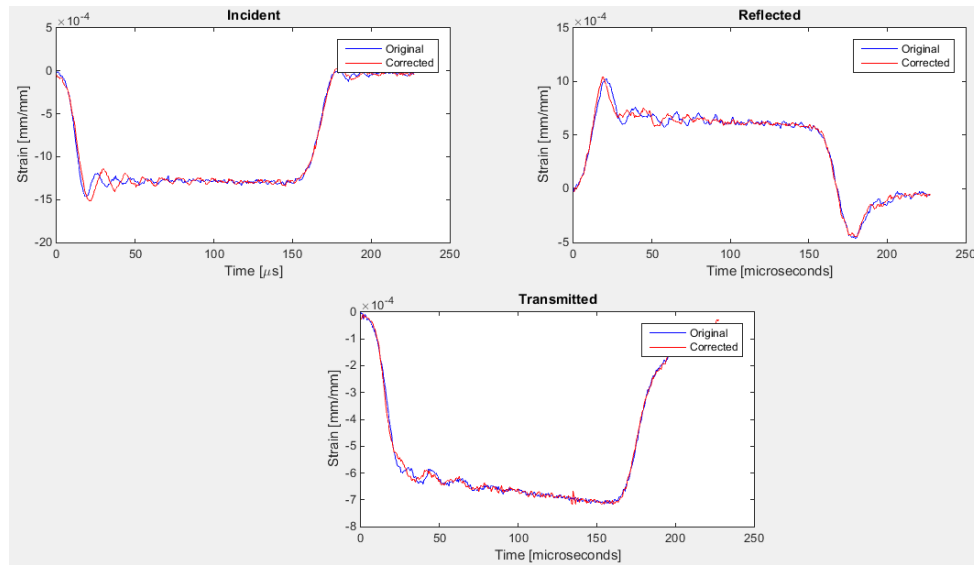


Figure 31. Original and corrected incident, reflected and transmitted signals.

5.1.5. Effect of specimen geometry

Specimen geometry is one the most important factors that has influence on the accuracy of the results in SHPB tests. By selecting proper geometry, inertia and friction effects can be reduced. That results in a better stress equilibrium state. [13]. Regarding to inertia, it introduces radial stress components in the stress state. According to Bertholf et al. [51], the effects of inertia become more severe at higher strain rates. At high strain rates, variations in stress and strain increase and that produces oscillations in the stress-strain curves due to the short rise time of the loading stress wave. Therefore, increasing the rise time of the loading pulse, it is possible to reduce inertial oscillations. Some authors have proposed expressions to estimate the effects of inertia. Davies and Hunter [52] proposed an

expression (equation 54) which allows calculating the approximate increase in stress (δ) due to inertial effects:

$$\Delta\sigma = \rho_s \left(\frac{L_s^2}{6} - \frac{v_s^2 d_s^2}{8} \right) \frac{d^2 \varepsilon}{dt^2} \quad (54)$$

where ρ_s is the density, L_s the length, v_s the Poisson's ratio and d_s the diameter of the specimen, respectively. By differentiating the expression, it is found that the expression for the optimum specimen length-to-diameter ratio is the one presented in equation 55.

$$\frac{L_s}{d_s} = \frac{\sqrt{3v_s}}{2} \quad (55)$$

This L_s / d_s ratio leads to insignificant effects of inertia. In contrast, according to Gorham [53], there is no L_s / d_s ratio that cancels absolutely the effect of inertia, but using specimens smaller than 1 mm the inertial effect can be reduced to insignificant levels.

Figure 32 illustrates the effects of an excessive friction. As it can be observed, if friction is too high, the stress state generated on the sample is not uniaxial due to some stresses that appear on the surface. Due to those stresses the specimen acquires barrel shape. Studies regarding the effect of friction in the interfaces specimen-bar have been also performed. Bertholf et al. [51] demonstrated that the higher is the friction coefficient at the interface, the higher are the stresses needed to deform the specimen and that the stress state in the specimen becomes multidimensional. However, these frictional effects can be minimized by selecting proper L_s / d_s ratio, by using specimens and bars with smooth ends and by using appropriate lubricants.

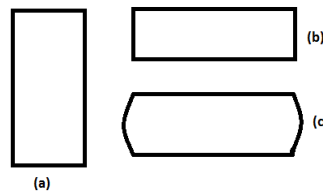


Figure 32. Effect of excessive friction in a Quasi-static compression test. (a) Original specimen shape (b) Shape after test performed without friction (c) Barrel shape of the specimen due to excessive friction

Researches have been made to determine the optimal L_s / d_s ratio that minimizes simultaneously both, frictional and inertial effects. Specimen should be short enough to achieve equilibrium stress state in a time shorter than the test duration, but long enough to minimize the influence of friction. Based on those ideas, Davies and Hunter [52] proposed that the optimal L_s / d_s ratio is approximately 0.5 for steels. Additionally, Keplaczko and Malinowski [54] found that the L_s / d_s ratio is also related to the ratio σ / ρ_s , as it is shown in equation 56:

$$\frac{L_s}{d_s} = \left[\frac{2\mu\sigma}{\rho_s d_s^2 (\dot{\epsilon}^2 + \ddot{\epsilon})} \right]^{1/3} \quad (56)$$

5.2. High Velocity Particle Impactor system

5.2.1. Description of the HVPI equipment at TUT

The High Velocity Particle Impactor (HVPI) equipment used in the current study has been developed at the Tampere Wear Center (TWC) of TUT. [55]. Using this HVPI system it is possible to shoot projectiles of different shapes, such as balls, cylinders or bullets made of different materials. Figure 33 shows a schematic view of the device.

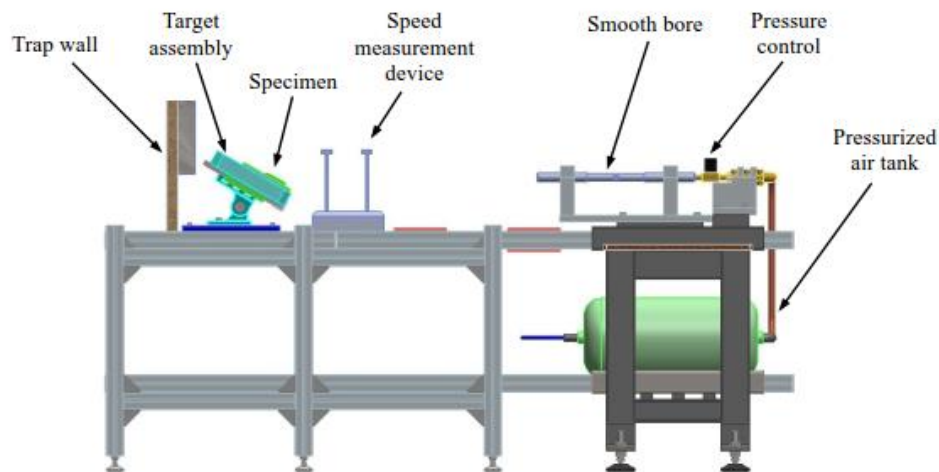


Figure 33. Schematic view of the High Velocity Impactor at TWC. [55]

The equipment has a barrel with a 9 mm internal diameter, where the projectile is placed. The barrel is connected to a pressurized air tank, where the pressure can vary from 0.1 to 16 bar in the present setup. The pressure is controlled via a pressure valve, which is opened to launch the projectile. Depending on the pressure used for a particular test, the velocity reached by the projectile varies from 45 m/s for 1 bar to 145 m/s for 16 bar. The target assembly is placed at 1 m distance from the end of the barrel. This target assembly can be tilted from 0° to 90° within a tolerance of $\pm 1^\circ$, what allows performing tests using a wide range of angles. The specimen holder is placed over the target assembly, and using different specimen holders it is possible to test different types of samples. The velocity of the projectile is measured with a ballistic chronograph placed between the target assembly and the shooting barrel. The impact is also recorded using a high-speed camera. Pressurizing and shooting valves, the pressure level in the tank, the lighting and the video recording system of the equipment are computer controlled to ensure timing and repeatability. The diameter of the balls used in these tests is 9 mm, which is bigger than the usual diameter used in erosion tests, because they should be large enough to be recorded using the high-speed camera. In addition, as the projectile is bigger, higher amount of energy is transferred to the target surface and the erosion crater is bigger, which simplifies its optical analysis and the post-impact analysis of damage mechanisms. [55].

5.2.2. Crater characterization

Figure 34 shows an oblique impact against a target surface and all the processes involved in it. According to M. Lindroos et al. [3], there are three different regions that can be distinguished after an impact. Region i) represents the elastic-plastic region, in which frictional contact takes place, leading to absorption of energy. Region ii) is known as the pile-up region. High strains and strain rates are located there due to high shear deformation. As a result, adiabatic shear bands can appear within it. Finally, region iii) is located in the interface ball-target material. Due to friction and the heat generated, there can be changes in a thin layer on the surface. In this region, also ploughing occurs, leading to the loss of some wear particles.

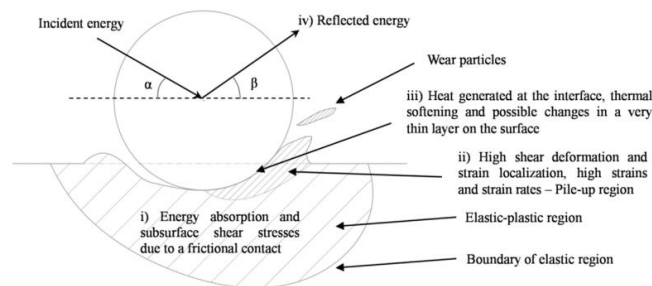


Figure 34. Deformation and different regions as the result of a sphere impacting on a target material. [3]

6. EXPERIMENTAL PROCEDURES

The main purpose of this work is to characterize the behavior of two ultra high strength steels against impact. Different testing procedures have been accomplished in order to test the materials through a wide variety of strain rates. Quasi-static compression testing is used for low strain rates (10^{-3} s^{-1} to 1 s^{-1}), while higher strain rates (up to 3600 s^{-1}) are tested by Compression Hopkinson-Split Pressure Bar system. Table 4 shows the different strain rates tested regarding the testing method used and the number of tests performed. Impact tests have been also performed using a HVPI device using different parameters and impact velocities, which are summarized in Table 5. Additionally, the material has been characterized in terms of microscopy and hardness testing. In the following, the procedures that have been followed are explained in order to allow repeatability, while the theoretical explanation of the different methods is presented in the previous Section.

Table 4. Compression tests performed for mechanical characterization.

	Quasi-static testing	Split Hopkinson Pressure Bar
Strain rates (s^{-1})	10^{-3}	700
	10^{-2}	1100
	10^{-1}	2400
	1	3600
Number of tests	2 per strain rate and material	

Table 5. Different impact energies and conditions used for impact testing.

	Dry	Oil	Work hardened	Subzero
Impact energy (J)	6,17,27,36			
Number of tests	2 tests per impact energy, condition and material			

6.1. Test materials

As previously mentioned, materials used in this study are two different ultra high strength steels (UHSS). Table 6 presents their maximum composition. Both steels are used in various applications of mechanical engineering. As it is shown in Table 6, the materials are slightly differently alloyed to achieve the properties that suit better their specific applications.

Table 6. Maximum composition of the studied ultra high strength steels.(wt %).

	C	Si	Mn	P	S	Cr	Ni	Mo	B
UHSS 1	0.23	0.8	1.7	0.025	0.015	1.5	1	0.5	0.005
UHSS 2	0.25	0.7	1.5	-	-	1	2	0.7	0.005

Figure 35 presents the microstructure of both materials after etching the surface with a 4% Nital solution for several seconds. Images were taken using a Nikon Eclipse MA 100. Both materials show a microstructure formed primarily by lath martensite, since the martensite is lath-shaped and oriented in groups in the same direction and there is a minor amount of retained austenite. Both materials contain also different amounts of untempered martensite, but its presence is more noticeable for UHSS 1. The presence of untempered martensite, which appears white after etching, leads to higher strength but simultaneously to lower toughness. Grain size is almost equal in both materials, being slightly finer for UHSS 1. Finer grain size improves the strength of the material.

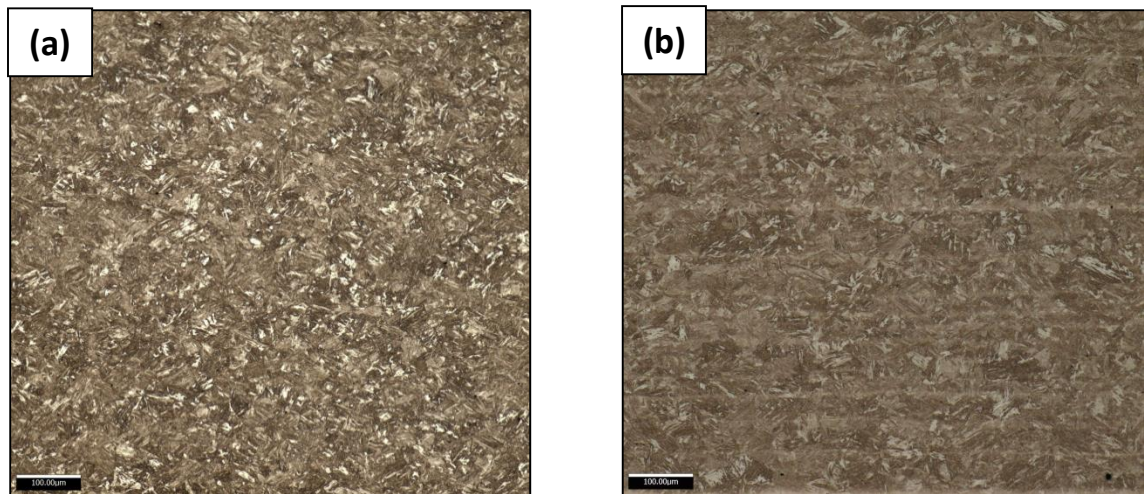


Figure 35. Microstructure of (a) UHSS 1 and (b) UHSS 2.

6.2. Quasi-static compression testing

6.2.1. Sample preparation

Cylindrical shaped specimens were used for both materials. Table 7 contains the main dimensions, i.e., diameter d , height h and height-to-diameter ratio, of the samples used in quasi-static compression testing for both materials. It is worth to mention that same sample dimensions were used for SHPB in order to enhance the comparability of the results. Firstly, cylinders were cut from a bigger plate in a way that the thickness of the plate became the height of the cylinder. Additionally, the ending surfaces of the specimen that were going to be in contact with the compression plates were ground in order to remove any oxide layer and achieve proper surface flatness and parallelism.

Table 7. Dimensions (diameter d , height h and height-to-diameter ratio h/d) for samples used in quasi-static compression testing and SHPB.

	d	h	h/d
UHSS 1	6	6	1
UHSS 2	6	7	1.17

6.2.2. Test procedure

Low strain rate testing was performed using an Instron 8800 servohydraulic materials testing machine. Figure 36 shows the configuration of the Instron 8800 machine. Materials were tested for four different strain rates: 10^{-3} s^{-1} , 10^{-2} s^{-1} , 10^{-1} s^{-1} and 1 s^{-1} and always at room temperature. The tests were repeated twice per each strain rate to ensure the repeatability of the results.



Figure 36. Instron 8800 servohydraulic materials testing machine.

The specimen was placed between the compression plates. The force was measured with a 100 kN Instron load-cell and the strain was measured using an extensometer that was attached to the compression plates by rubber bands. As shown in Figure 37, for practical reasons, the extensometer covered a length larger than the specimen, i.e., parts of the compression plates were included in the extensometer gauge length. However, assuming that the compression plates do not deform, it is possible to consider that the displacement measured by the extensometer coincides with the sample deformation. Additionally, a layer of MoS₂ grease was applied on the interfaces specimen-compression plates to minimize friction.

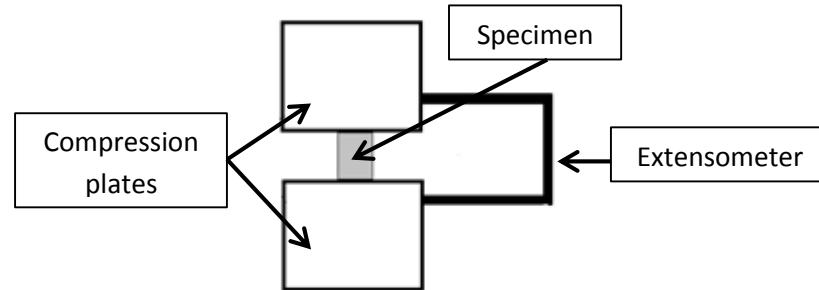


Figure 37. Setup for measuring specimen strain in quasi-static compression test.

Once the sample was correctly placed, the compression heads were pressed together until both ending surfaces of the specimen were in complete contact with them. Tests were conducted controlling the displacement, which allows ensuring constant strain rates. While the test is performed, data is stored. The number of data points obtained for every test is the one included in Table 8.

Table 8. Number of data points obtained in quasi-static compression testing depending on the strain rate

Strain rate (s ⁻¹)	10 ⁻³	10 ⁻²	10 ⁻¹	1
Number of data points	2500	4500	4500	2000

6.3. Split-Hopkinson Pressure Bar system

6.3.1. Sample preparation

As mentioned above, in order to be able to compare the SHPB results to the quasi-static testing results, the specimens used for both tests had the same geometry, shown in Table 8. However, for SHPB testing, a more careful preparation of the samples was needed because the procedure is based on wave propagation. Specimen faces that were loaded were perfectly flat, parallel with each other and with no rust or scratches, so the contact in the interfaces specimen-bar was as good as possible. In that way, wave dispersion was minimized and wave propagation could be considered one-dimensional, which will lead to more reliable results. In order to produce a good surface quality, the samples were ground until parallelism and proper roughness were achieved. Additionally, the pressure bars of the apparatus were carefully aligned.

6.3.2. Test procedure

A detailed description of the SHPB system used in this study and its operation is given in Section 5.1. First of all, the specimen was placed between the incident and transmitted bars. Due to the high strength of the tested materials, high resistant metallic inserts were placed in the specimen-bar interfaces as shown in Figure 38. Those inserts protect the bars from any damage as a result of the test. It is worth to mention that the inserts should be taken into consideration during the data processing as space and time lost for the waves while travelling through the bars to the specimen. Some grease was applied on the insert-bar and specimen-insert interfaces to reduce friction and assure one-dimensional testing.

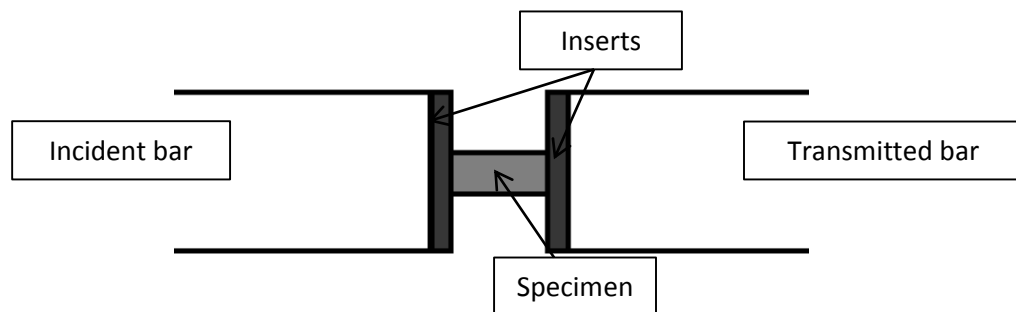


Figure 38. Basic setup of the specimen for SHPB testing.

Once the sample is correctly placed the rest of operations are computer controlled. Figure 39 illustrates schematically the flow of the information during the test. First, the striker is loaded and, afterwards, the pressure necessary for the striker to reach a specific velocity is set. The pressure is loaded in a pressure accumulator and released when the striker is to be launched. During the test the stress waves, as well as the velocity of the striker, are recorded. Two optical sensors mounted at the end of the launcher tube allow obtaining the velocity of the striker. The stress waves are registered by two pairs of strain gages attached to the incident and transmitted bars. The signals from the strain gages need to be amplified before reaching a digital oscilloscope where they are recorded. The data acquired by the oscilloscope is transferred to a computer where, using a Matlab code, the data is processed. As a result of the calculations, all information related to stress, strain and strain rate in the specimen are obtained. As explained in Section 5.1.4 some adjustments are included in the Matlab code to correct for the wave dispersion.

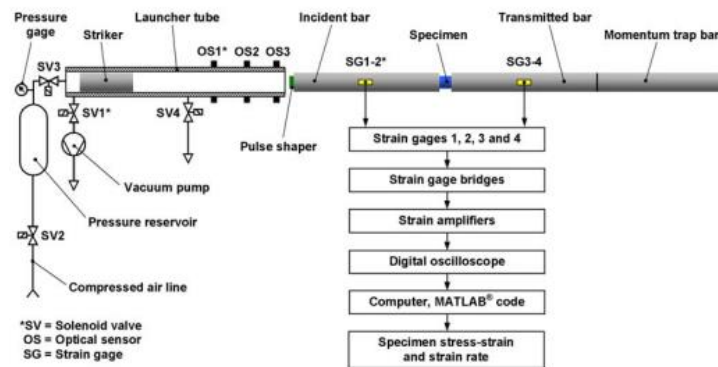


Figure 39. Schematic of the SHPB equipment at TUT. [12].

6.4. High Velocity Particle Impactor

As shown in Table 5, four different types of experiments were performed using the HVPI. Firstly, the dry-impact test, without any modifications on the specimen surface, was conducted. Secondly, an oil layer was placed on the specimen's surface in order to study its effects on wear and volume loss. Also some work hardening was done on the surface. Finally, some tests were conducted at -20°C to study the effect that temperature has on wear.

6.4.1. Sample preparation

The dimensions of the target assembly of the HVPI determine the size of the samples. According to them, specimens should be 40 mm x 40 mm square plates. Both materials were received as square plates of 200 mm x 200 mm with 6 mm thickness for UHSS 1 and 7 mm for UHSS 2. Hence, suitable sample sizes were prepared from the larger plates. Afterwards, the surfaces were ground, in order to remove the decarburized layer that forms during manufacturing. After grinding, the surfaces were polished with a 1 μ m cloth, which ensured mirrored surface, which is necessary to study the actual impact effects, such as volume loss.

6.4.2. Test procedure for dry tests

The test procedure explained in the following was applied to all performed impact tests. WC-Co balls of 9 mm of diameter and 5.70 g weight were used as projectiles. The balls hit the target surface with energies ranging from 6 to 36 J. Different launching pressures result in different impact velocities and, therefore, different impact energies. Table 9 shows the used launching pressures and their consequent impact velocities and energies. As mentioned above, tests were performed twice per pressure. Also, Figure 40 shows the top view of the impact craters formed at different impact velocities. As it is shown the higher is the pressure and, therefore, the impact velocity and impact energy, the larger is also the impact crater.

Table 9. Impact velocities for the different pressures used on HVPI testing.

	Pressure			
	2 bar	6 bar	10 bar	14 bar
Impact velocity (m/s)	45	78	98	112
Impact energy (J)	6	17	27	36

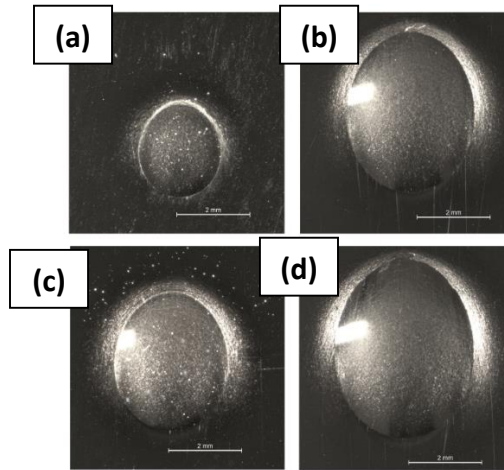


Figure 40 Marks on specimen surface for impacts at: (a) 45 (b) 78 (c) 98 and (d) 112 m/s.

Specimens were fixed to the target assembly so that the rolling and impact direction were coincident. Two impacts were performed per sample at different locations, in such way that different pressures were used for each hit. This reduces the effect of possible random flaws in one specimen. As the name implies, dry tests were conducted in dry conditions, which means that there was no lubrication on the surface of the specimen or on the ball. In Figure 41 it is possible to observe the instant at which the ball impacts the surface of the specimen and the mark produced on it.

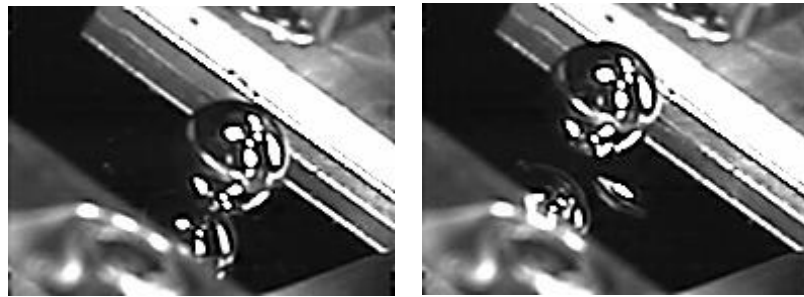


Figure 41. HVPI dry test a) WC-Co ball impacting the specimen (b) Ball leaving the specimen after the impact

Additionally, the impacts were recorded for post-processing using a high-speed camera with 40 000 frames per second. Through an image analysis of the recorded images it is possible to calculate the exit velocity. Knowing both, impact and reflected velocities, it is possible to calculate the dissipated energy as the difference between the impact kinetic energy and the reflected kinetic energy. Equation 57 allows the calculation of the dissipated energy, in which m_p represents the mass of the projectile, v_i , the impact velocity and v_r , the reflected velocity.

$$E_d = \frac{1}{2}m_p(v_i^2 - v_r^2) \quad (57)$$

6.4.3. Test procedure for oil layer tests

In contrast to dry testing, in these tests an oil layer was placed on the specimen surface. The oil selected for the tests was an oil from Mobilgear SHC SMP Series, a synthetic industrial gear box oil designed to work under extreme conditions, especially for heavily loaded gearboxes. Main properties of the oil are presented in Table 10.

Table 10. Properties of gear oil used for HVPI testing

ISO Viscosity Grade	Viscosity at 40 °C (cSt)	Viscosity at 100 °C (cSt)	Pour Point, °C, ASTM D 97	Flash Point, °C, ASTM D 92
320	335	38,3	-38	242

In general, the procedure was exactly the same as in the cases of dry conditions. However, the oil layer was applied on the specimen before shooting. After the specimen was fixed to the target assembly some oil drops were poured carefully on the surface. Several seconds were needed until an evenly oil layer was formed. In practice, it is not possible to measure the thickness of the oil layer. However, in these early stages of the study that information was not considered necessary since the purpose was only to determine if the lubrication has any effect on impact wear. Equal test parameters as in the dry-impact tests were used to ensure comparability (Table 5). Therefore, the impact velocities were also the on the same level. Figure 42 shows the impact of the ball on a specimen with an oil layer on its surface.

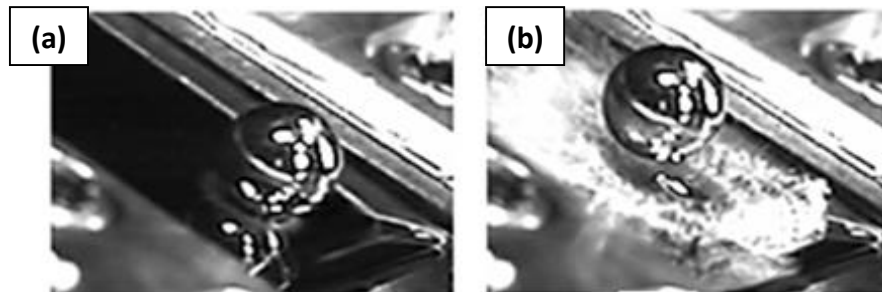


Figure 42. HVPI oil test a) WC-Co ball impacting the specimen (b) Ball leaving the specimen after the impact

6.4.4. Test procedure for work hardened tests

Prior to testing, the hardness of the sample surface was increased by cold working. Thus, a work hardening device [56] was attached to a quasi-static testing machine (Instron 8800). Figure 43 shows the used equipment. As it can be observed, the device consists of a pin holding an indenter, which is pressed against the surface, and two pairs of guides, which allow moving the sample in both perpendicular directions. In each pair only one of the guides is motorized, while the other has a spring. The sample is moved forward by the motor and backward by the force supplied by the spring. Those movements are controlled by a computer.

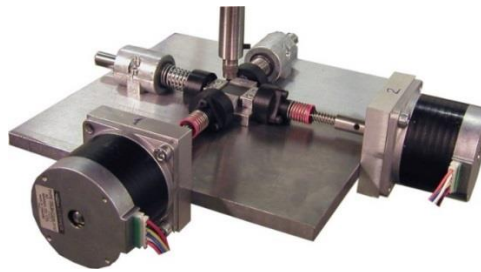


Figure 43. Work hardening device.

Figure 44 illustrates how the work hardening device was attached to the quasi-static testing machine. As shown, the pin was held by the hydraulics grips of the device and was supported by two preload springs. The indenter was a bullet of 9 mm diameter, same diameter than the ball used in the HVPI test. As the materials tested were initially very hard, the circular mark obtained after pressing the 9 mm indenter against the surface was about 1.5 mm in diameter for the first cycles and it decreased as the hardness of the surface increased. The work hardened area was approximately 15x15 mm, which is large enough to assure that the ball during the HVPI test will strike within it. The surface needed to be pressed high number of times with a specific compression force to obtain the aimed hardness. The preloaded springs are designed to support the force provided by the machine in a way that the contact between the pin and the surface is ensured. This force needed to compress the springs should be taken into account in order to know the actual force applied on the sample. Equations 60 to 68 shown later show how to calculate the actual force applied. To obtain an even resulting hardness on the surface, it is necessary to assure that the movement of the sample is so that the whole area is reached. Thus, friction needs to be reduced as much as possible. For that reason, all surfaces were polished and some lubricant was added on the sample-device interface.

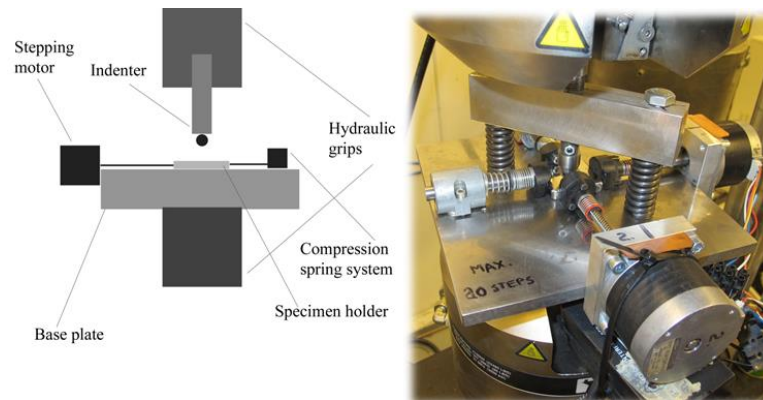


Figure 44. Work hardening device attached to the servohydraulic testing machine.

Most of the samples were hardened using 22 000 cycles with 3 kN of compressive force. However, to further study the effects of work hardening, longer treatments were performed for UHSS 1, that is, 50 000 and 100 000 cycles. Table 11 shows the number of work hardened samples, while Table 12 contains the resulting hardness. Despite the different durations of the work hardening treatments, the used force was 3kN for all cases, in order to simulate real working conditions, i. e. low loads applied for a high number of times.

Table 11. Number of work hardened samples for both materials according to the number of cycles applied.

	UHSS 1			UHSS 2
	22000 cycles	50000 cycles	100000 cycles	22000 cycles
Number of samples	8	1	1	8

Table 12. Original and obtained hardness for both materials after work hardening.

		UHSS 1			UHSS 2
		22000	50000	100000	22000
Hardness	Original (HV)	430	430	430	450
	Work hardened (HV)	630	700	780	655
	Increase (%)	46	60	80	45

After work hardening, an area of about 15 x 15 mm is obtained. Figure 45 shows the complete area after 20 000 and 100 000 cycles applied. As it can be observed the appearance of the surface and its roughness is strongly affected by the number of cycles used. Figure 46 contains detailed images of the surfaces after 20 000, 50 000 and 100 000 cycles, respectively. After 20 000 cycles (Figure 46 a), it is possible to observe the marks produced by the indenter. A strong roughness has developed but no removal of material can be noticed. However, as the number of cycles increases more material is removed from the surface due to the formation of thin flakes. Those flakes start to be noticeable at 50000 cycles (Figure 46 b) and their amount has considerably increased after 100 000 cycles (Figure 46 c).

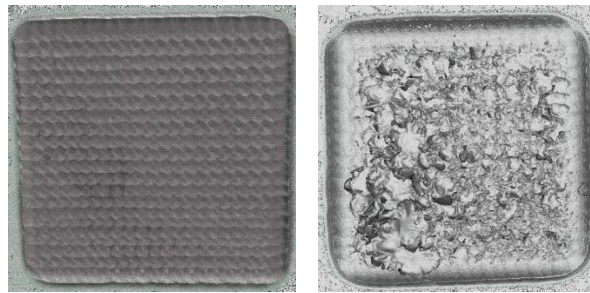
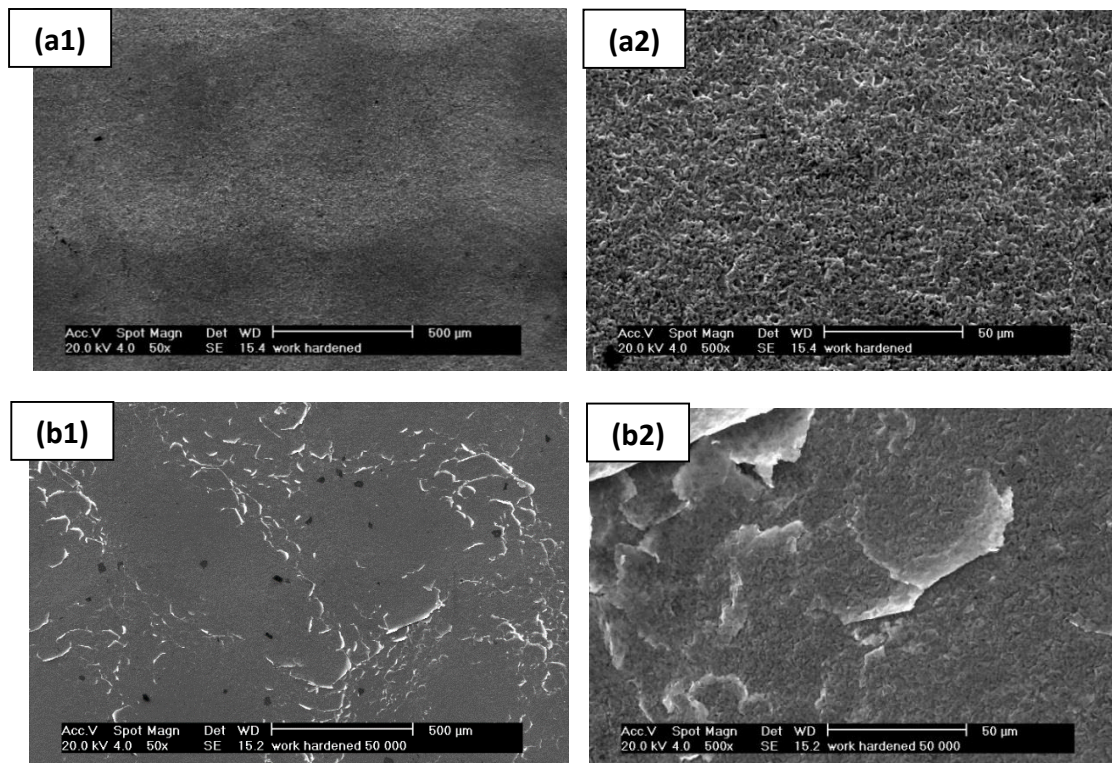


Figure 45. Top images of the work hardened area after 20 000 cycles (left) and 100 000 cycles (right).



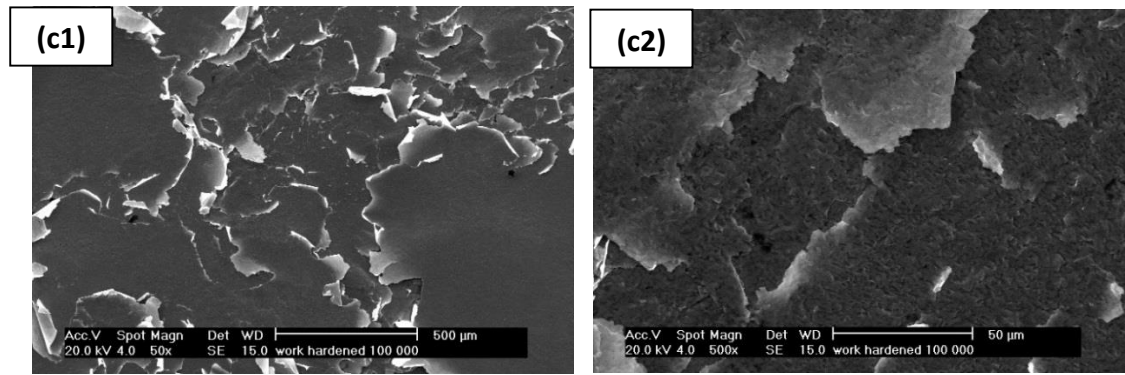


Figure 46. Detailed images of the work hardened surface after (a1) and (a2) 20 000, (b1) and (b2) 50 000 and (c1) and (c2) 100 000 cycles obtained by a SEM

It is also worth to mention that during the work hardening treatment the microstructure of the material was also affected as it underwent different levels of plastic deformation. Figure 47 shows the different grain structure at different distances from the surface. About 200 micrometers below the surface the material shows finer grain structure. There is also a transition zone between the unaffected bulk material and the severely deformed material close to the surface. According to this deformed microstructure distribution, the hardness of the material increases from the bulk material to the surface.

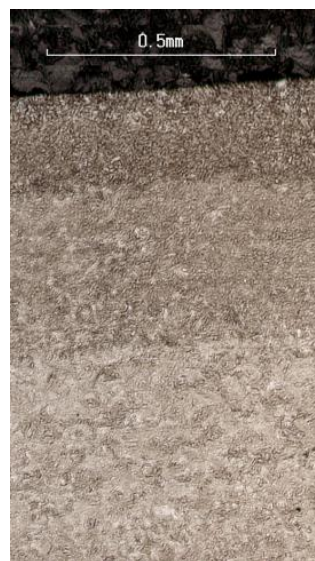


Figure 47. Differences in the microstructure in the cross section of a work hardened sample.

In the following, the equations used to calculate the actual force compressing the sample are presented. First of all, it is necessary to calculate the value of the spring constant, k_s . According to Hooke's Law, Equation 58, the force needed to compress a spring for a distance, x_s , is proportional to the spring constant. It is important to notice that x_s is the distance that the spring is compressed. However, the quasi-static testing machine only provides the acting force and the position of the actuator. As it is shown in Equation 59, it is possible to calculate the value of x_s as the difference of the displacement obtained from the machine in a point i , d_i , and a reference displacement d_0 taken when the spring is fully unloaded.

$$F_s = k_s x_s \quad (58)$$

$$x_s = d_i - d_0 \quad (59)$$

Taking force and displacement in two points and expressing them as a combination of Equations 58 and 59, it is possible to obtain Equation 63, which allows calculating the spring constant.

$$F_{s1} = k_s x_{s1} = k_s (d_1 - d_0) \quad (60)$$

$$F_{s2} = k_s x_{s2} = k_s (d_2 - d_0) \quad (61)$$

$$F_{s1} - F_{s2} = k_s x_{s1} - k_s x_{s2} = k_s (d_1 - d_0) - k_s (d_2 - d_0) \quad (62)$$

$$k_s = \frac{F_{s1} - F_{s2}}{d_1 - d_2} \quad (63)$$

Once the spring constant is known, it is possible to know the deflection of the spring at the initial moment of the test, designated as x_0 , because the force at the initial moment, F_0 , is also known.

$$x_0 = \frac{F_0}{k_s} \quad (64)$$

Finally, the actual force applied by the indenter at any moment of the test, F_a , can be expressed as the force measured by the device, F_m , less the force spent to deflect the spring, F_s . This force, F_s , depends on the distance that the spring is compressed, x_i , which can be expressed as the sum of the initial compression and the extra compression undergone by the spring to reach the actual position. The extra compression can be obtained as the difference between the original displacement of the piston and the actual one, as it is shown. The final expression of the actual force applied is presented in Equation 66.

$$F_a = F_m - F_s = F_m - [k_s x_0 + k_s x_s] = F_m - [k_s x_0 + k_s (d_i - d_0)] \quad (65)$$

$$F_a = F_m - [k_s x_0 + k_s (d_i - d_0)] \quad (66)$$

Once the sample is ready, the HVPI testing procedure is similar to the one for dry and oil tests. The samples hardened with 20000 cycles were shot using the same pressure levels than in the previous tests, and all tests were performed twice per each pressure in order to make comparison possible. However, for the previous tests the same sample was shot twice using two different pressures, but for the work hardened samples this was not possible due to the smaller area available. Therefore, each sample was only shot once. Finally, both extra-hardened samples, i.e. after 50 000 and 100 000 cycles, were shot only at impact velocity of 78 m/s due to the small thickness of the hardened layer. At this velocity it is possible to observe clearly the damage on the surface, but the energy is not enough for the ball to penetrate to the bulk material, where the work hardening did not have any effect. Figure 48 shows the moment of the impact for a work hardened sample.

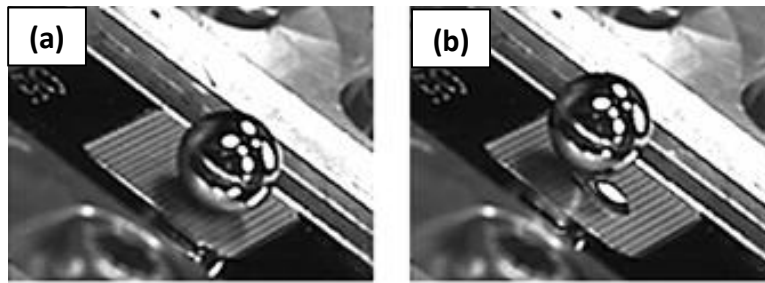


Figure 48. HVPI testing for work hardened samples (a) WC-Co ball impacting the surface (b) ball leaving the surface after the impact.

6.4.5. *Test procedure for -20°C tests*

Prior to testing, once the samples were polished, two thermocouples were welded at both sides of each sample near the impact area. With these thermocouples it was possible to monitor the temperature of the sample during the test. As an initial attempt, the sample was placed inside a freezer until its temperature was about -20 °C. However, due to the small mass of the specimen, it would warm very quickly when taken out of the freezer. Therefore, to avoid the fast warm up, the sample was attached to the specimen holder and the whole assembly was immersed in liquid nitrogen mixed with some ethanol. As a result the sample was cooled down close to -60 °C and when that temperature was achieved it was placed on the target assembly and the test was carried out. The procedure was done quickly so that the temperature of the specimen did not rise over -20 °C. The temperature was recorded by an oscilloscope through the thermocouples placed on the surface of the sample in order to know the exact temperature at the moment of the impact.

6.4.6. *Profiling and crater characterization*

To characterize the damage mechanisms undergone by the surface, the impact crater were studied by using an optical profilometer. The cross section was studied to identify changes in the microstructure and the appearance of features such as shear bands. Finally, detailed images of the surface of the impact crater were taken using a SEM. Figure 49 shows the profile and the topography of the crater formed on UHSS 2 after the impact of a ball at 98 m/s. As it can be observed, when the ball hit the surface of the specimen a crater was formed, leaving an “empty” volume on the surface, referred to as negative volume (below zero-plane defined from the undeformed surface). Part of the material that was occupying that volume was removed due to the wear produced by the impact, while the other part was displaced around the crater due to the plastic deformation caused, forming a pile-up. The volume occupied for the material displaced is referred to as positive volume (above the zero-plane). The volume loss, i.e., volume of the material removed, is calculated as the difference between the positive and negative volume.

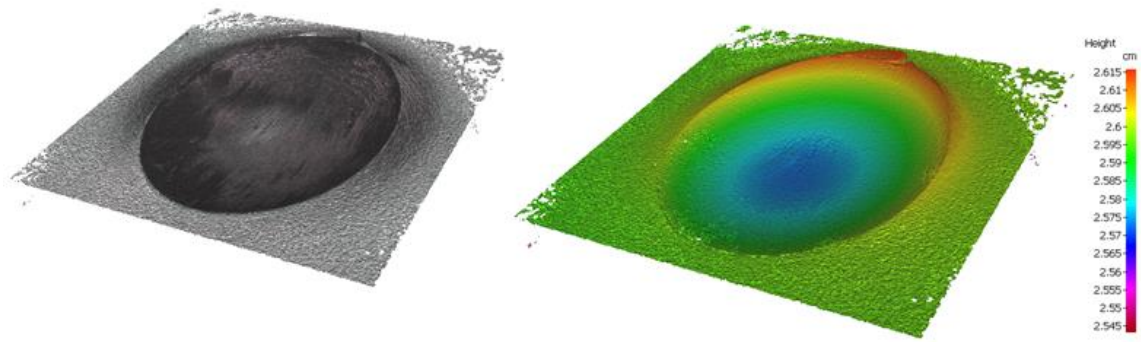


Figure 49. Profile and topography of the crater produced on UHSS 2 by the impact of a projectile at 98 m/s obtained with an optical profilometer.

All the results are based on the information regarding the volume loss and the energies involved in the impact. Volume loss is highly influenced by the amount of energy absorbed during the impact. Therefore, the ratio volume loss (or wear)-to-initial kinetic energy can provide useful information. Equation 67 shows the expression to calculate the cutting-to-plasticity ratio, φ , where V_{neg} represents the negative volume and V_{pos} the positive volume. This ratio provides information about the amount of material that has been removed from the surface and the amount that has been plastically deformed and its values range from 0 to 1. While φ equals 0 means that all the material has been plastically deformed and there is no material removed from the surface, φ equal 1 means that all the material occupying the volume is lost.

$$\varphi = \frac{|V_{neg}| - |V_{pos}|}{|V_{neg}|} \quad (67)$$

7. RESULTS AND DISCUSSION

In the following, the main results and observations made during the study are presented. Firstly, results regarding the microstructure and composition of both materials are shown. The mechanical behavior of the test materials was studied at different strain rates using a quasi-static testing machine and the Split Hopkinson Pressure Bar. Hence, the main mechanical properties and their dependence on the strain rate are presented as well. To evaluate the behavior of the materials against impact wear, impact testing was performed and the main results are shown below. Failure and damage mechanisms were identified by studying the impact craters and their cross section using a profilometer and a Scanning Electron Microscope (SEM).

7.1. Mechanical behavior results and strain rate dependence

7.1.1. *Compressive properties*

Compressive behavior of the materials was found to be dependent on the strain rate. For the majority of the strain rates plastic deformation occurred without fracture. However, for UHSS 2, specimens at 3600 s^{-1} strain rate fractured. Figure 50 shows the engineering stress vs engineering strain curves for both materials. Figure 51 shows the plastic behavior of both materials at the studied strain rates. Elastic regime was removed from the curve and only the true plastic strain region is shown, region within which the curves were smoothed with a second order polynomial. True stress values of stress and strain presented in Figure 51 are calculated from engineering values taking into account that the cross section of the sample increases as the sample is deformed. Larger cross sectional area leads to smaller stresses; therefore, true stress is smaller than engineering stress. Materials behave different depending on whether they are tested in the quasi-static or dynamic region. It is worth to mention that, as Figure 51 and 52 show, the difference between the values of stresses obtained at 10^{-3} and 3600 s^{-1} strain rates, respectively, is only about 10 %. Consequently, even though there is a clear dependence on strain rate, its effect is not very strong.

Higher values of strain rates result in higher values of true stress for lower values of strain. However, within the quasi-static region, when a certain strain level is reached the opposite effect appears so that the lowest strain rate (10^{-3} s^{-1}) leads to the highest true stresses. This can be explained through the strain hardening. As a result of strain hardening, the more the crystal is plastically deformed, the larger is the stress needed to further deform it. Strain hardening is defined as the slope of the stress-strain curve, $\frac{d\sigma}{d\varepsilon}$. According to this definition, positive slopes of the curves lead to strain hardening, whereas negative slopes mean strain softening.

Firstly, considering quasi-static testing region, the curves exhibit a clear strain hardening effect that decreases as the strain rate increases. Strain hardening is slightly more pronounced for UHSS 2. It is worth to note that the shape of the curves for UHSS 1 at strains lower than about 5 % differ slightly from the expected. First the strain hardening rate is very low and after 5 % of strain it increases rapidly. It appears that dislocation forest hardening [57], which usually causes strain hardening, is not very effective at the beginning of the test. Considering the complexity of the studied alloys, there might also be other mechanisms taking place. Their characterization is, however, out of scope of this work.

Concerning the dynamic testing, at strain rates between 700 and 3600 s^{-1} , the behavior of materials is considerably different. As the strain rate increases, the values of stress increase too. The main difference is found in the strain hardening rates. While at lower strain rates the materials become harder as they deform, at higher strain rates strong softening appears at strains higher than 0.1. The appearance of adiabatic shear bands could explain the softening observed at the highest strain rates. This is supported by calculations made using Equation 16, which predict the formation of adiabatic shear localizations at low strains (below 0.1) for both materials. In the calculations typical thermal properties of a mild steel were used ($\rho=7900 \text{ kg/m}^3$, $C_V=500 \text{ J/(kg K)}$, $T_0=300 \text{ K}$, $T_m=1800 \text{ K}$, $\beta=0.9$) and strain hardening parameters were found by fitting to the data shown in Figure 51 (for example, $A=1800 \text{ MPa}$, $B=160 \text{ MPa}$, $n=0.5$ for UHSS2 at 2400 s^{-1}).

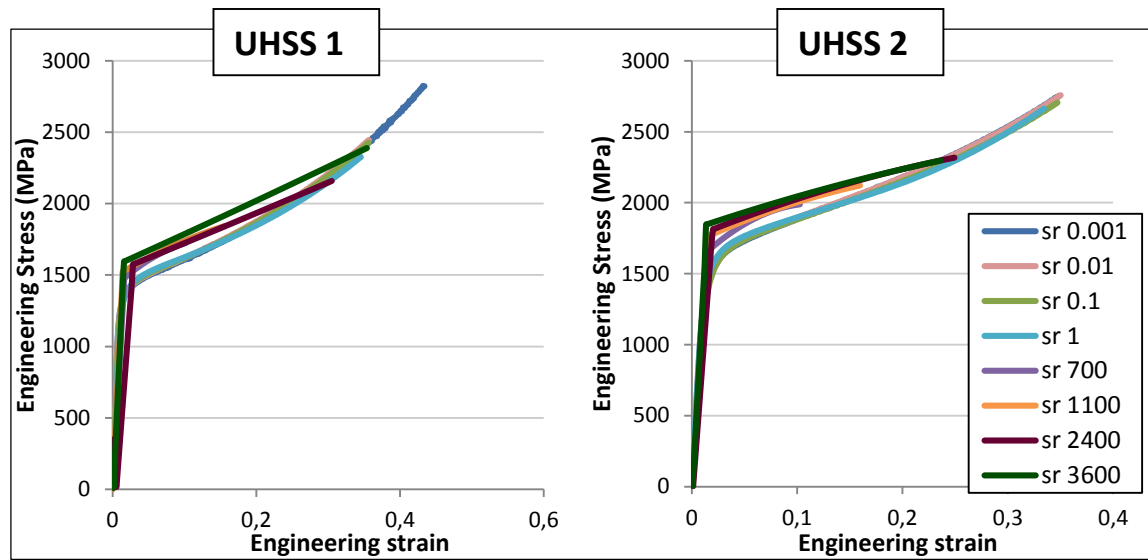


Figure 50. Engineering stress vs engineering strain at different strain rates in compression

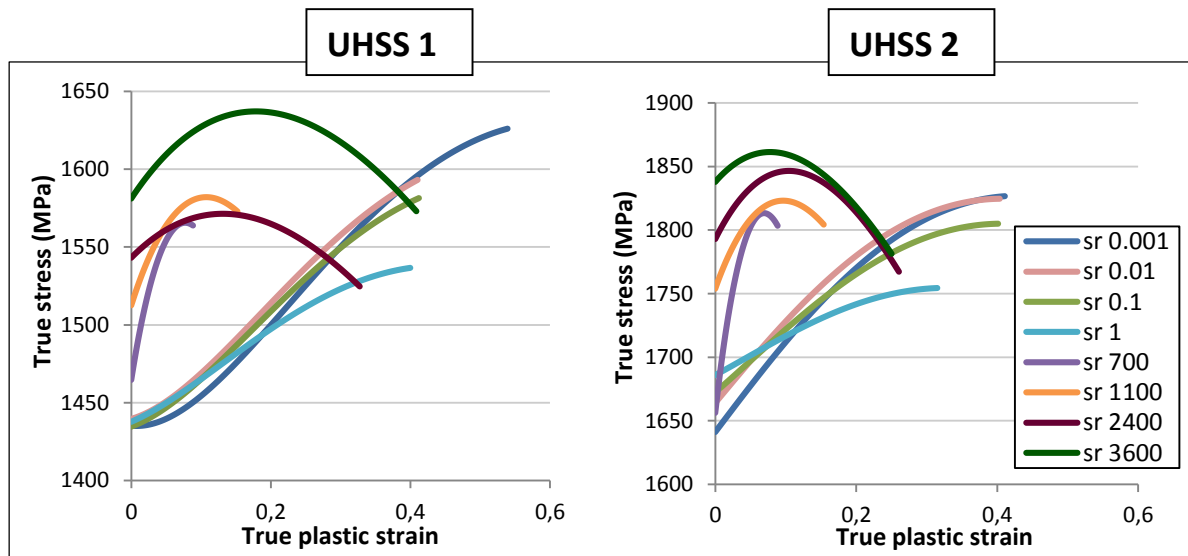


Figure 51. Behavior of the materials at different strain rates in compression.

Figure 52 presents the evolution of the flow stress at 1, 5 and 7.5 % of strain for all the studied strain rates. Strain rate has a clear influence and it is possible to distinguish two different behaviors which correspond to quasi-static and dynamic ranges. In the quasi-static region, the flow stress is almost independent of the strain rate. However, for strain rates higher than 10^3 s^{-1} , there is an increase of stress as the strain rate increases. It should be noted that the accuracy of the SHPB technique is limited at low strains [51], which may affect the low strain data in Figure 52.

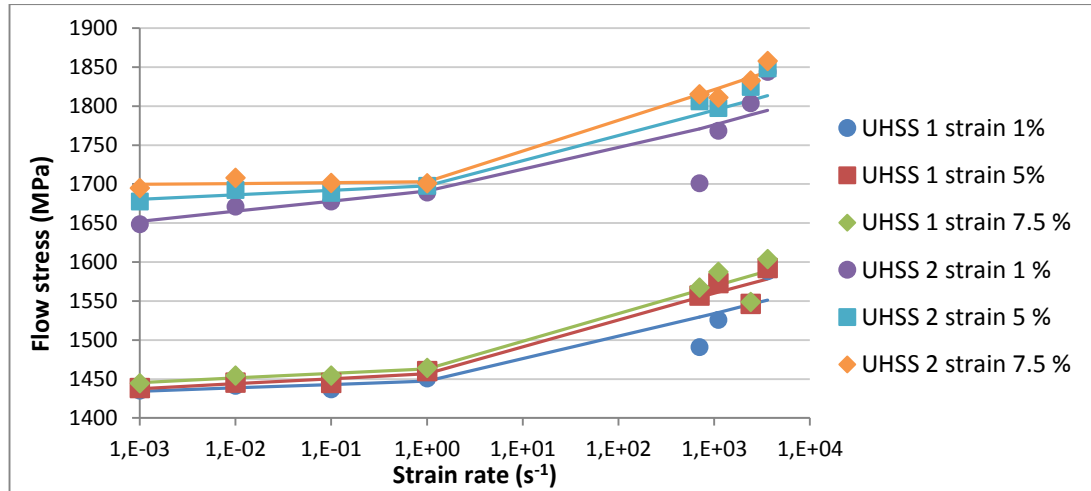


Figure 52. Stress and strain rate comparison for constant strains.

7.1.2. Impact testing

In the following, the results obtained at HVPI tests are presented. For each test the impact crater profiles were investigated by an optical profilometer and all the energies were calculated through post-processing of the high speed images.

Figure 53 shows a schematic view of a two-dimensional impact crater obtained by cutting the crater at the middle along the longitudinal impact direction. The highest point of the pile-up is mostly related to the amount of plastically deformed material, while the deepest point depends on the amount of both cut-off and deformed material. The diameter of the crater formed varies from 2.5 to 4 mm, which is about 25 to 45 % of the diameter of the ball used as projectiles. Figure 54 shows the two-dimensional profiles of the impact craters formed after a single oblique impact for different impact energies in tests performed at dry conditions. As expected, the results show that depth, as well as height, are strongly dependent on the impact energy. As the impact energy increases, both depth and height increase abruptly. Both materials exhibit the same behavior when tested at other conditions.

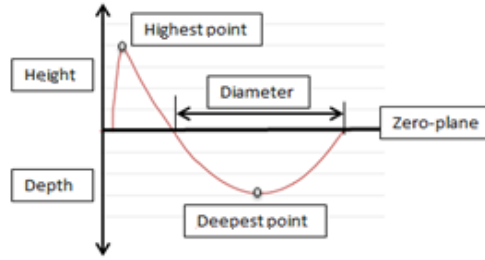


Figure 53. Diameter, depth and height of an impact crater.

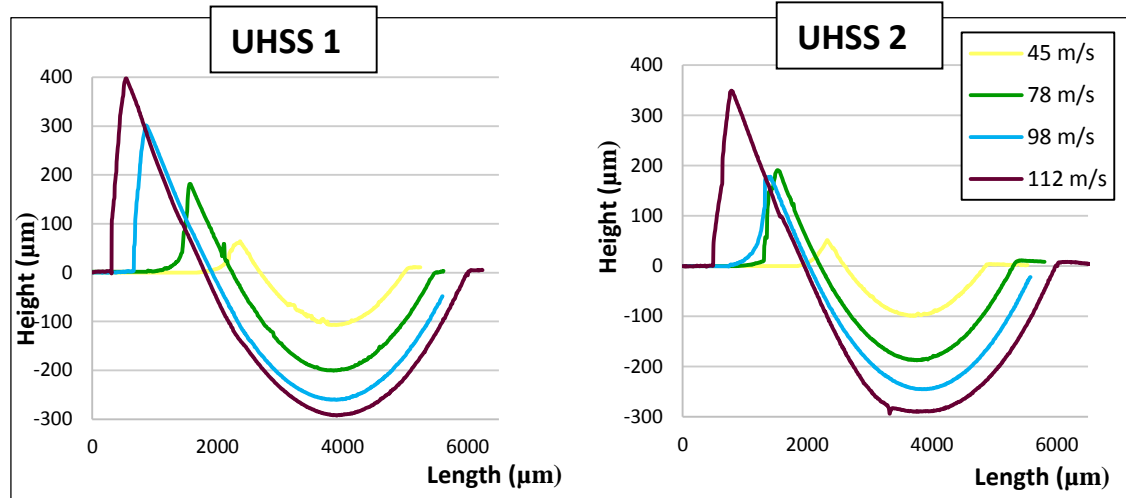


Figure 54. Two-dimensional profiles of the impact craters formed by an oblique impact at 30° for different impact energies in dry-impact conditions. (Impact direction from right to left)

Comparisons of the two-dimensional profiles of the impact craters for all tests are shown in Figure 55 and 56 for UHSS 1 and UHSS 2, respectively. According to Lindroos et al. [3], the depth of the crater and the height of the formed pile-up depend on the impact angle, and on whether the energy is consumed in cutting or deforming the material. They found that impacts at 30° produce larger pile-ups than any other impact angle. The height of the pile-up is related to the amount of plastically deformed material and, therefore, to the amount of energy spent during deformation. The bigger is the pile-up, the more material has plastically deformed. The results show that diameter and depth are very alike at all conditions. However, for the highest point of the pile-up there is not a clear trend. Some authors have used the relation between the deepest and highest point expressed as $R_i = \frac{d_{max}}{h_{max}}$ to characterize wear on impact craters. However, R_i considers only one two-dimensional section of the crater and, consequently, it does not represent the whole pile-up and crater. Therefore, as mentioned in Section 5.2.2, the best way to characterize the wear at the craters is by the cutting-to-plasticity ratio, which is discussed below (Figure 57 c).

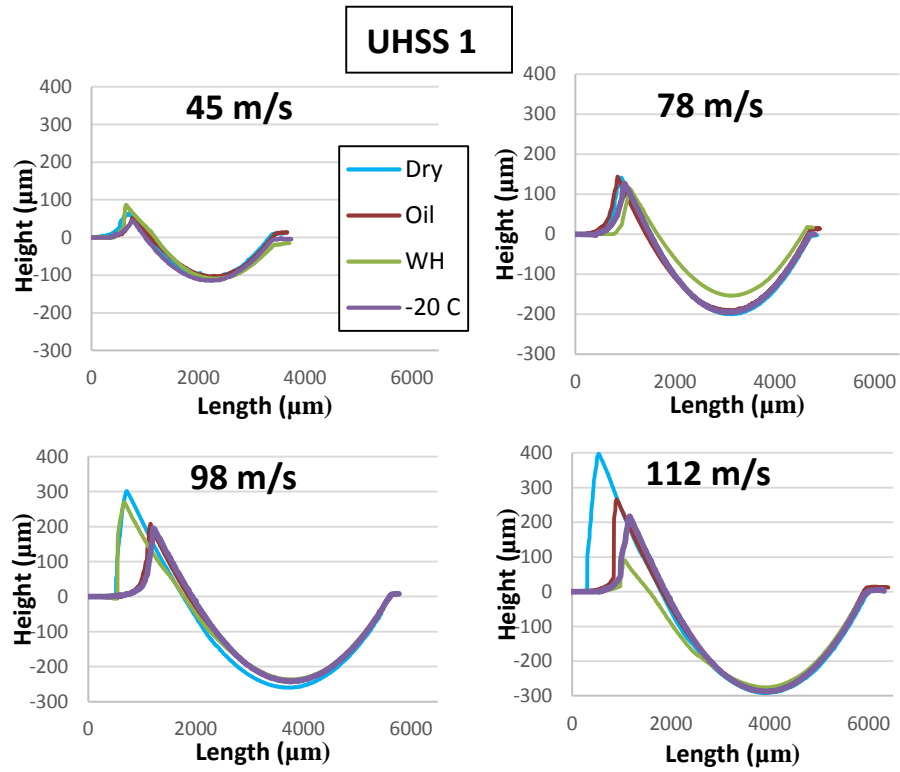


Figure 55. Comparison of two-dimensional profiles of the impact craters formed on UHSS 1 by an oblique impact at 30° for all test conditions and energies used. Impact direction from right to left.

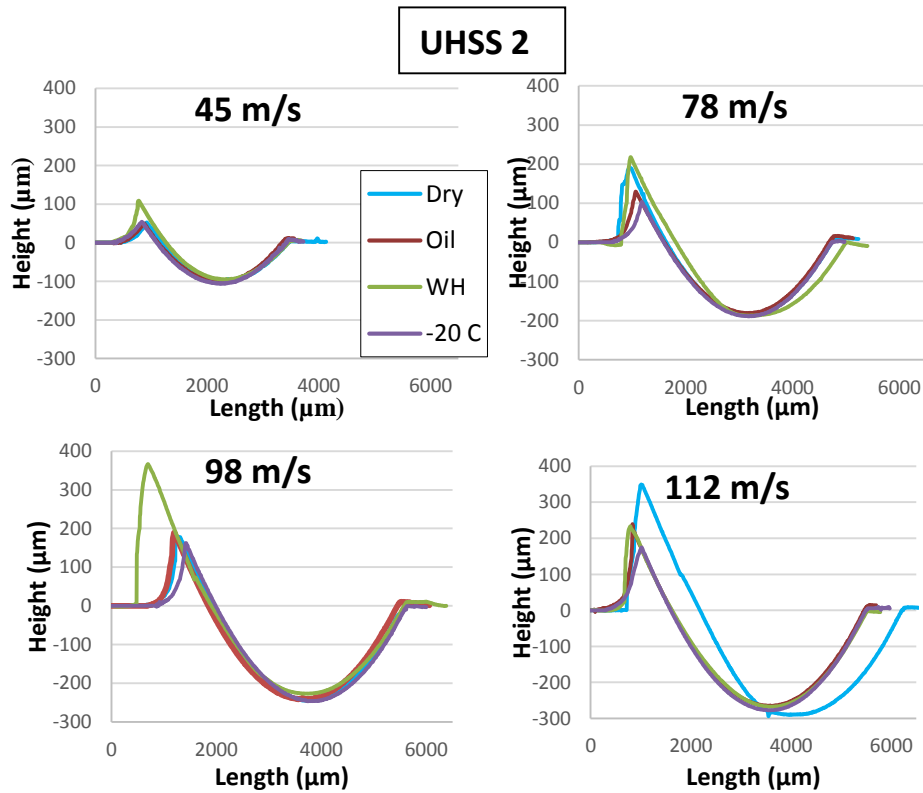


Figure 56. Comparison of two-dimensional profiles of the impact craters formed on UHSS 2 by an oblique impact at 30° for all test conditions and energies used. Impact direction from right to left.

Calculated impact energies help to support the fact that work hardening helps to reduce volume loss, while low testing temperature and lubrication lead to a higher level of wear. Figure 57 shows the ratio dissipated/impact kinetic energy as a function of the impact velocity. Higher values of dissipated energy lead to more damage produced on the surface. However, the dissipated energy can cause two different damages, such as cutting-off of material and plastic deformation. As the percentage of energy spent in each mechanism is unknown, it is not possible to know which the prevalent damage mechanism is. Anyway, from the values presented in the curves below it is possible to notice that the biggest damage is undergone at low temperatures and also under lubricated conditions, while work hardening leads to the lowest levels of damage. The prevalent damage mechanism can be discovered through the cutting-to-plasticity ratio, shown in Figure 59 c), and which is going to be explained below.

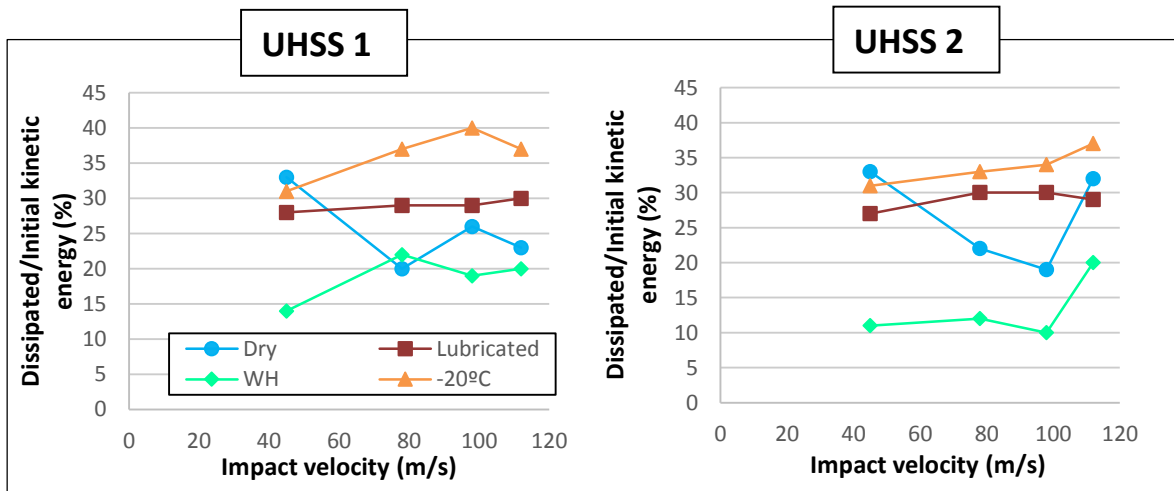


Figure 57. Dissipated/Initial kinetic energy ratio as a function of impact velocity. UHSS 1 left, UHSS 2 right.

Figure 58 shows the main results regarding the wear behavior of the materials. Figure 58 a) demonstrates that impact velocity has a strong influence on volume loss. Regardless of material or test conditions, wear increases proportionally to about the square of the impact velocity, a result that has been also reported by Finnie et al. [21]. Similar results were found by Lindroos et al. [3], while studying impact wear on wear resistant steels under high velocity single impacts for different impact angles. The differences in volume loss become more significant as impact velocity increases.

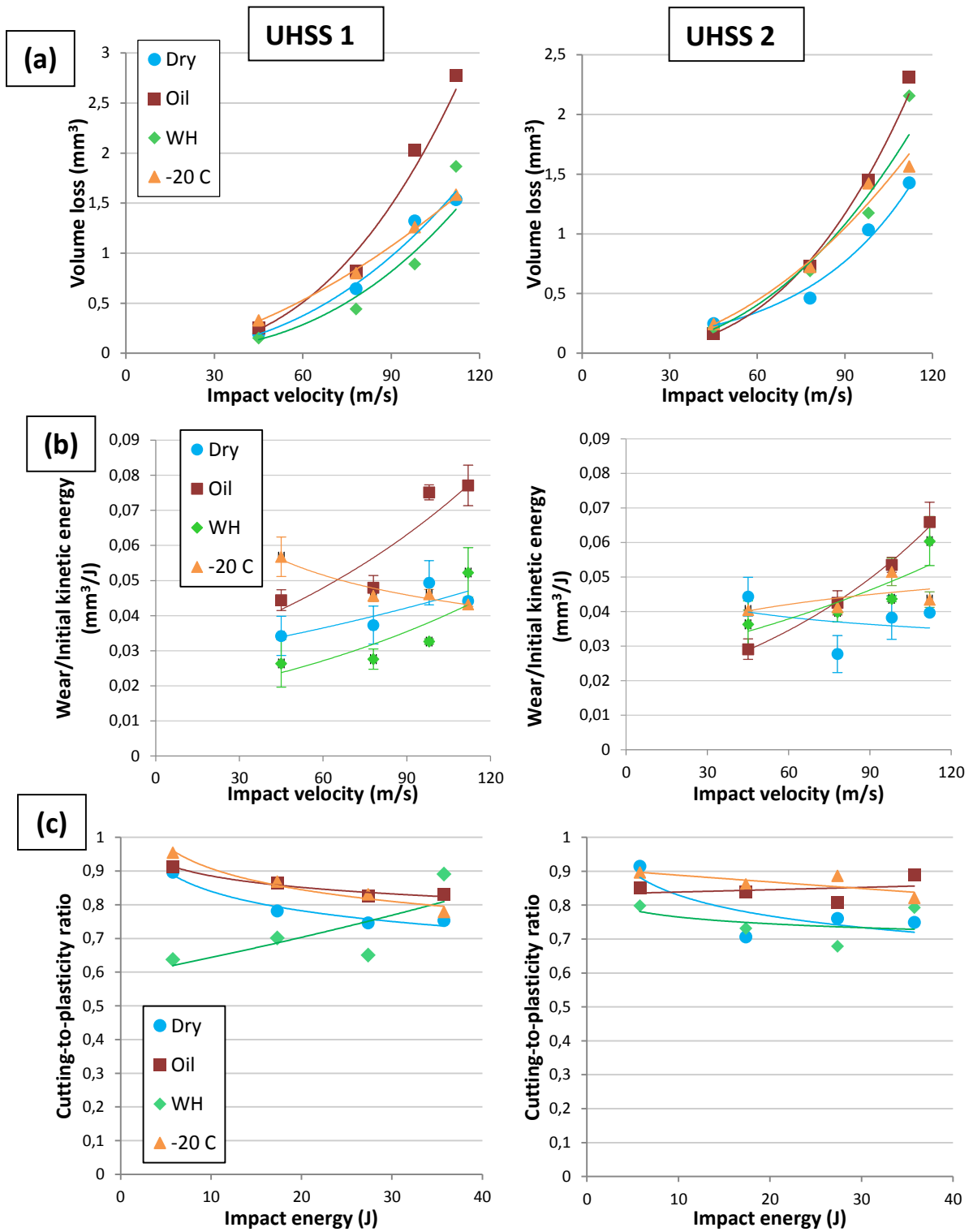


Figure 58. Wear results: a) Volume loss at different impact velocities and test conditions. b) Wear rate as volume loss per initial kinetic energy at different impact energies and test conditions. c) Cutting-to-plasticity ratio at different impact energies and test conditions

Against expected, volume loss is remarkably higher when an oil layer is placed on the target surface. Lubrication reduces friction in the contact projectile-target material, therefore less material is plastically deformed and displaced laterally and to the front of the ball. However, the oil layer does not prevent the material to be cut-off from the surface, leading to higher volume losses. The three-dimensional profiles of the crater formed on UHSS 1 at dry (a) and oil (b) conditions are presented in Figure 59. As mentioned, the amount of material deformed around the crater is higher in dry conditions. Also the height of the pile-up is larger than for the lubricated crater, which could mean that more material was removed from the surface in the second case. For lubricated tests, as the velocity increases, the ratio wear per unit incident energy increases also quite drastically. For the rest of cases this ratio is shown to be not affected by the impact velocity, since the curves are nearly flat. The cutting-to-plasticity ratio, shown in Figure 58 c), is somewhat higher for lubricated testing, which also implies that most of the material is removed from the surface instead of plastically deformed. As mentioned, likely the oil layer protects the surface from plastic deformation but not from cracking and losing material, which leads to larger wear rates.

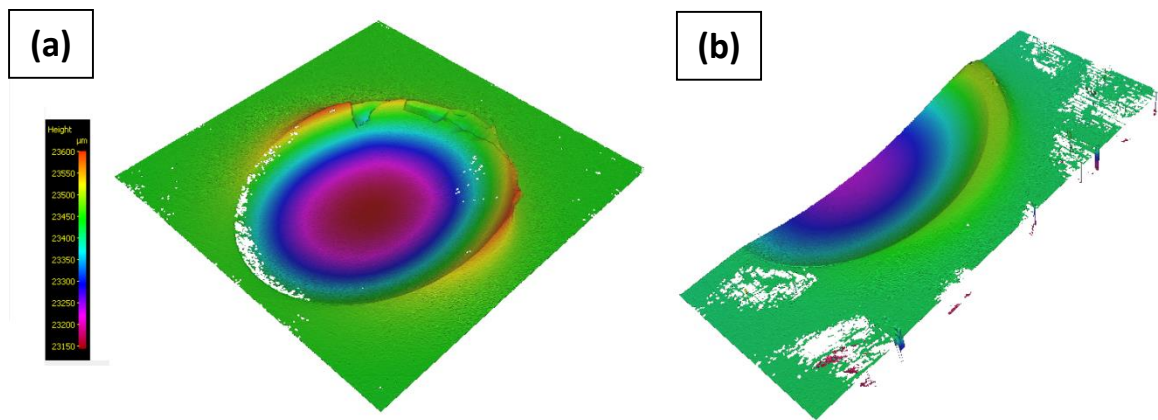


Figure 59. Three dimensional images of the craters obtained for (a) dry and (b) lubricated testing conditions in UHSS 1.

When testing at subzero temperatures, it was found that UHSS 1 is not strongly influenced by the changes of temperature in the range from 0 to -20°C , since the volume loss is nearly the same for both temperatures. On the other hand, for UHSS 2 volume loss is somewhat higher at the low temperature. However, for both materials, higher values of the cutting-to-plasticity ratio at -20°C lead to the conclusion that more material was cut off from the surface than plastically deformed. According to Hurlich [58], metals and alloys with a BCC

structure undergo a marked decrease in ductility as temperature decreases. As the material becomes more brittle, less material deforms plastically and more is cut-off from the surface. Moreover, at a given temperature a metal can be ductile under static loading but brittle when tested under impact conditions.

Increase in hardening of about 45 % (20 000 cycles) prior to tests does not lead to significant improvements in wear rate, since the results are similar than in the case of dry-impact conditions. Zum-Gahr [6], found that an increase in hardness of steels does not lead to a noticeable decrease on wear. He explained this phenomenon as the consequence of the reduction of the capability of deformation of the material, as a result of the previous work hardening. Figure 58 b) shows that at lower velocities the ratio wear/initial kinetic energy is practically independent of impact velocity, but the highest impact velocity results in an increase. The same tendency can be found on Figure 58 c) for the cutting-to-plasticity ratio. There are a few reasons that can explain this behavior. As mentioned before, work hardening reduces the deformation capability. Lower impact velocities do not require high deformation, so the material is able to plastically deform avoiding the removal of a large amount of material from the surface. However, for higher velocities the deformation capability is not enough, leading to higher volume losses. Another possible explanation is related to the thickness of the work hardened layer of the surface. At the highest velocities the depth of the formed craters is about 300 micrometers. Since the work hardening process only affects about 200 micrometers below the surface, impacts at higher velocities reach the bulk material, which has noticeable lower hardness. As a result, volume loss is similar than at dry conditions or even higher due to the microcracks that can appear on the surface as a result of the work hardening process. Additionally, and according to the cutting-to-plasticity ratio, work hardening prior to testing results in less material cut-off from the surface than plastically deformed, therefore, in reducing volume loss. This effect is clearly more remarkable for UHSS 1.

In addition, for UHSS 1 different number of work hardening cycles were applied prior to testing at 17 J of impact energy. As mentioned above, the chosen energy for the test is 17 J to assure that the work hardened layer is thick enough. The three different levels of work hardening resulted in increases of hardness of 45, 60 and 80 %, respectively. Figure 60 illustrates the strong influence of the surface hardness on the volume loss per unit initial kinetic energy. An increase in surface hardness leads to a considerable decrease in volume loss per unit incident energy at moderate values of impact energy. Consequently, and as observed in the previous curves presented in Figure 58, work hardening reduces volume loss when impact energy is not very high. However, when impact energy reaches a certain value the wear increases abruptly. This behavior could be explained by the low thickness of the work hardened surface. When impact energy is very high the work hardened surface is

not thick enough, so the resistance against impacts is made by the bulk material, which has lower hardness. Figure 61 shows a comparison of the two dimensional profiles of the craters formed for different surface hardness. As it can be observed also in Figures 55 and 56, the profiles overlap and there is no a clear difference.

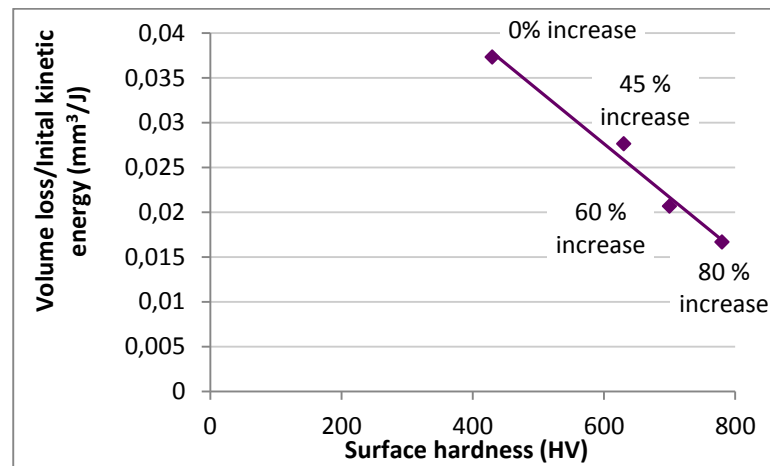


Figure 60. Wear/initial kinetic energy at different levels of work hardening in UHSS 1.

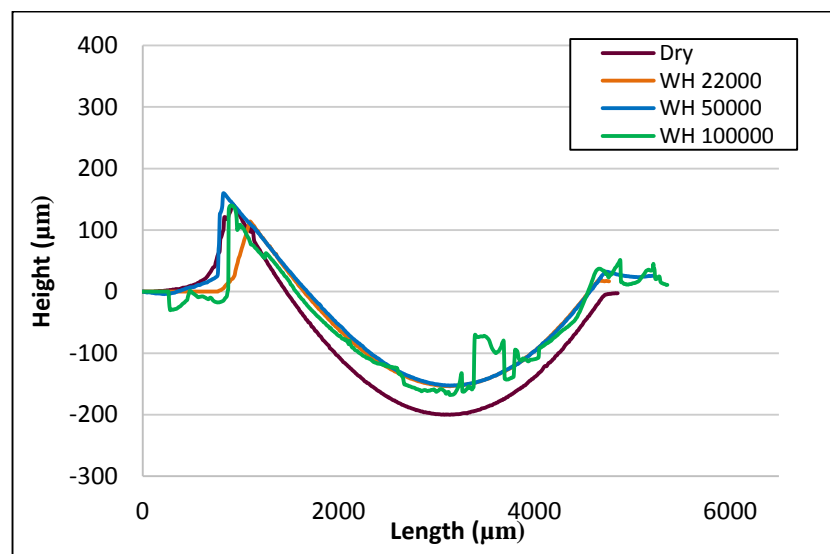


Figure 61. Two dimensional crater profiles of work hardened samples.

7.2. Damage and failure mechanisms

In order to identify the main damage and failure mechanisms the cross sections of some specimens in both types of tests were studied. Also some images were taken using a Scanning Electron Microscope (SEM). Firstly, the results concerning compression testing are presented, followed by the study of the impact craters produced by HVPI testing.

7.2.1. Compression testing

All specimens underwent high amount of plastic deformation at low strain rates. During SHPB testing, UHSS 1 samples did not break, while UHSS 2 samples fractured at higher strain rates, i.e., 2400 and 3600 s^{-1} . The fracture occurred following a line that forms 45° with the axis of the cylindrical specimen, i.e., in the shear direction. When the cross section were studied, numerous adiabatic shear bands were found, examples of which are presented in Figure 62. Transformed ASBs appear white when etched with nital 4 %. The grains following a specific direction indicate the presence of deformed ASBs. Also a white layer appeared following the fracture line. It should be noted that the test duration (pulse length) may not have been long enough at 700 and 1100 s^{-1} to cause deformation up to fracture.

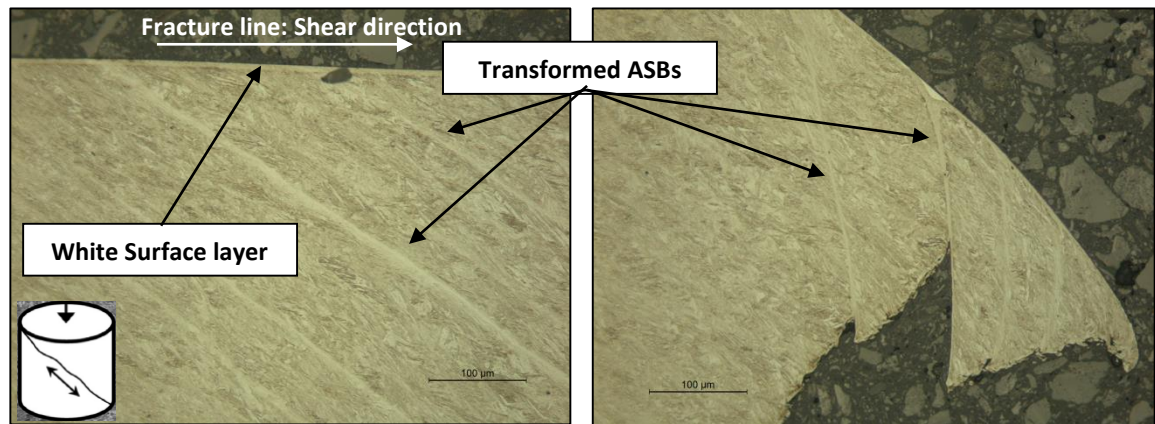


Figure 62. Cross section of SHPB specimen of UHSS 2 tested at a strain rate of 3600 s^{-1} .

Table 13 contains the average of hardness values measured in the cross sections for both materials tested at 3600 s^{-1} strain rate. The high levels of deformation resulted in a noticeable increase of the hardness of the material. Deformed material (DM) has an increase in hardness of about 75 % with respect to the original (BM). The changes in the hardness along the cross section can be observed in Figure 63. Several microhardness measurements were performed in the cross section of UHSS 2. It is worth to notice that hardness within the TASBs is clearly higher.

Table 13. Hardness measured in the cross section of SHPB samples tested at a strain rate of 3600 s^{-1} .

	Average hardness (HV)	Increase (%)	Hardness White Layer (HV)
UHSS 1	750	75	-
UHSS 2	780	75	820

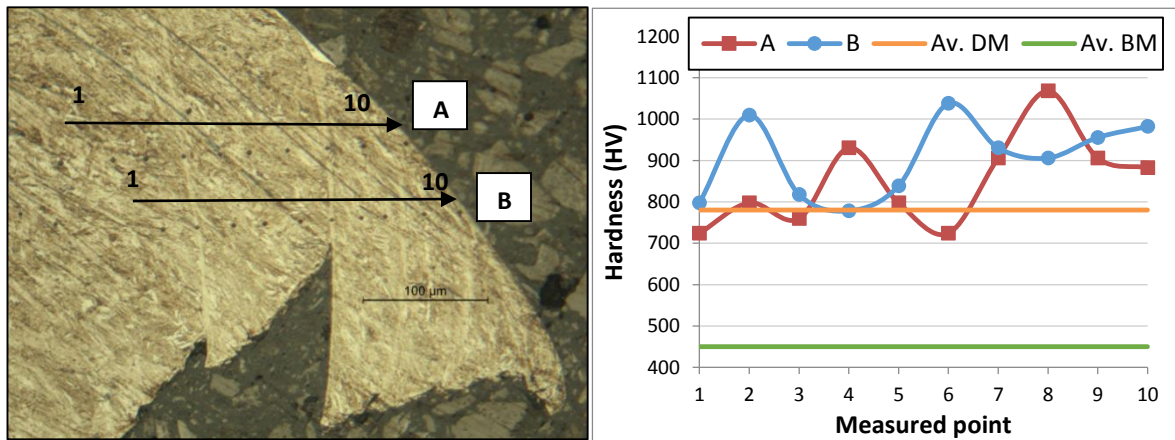
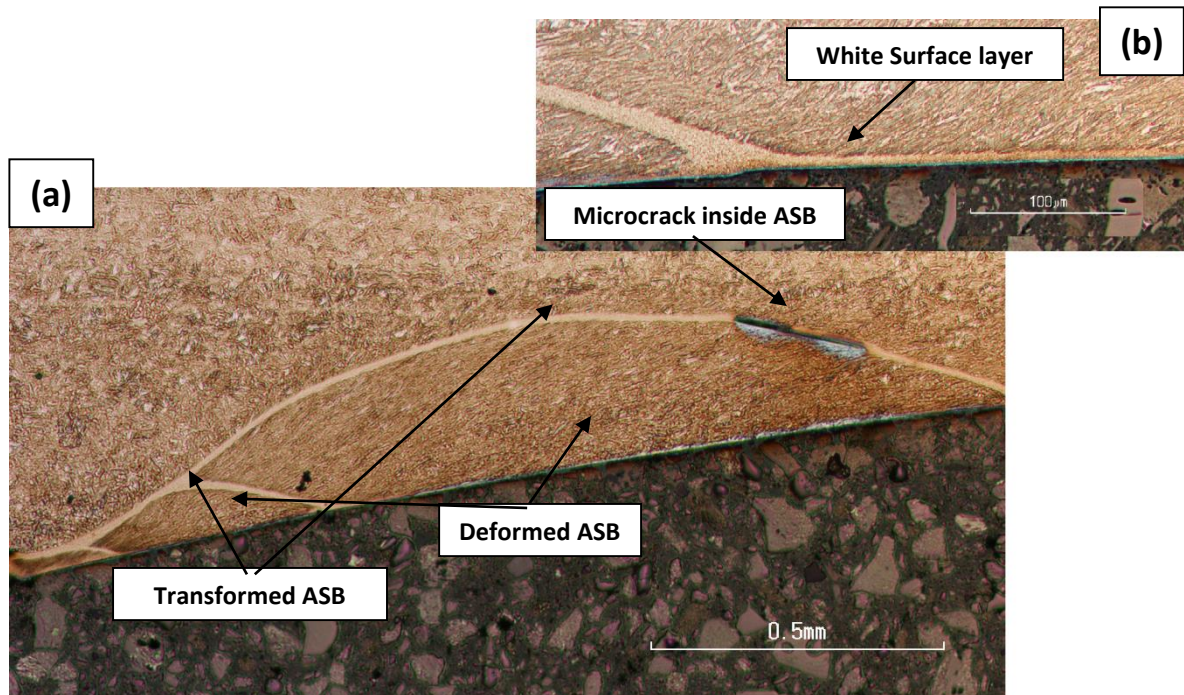


Figure 63. Evolution of hardness along the cross section of UHSS 2 specimen tested at 3600 s^{-1} .

7.2.2. Impact testing. Cross-sectional study

Different damage mechanisms were found when studying the cross sections after a 30° oblique impact. A pile-up appears in all samples and it is formed as a result of the high deformation. Occasionally, part of the deformed material of the pile-up can be cut-off by the projectile while leaving the surface. The pile-up region has experienced a very strong shear deformation, leading to the formation of adiabatic shear bands. Figure 64 a) shows the usual appearance of the ASBs. As it can be seen in Figure 64 c), both types of ASB,

deformed and transformed, are present in the pile-up region. Similar behavior was observed in also other samples. As mentioned in Section 3.2, transformed ASB appeared white when etched, while deformed shear bands are detected by the heavy grain reorientation following the shear stress direction. Some microcracks have started to arise within the transformed ASB (Figure 64 d). After multiple impacts those microcracks may grow, leading to the fragmentation of the material following the ASB direction. Sometimes the fragmentation starts to occur even with a single impact, as shown in Figure 64 e). Therefore, formation of shear bands may result in higher wear rates. Additionally, Figure 64 b) demonstrates the appearance of a thin white layer on the surface following the outline of the crater. Finally, the grains along the crater are oriented following impact direction, as illustrated in Figure 64 f). Similar damage mechanisms were found by Lindroos et al. [3]. However, in the current tests subsurface cracks at various depths were not found in contrast to their findings. Even though the above discussed damage mechanisms are present in both materials, their presence is less evident in UHSS 1, in which shear bands appear shorter and less branched. It is also worth to mention that shear bands are less visible in tests performed in lubricated and low temperature conditions, being non-existent in UHSS1. The oil layer placed in the interface between projectile and target material reduces friction in the contact area and, therefore, the shear stress, which is responsible for the ASB formation. However, lubricated samples show a smaller pile-up region, leading to the conclusion that more material was cut-off from the surface. Pile-up regions also were found to be smaller for sub-zero temperature tests, in which more material was cut-off due to decrease in the ductility.



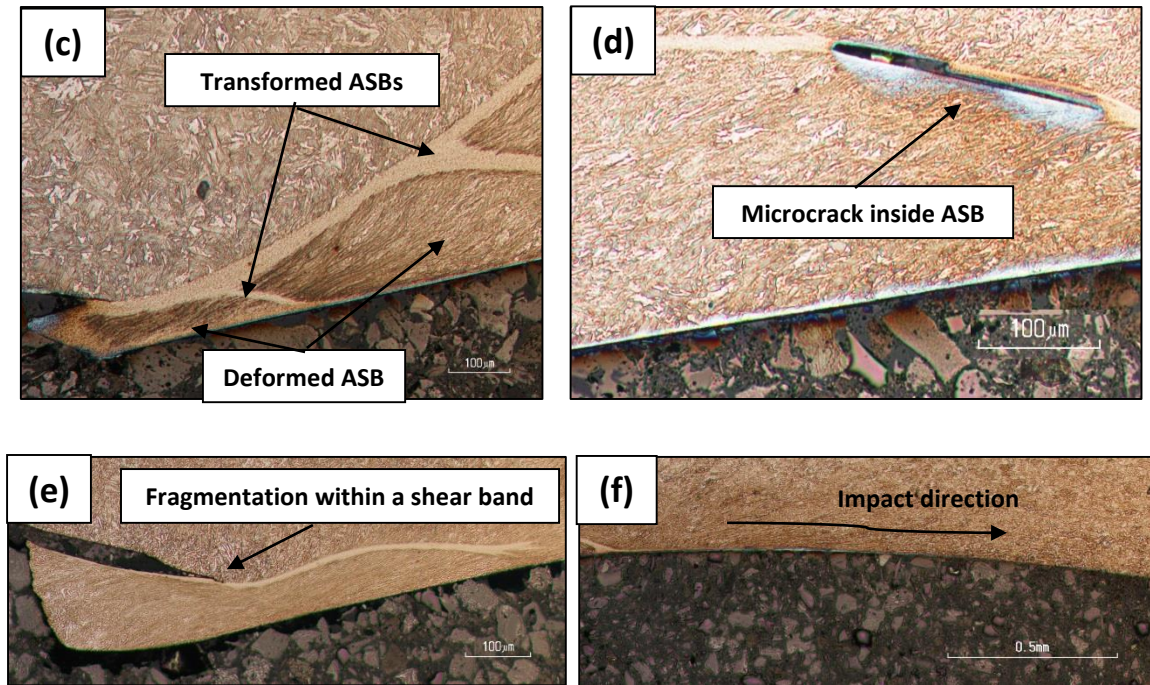


Figure 64. Damage mechanism identified in the cross section of UHSS after oblique impact. (a) Adiabatic shear bands (b) detail of the white surface layer (c) detail of transformed and deformed ASB (d) detail of the microcracks inside a TASB (e) fragmentation within a TASB (f) detail of a deformed ASB

Regarding the microstructure, also grain size and distribution undergo some changes after the impact. Figure 65 show the differences between the microstructure of the bulk material (image a) and that of the material surrounding the impact crater (image b). Due to formation of a deformed ASB the grain structure becomes finer and oriented, resulting in thinner and lengthened grains that clearly follow the shear stress direction.

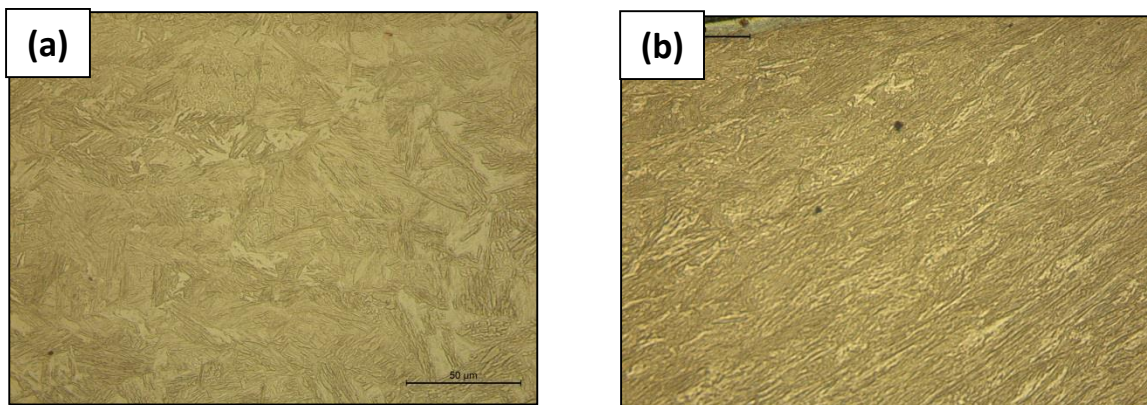
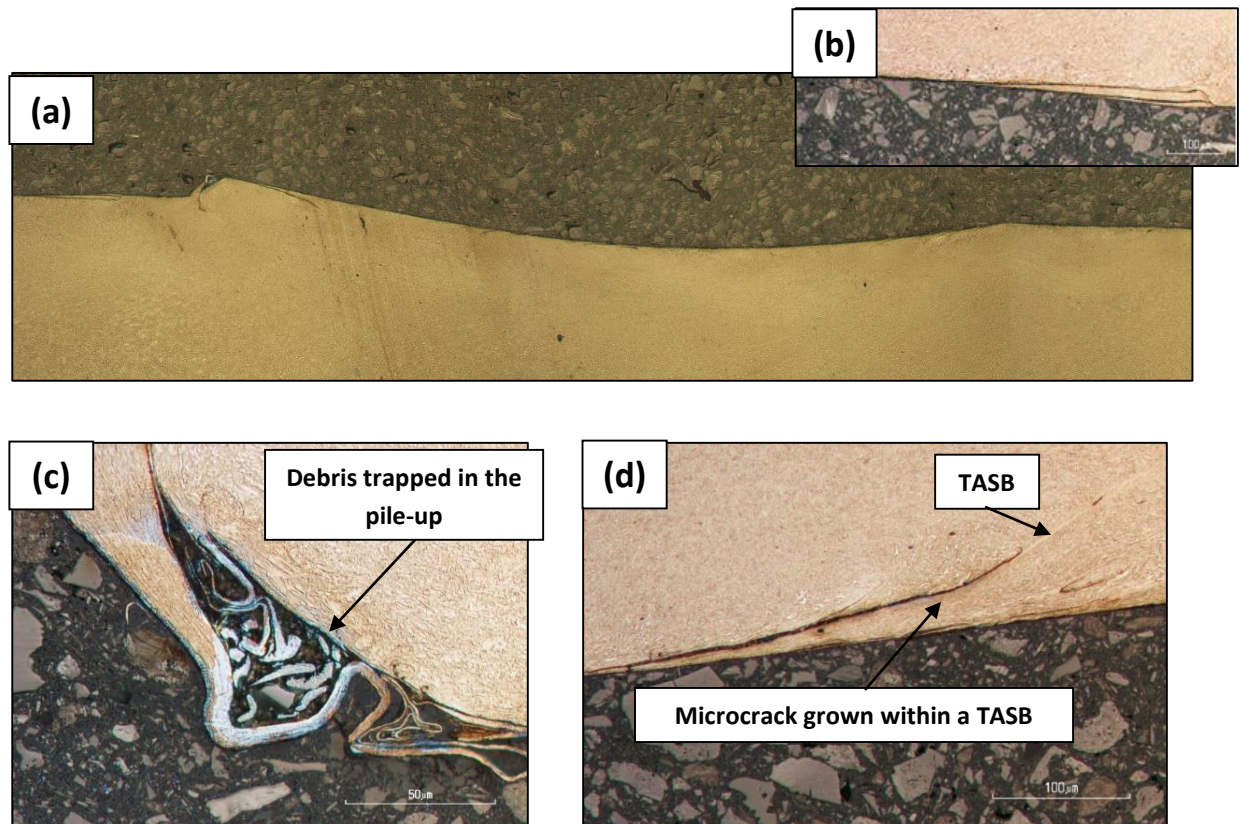


Figure 65. Microstructure of UHSS 2 before (a) and after (b) the impact.

Regarding the work hardening made prior to impact testing, some interesting results have been found as well. Samples work hardened with 20 000 cycles (45% increase on hardness) present similar behavior than the original material. However, as the number of work hardening cycles increases the damage mechanisms change. ASBs are narrower and shorter when hardness is increased up to 60 and 80 %, leading to lower wear rates, as was shown before in Figure 59. Figure 66 a) shows the complete cross section of the impact crater formed on the specimen with 80 % of hardness increase. Based on the inspection of the cross section, transformed shear bands are more common than deformed. Figure 66 d) shows a crack growing within a shear band. In contrast, deformed shear bands cannot be easily found. As a difference to non-hardened specimens, some microcracks start to appear along the outline of the crater as it can be observed in Figure 66 e) and Figure 66 f), which show the bottom and the entrance part of the crater, respectively. Some debris, resulting from the previous work hardening, is trapped on the exit part of the pile-up and also all along the surface of the material, as shown in Figure 66 c) and Figure 66 b), respectively.



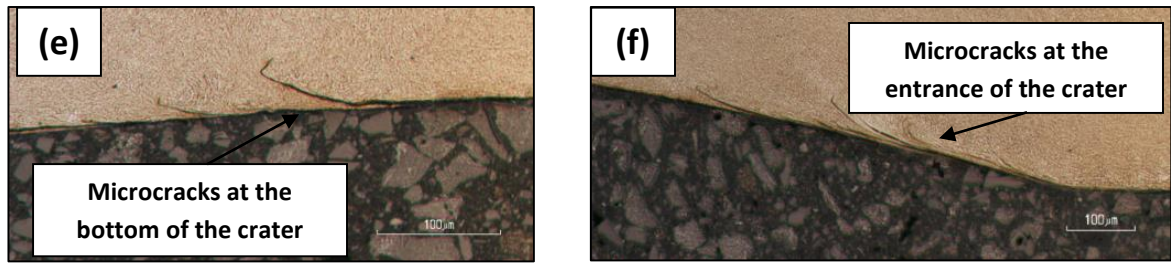


Figure 66. Two dimensional image of the crater formed after the impact on a sample with 80 % enhanced hardness. (a) Complete impact crater (b) debris trapped on the surface outside the crater (c) debris trapped in the pile-up (d) detail of a TASB (e) microcracks at the bottom of the crater (f) microcracks at the entrance of the crater

Figure 67 shows the results regarding the microhardness measurements performed on the cross sections after an impact in dry conditions. Several measuring points have been made along the cross section to get the evolution of the hardness as a function of the depth. In that way it is possible to observe how hardness varies within transformed (TASB) and deformed shear bands (DASB), white surface layers (WSL) and the deformed matrix (DM). As a reference, also the bulk material (BM) hardness is represented in the graphic. The average hardness of the shear bands and the white layer (referred to as Av. in Figure 67) were obtained measuring 5 extra points within them. Table 14 shows the mean microhardness values in the different regions. For UHSS 1 hardness within the transformed shear bands has increased 95% with respect to that of the bulk material, while for UHSS 2 the hardening is around 60 %. That difference in the hardening could be related to the amount of retained austenite and untempered martensite present in the microstructures. Deformed shear bands also result in hardening of the material, but considerably lower than transformed ASB. The white layer formed on the outline of the crater has less hardness than the interior shear bands, likely due to different process of heat transfer and also to different shear stresses. The interior adiabatic shear bands undergo larger shear stresses and cooling rate due to the surrounding material. Finally, below the white bands there is still an affected part of the material, so-called “deformed matrix” that extends to about 300 micrometers underneath.

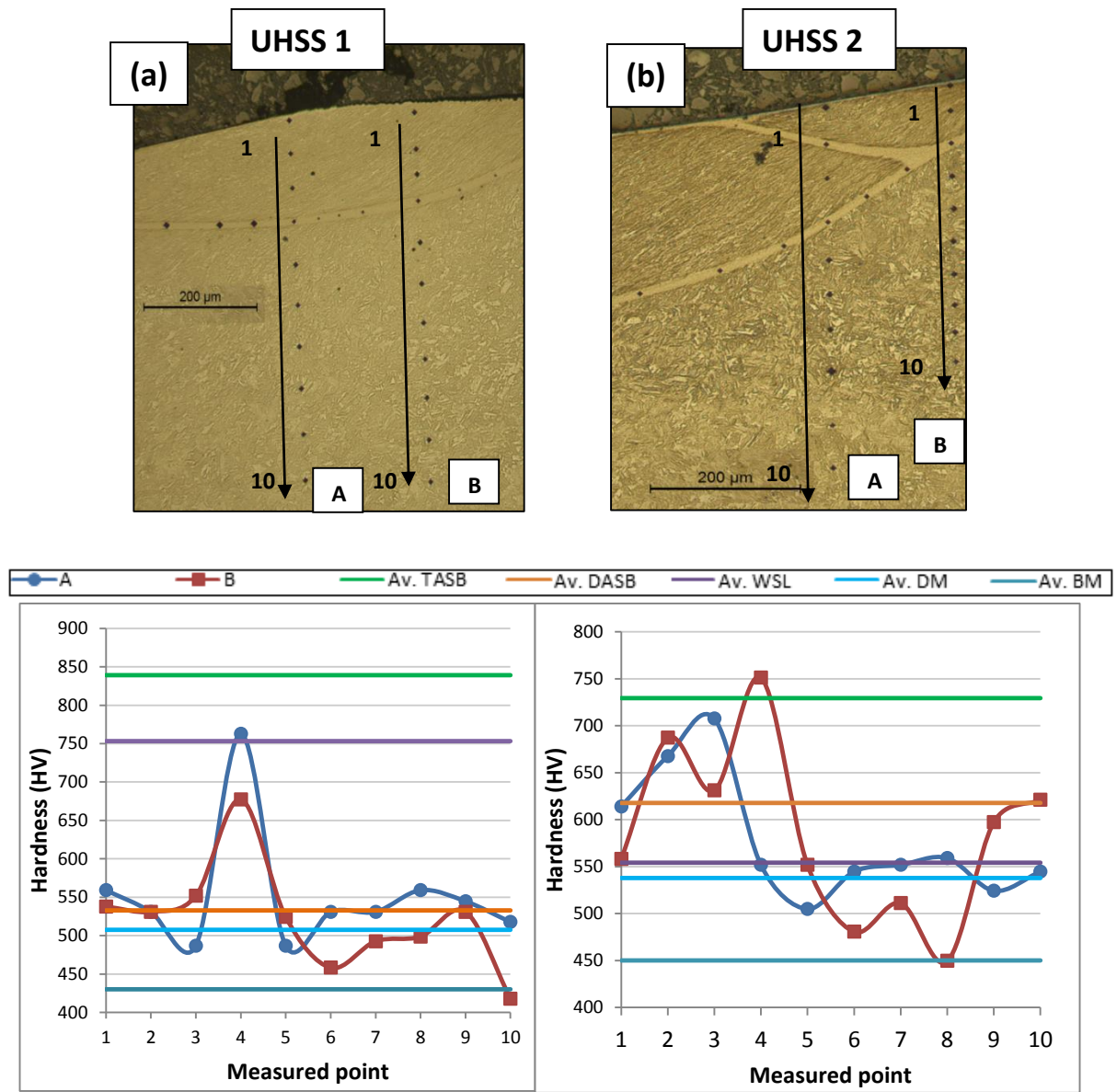


Figure 67. Cross sectional microhardness measurements from the transformed and deformed ASB, white layer and deformed material in UHSS 1 (a) and UHSS 2 (b) produced by an impact in dry conditions.

Table 14. Mean measured microhardness in each region of the cross section and its increase compared to bulk material hardness.

	TASB		DASB		DM		WSL	
	Hardness (HV)	Increase (%)	Hardness (HV)	Increase (%)	Hardness (HV)	Increase (%)	Hardness (HV)	Increase (%)
UHSS 1	840	95	530	25	505	18		
UHSS 2	730	60	620	35	540	20	555	25

7.2.3. Impact testing. Crater three-dimensional study

A more detailed study of the impact craters was conducted using a Scanning Electron Microscope (SEM). Figure 68 shows the pile-up region of the crater formed at different testing conditions in tests performed at the impact velocity of 112 m/s. In all cases cracks appear on the pile-up region. The cracks are greater for dry impacts and also quite noticeable for work hardened specimens, and subzero tested samples. On the other hand, cracks are imperceptible or even nonexistent when lubrication was present. However, while cracks formed during dry impacts are about 700 μm of length and 100 μm of width, cracks formed on samples with enhanced hardness are shorter and wider. In some samples there were also some cracks present on the bottom part of the crater.

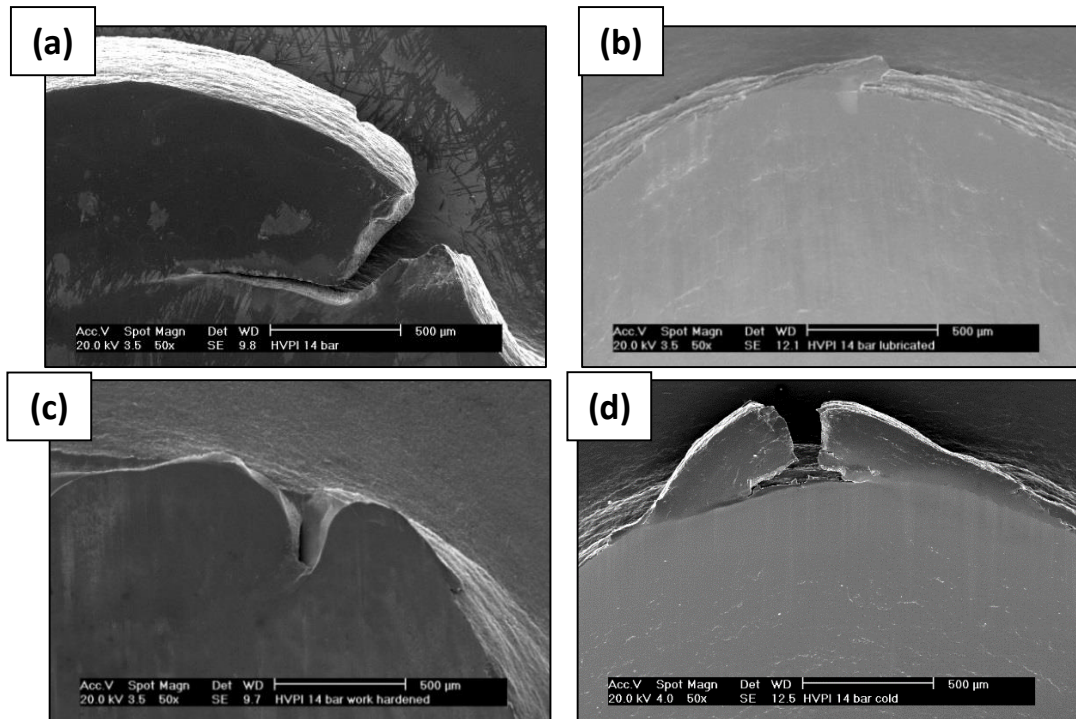


Figure 68. SEM images of the pile-up region for different test conditions: (a) dry (b) lubricated (c) work hardened (d) low temperature.

Figure 69 shows detailed images of the fractures. On one hand, regardless of the surface hardness, fractures on samples tested without lubrication were found to be ductile (Figure 69 a and b) although they show a more brittle character at -20°C of temperature. Those cracks had likely grown within the adiabatic shear bands that were identified on the cross section. On the other hand, as Figure 69 (c) represents, lubricated samples show fracture with a more brittle character and it is possible to observe how some material has been

removed from the upper part of the pile-up region. Finally, Figure 69 (e) and (f) show the surface cracking at the end of a crack formed in a work hardened sample. This surface cracking may form as a result of the previous work hardening.

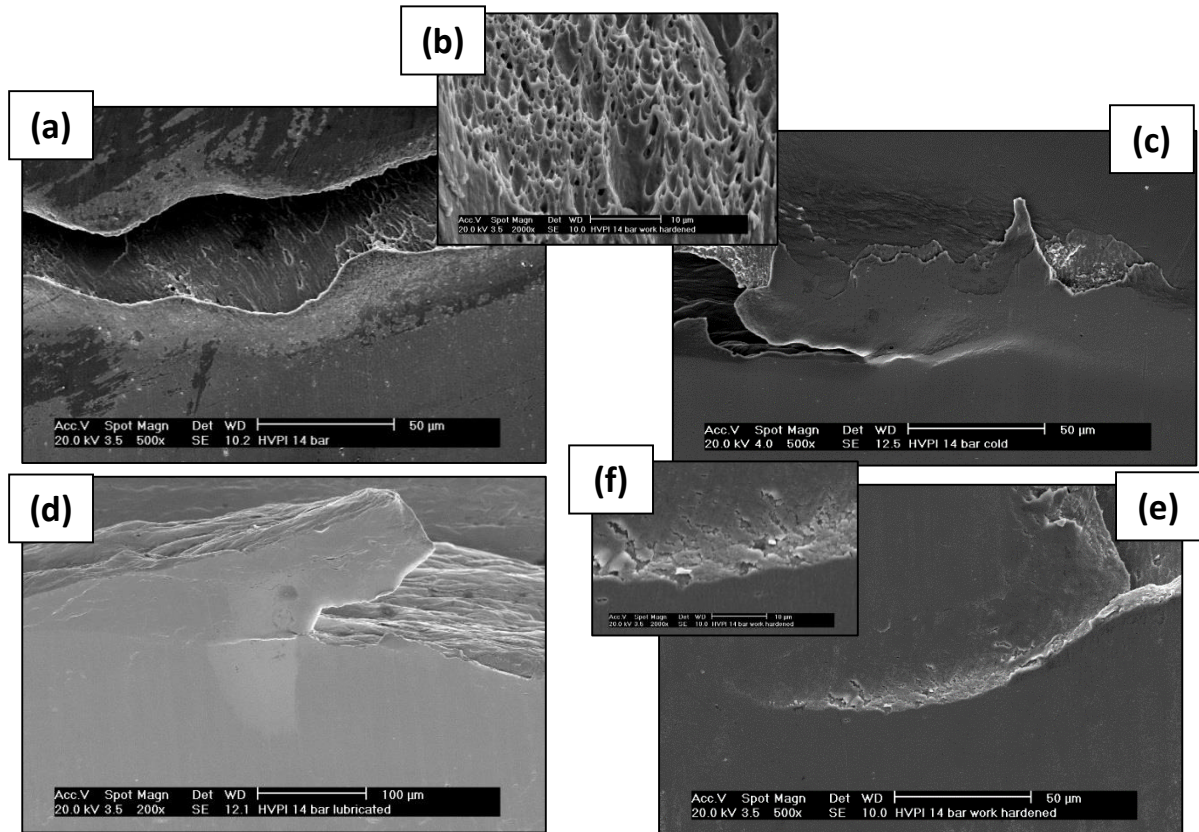


Figure 69. Detail of fracture cracks at different impact conditions. (a) dry impact (b) detail of ductile fracture (c) low temperature impact (d) lubricated impact (e) work hardened impact (f) detail of fracture formed on WH sample

Also the bottom of the crater shows different behavior at different testing conditions. While the surface of the samples tested in “normal” conditions, i.e., at room temperature, without lubrication and not work hardened, does not exhibit any kind of marks, some marks appear in the other cases (Figure 70). In lubricated samples some marks were formed and they are randomly distributed, as shown in Figure 70 a). They were likely formed as the result of the plastic deformation created on the surface as a result of the impact. After the impact, on the bottom of the crater of previously work hardened samples (Figure 70 b), the surface appears also deformed and the marks resulting from the previous work hardening were partially covered as a result of the deformation and material dragging. Also some marks caused by the friction on the interface ball-target surface can be observed. Finally, samples

tested at subzero conditions exhibit some marks on the bottom of the crater (Figure 70 c) that may have been formed as a result of the opening of the grain boundaries.

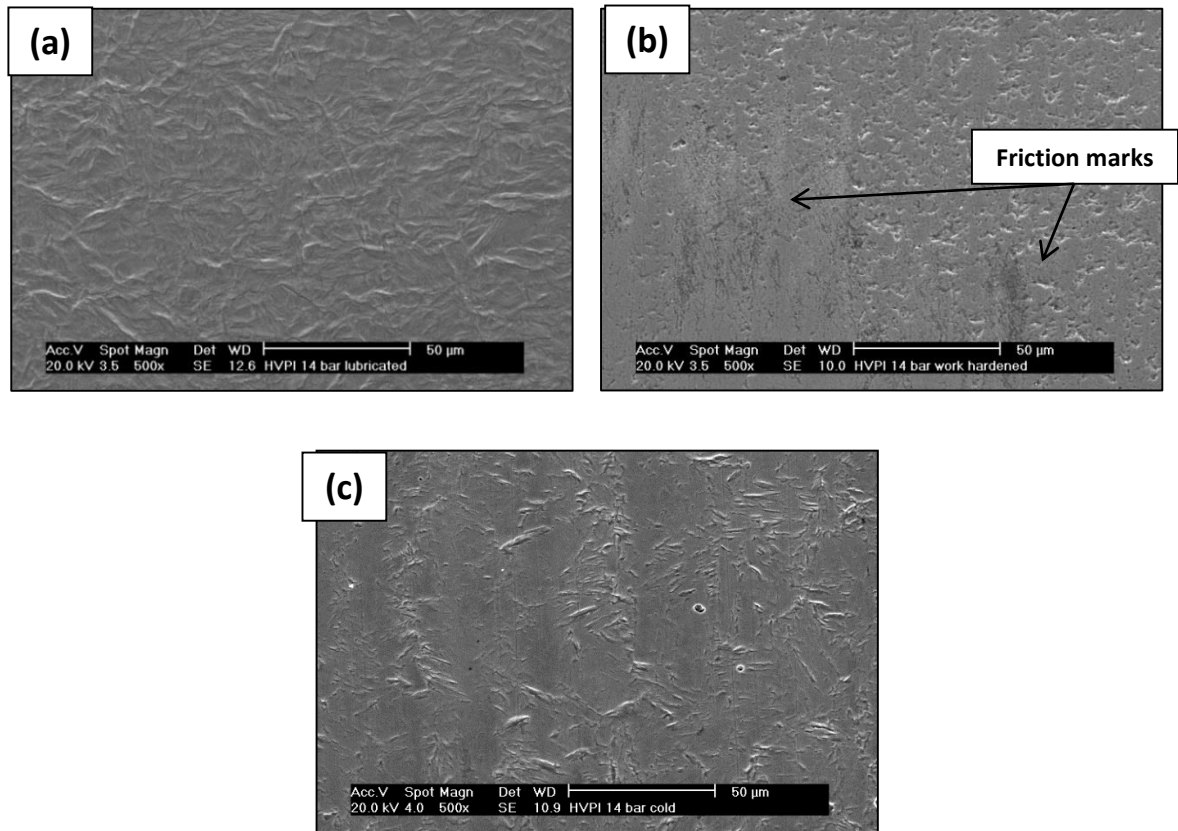


Figure 70. Marks on the bottom of the crater on (a) a lubricated sample (b) a work hardened sample (c) low temperature sample

8. CONCLUSIONS

Experimental testing and characterization was performed on two Ultra High Strength Steels. Their mechanical behavior was studied at different strain rates, ranging from 10^{-3} to 3600 s^{-1} . As the main part of the thesis, both materials were tested with high velocity impacts to characterize their impact wear resistance and related damage mechanisms. All tests were performed with four different impact energies, but at a fixed impact angle of 30° . To simulate real working situations, four different testing conditions, i.e., dry, lubricated, previous work hardening and low temperature, were used. An analysis of the impact craters and cross sections was made in order to identify the impact wear behavior and features of the inflicted damage. Based on the results, the following conclusions can be drawn:

Within the quasi-static region, ranging from 10^{-3} to 1 s^{-1} , both UHSS show clear strain hardening. Strain hardening effect is more remarkable for UHSS 2 and it decreases as the strain rate increases. Despite the general strain hardening tendency, UHSS 1 exhibits slight strain softening for strains lower than 5%.

Concerning the dynamic range of testing, as strain rate increases, the values of stress also increase. However, a strong strain rate softening appears for strains higher than about 15-20 %. This behavior can be explained by material heating and the appearance of adiabatic shear bands. Even though there is a clear dependence of strength on the strain rate, its effect is not very strong since the difference of the yield strength at 10^{-3} and 3600 s^{-1} is only of about 10 %. Higher strain rates have a larger influence on the flow stress.

An investigation of the cross sections of samples tested at the strain rate of 3600 s^{-1} show that both materials undergo an increase in hardness of about 75 % as a result of the large deformation (up to 40%). Also numerous adiabatic shear bands and a white layer on the surface were identified. UHSS 2 samples broke following the shear direction, likely due to cracks that grew within the white layer located on the fracture surface.

Dissipated energy in the impact tests was found to be strongly dependent on test conditions, but not on the material. Higher values of the ratio dissipated/initial kinetic energy found for lubricated conditions lead to the conclusion that more pronounced wear damage is produced under this condition. On the other hand, the lowest values of the ratio were found for the work hardened specimens. The dissipated energy produces damage on

the material in two ways, cutting-off material from the surface and generating plastic deformation. The amount of energy producing each kind of damage is cannot, however, be determined based on the current results.

Volume loss was found to be higher under lubricated conditions than during dry-impact testing. Also higher values for the cutting-to-plasticity ratio were found, leading to the conclusion that more material is removed from the surface than plastically deformed. The oil layer placed on the surface reduces the friction in the interface projectile-target material, therefore less material is deformed plastically and displaced by the projectile. However, the oil layer does not appear to prevent the material to be cut-off from the surface, leading to higher volume losses.

Subzero temperatures were found to have stronger influence on UHSS 2 than on UHSS 1 since for the first material volume losses are higher. For both materials, higher values of the cutting-to-plasticity ratio were found, leading to the conclusion that more material was cut off from the surface than plastically deformed. Decrease in ductility as temperature decreases could explain the higher amount of material removed from the surface.

Work hardening was performed pressing the surface with a 3 kN force for 20000, 50000 and 100000 cycles. The increase in hardness was found to be of 45, 60 and 80 %, respectively for UHSS 1. Work hardening prior to testing was found to reduce volume loss. The higher is the hardness produced on the surface as a result of the previous work hardening, the lower is the wear rate caused. However, for the highest impact velocity the volume loss becomes higher than in the original material, since the thickness of the work hardened layer is only about 200 micrometers and the crater formed at that velocity is deeper. Also the presence of microcracks on the surface as a result of the work hardening can lead to higher wear rates at higher impact velocities.

Adiabatic shear bands (ASB) were identified as the main damage mechanism on the samples of high velocity impact testing. Both transformed (TASB) and deformed (DASB) adiabatic shear bands were found, and they apperared primarily in the pile-up region of the crater. However, their presence is more remarkable in UHSS 2, in which ASBs are longer and more branched. Within the TASBs some microcracks were found growing following their direction. Additionally, in some samples a thin white surface layer (WSL) appeared following the outline of the crater. The hardness of the ASBs, the white layer and the deformed material was measured and compared to that of the bulk material. Hardness within TASBs was found to be almost double than in the bulk material for UHSS 1, while for UHSS 2 the hardness is 60 % higher than in the original material. DASBs and WSLs show an increase in

hardness ranging from 25 to 35 %. The so-called deformed material constitutes the transition zone and shows a hardness increase of about 20 %. The difference in the hardness developed within each region could be related to the different stress states and the different cooling rates at different depths of the material.

As the level of work hardening increases, the appearance of shear bands decreases. DASBs were not present to a considerable extent in the samples with 60 and 80 % increase in hardness. Also TASBs are less remarkable than in other cases, but they are still visible and with larger microcracks growing within them. Higher levels of work hardening result in the formation of microcracks all along the outline of the crater. Finally, some debris resulting from the work hardening process itself was found to be trapped on the surface and on the exit part of the pile-up region.

SEM images of the impact crater show that cracks appear on the pile-up region of the samples tested in dry conditions, regardless of the surface hardness. When lubrication is applied only small cracks can be observed. While the nature of the fractures in dry conditions is ductile, lubricated samples exhibit a more brittle fracture and it is possible to observe that material was removed from the top part of the pile-up region. Low temperatures, however, lead to ductile fracture that exhibits some brittle fracture features.

Based on this study, natural steps in the future would be to extend the conditions for HVPI testing and increase their control. Regarding lubricated tests, in this study the thickness of the oil layer was not taken into account. A step forward would be to control this parameter in order to find the relationship between the oil layer thickness and the impact wear rate. Another interesting feature would be extending the range of tested temperatures from about +200 to -100 °C to establish a relationship between temperature and impact wear. It would then be necessary to design a device that allows cooling and heating the sample directly at the HVPI device. With this new design, it would be possible to control the testing temperature more accurately. Regarding work hardening prior to testing, it was found in this study that it leads to reduced wear loss at low impact velocities. Therefore it would be very interesting to determine a level of work hardening that could lead to lower wear rates also for the highest impact velocities. Finally, only single impacts at one impact angle (30°C) were performed in this study. However, in real working conditions the material undergoes a high number of impacts in multiple directions. The study of the influence of different angles in multiple impact testing would lead to a better understanding of the behavior of the materials in their real applications.

9. REFERENCES

- [1] P. P. Suikkanen, J. I. Kömi, Microstructure, Properties and Design of Direct Quenched Structural Steels, *Science Forum*. 783-786, 2014.
- [2] V. Ratia, I. Miettunen, V-T. Kuokkala, "Surface deformation of steels in impact-abrasion: the effect of sample angle and test duration," *Wear*, vol. 301, pp. 94-101, 2013.
- [3] M. Lindroos, M. Apostol, V.-L. Kuokkala, A. Laukkanen, K. Valtonen, K. Holmberg, O. Oja, "Experimental study on the behavior of wear resistant steels under high velocity single particle impacts," *International Journal of Impact Engineering*, vol. 78, pp. 114-127, 2015.
- [4] M. Lindroos, V. Ratia, M. Apostol, K. Valtonen, A. Laukkanen, W. Molnar, K. Holmberg, V-T. Kuokkala, "The effect of impact conditions on the wear and deformation behavior of wear resistant steels," *Wear*, Vols. 328-329, pp. 197-205, 2015.
- [5] K. H. Z. Ghar, Microstructure and wear of materials, *Tribology series*, Vol 10, 1987.
- [6] K.-H. S. Gahr, "Wear by hard particles," *Tribology International* Vol 31, pp. 587-596, 1998.
- [7] A. V. Levy, "The solid particle erosion behavior of steels as a function of microstructure," *Wear*, vol. 68, no. 3, pp. 269-287, 1981.
- [8] R. Bellman, A. Levy, "Erosion mechanism in ductile metals," *Wear*, vol. 70, no. 1, pp. 1-27, 1981.
- [9] S. Bahadur, R. Badruddin, "Erodent particle characterization and the effect of particle size and shape on erosion," *Wear*, vol. 138, no. 1-2, pp. 189-208, 1990.
- [10] W. D. Callister, D. G. Rethwisch, Materials Science and Engineering, 2011.
- [11] R. Isaac, A. Granato, "Rate theory of dislocation motion: Thermal activation and inertial effects," *Physical Review B*, 1988.
- [12] M. Apostol, "Strain Rate and Temperature Dependence of the Compression Behavior of FCC and BCC metals. Development of Experimental Techniques and their Application to Materials Modelling," TUT, Tampere, 2007.
- [13] M. Hokka, "Effects of Strain Rate and Temperature on the Mechanical Behavior of Advanced High Strength Steels," TUT, Tampere, 2008.

- [14] S. Curtze, "Characterization of the Dynamic Behavior and Microstructure Evolution of High Strength Sheet Steels," TUT, Tampere, 2009.
- [15] W. S. Lee, C. F. Lin, "Impact properties and microstructure evolution of 304L stainless steel," *Materials Science and Engineering A*, 2001.
- [16] M. C. Meyers, *Dynamic Behavior of Materials*, University of California, p 448-487, 1994.
- [17] K. Kato, K. Adachi, "Wear mechanisms," *Wear*, vol. 203, pp. 291-301, 1997.
- [18] R. E. Winter, I. M. Hutchings, Solid particle erosion studies using single angular particles, *Wear*, Vol 29, 1974.
- [19] R. E. Winter, J. E. Fields, I. M. Hutchings, Solid particle erosion of metals: the removal of surface material by spherical projectiles, 1976.
- [20] J. Williams, *Wear by hard particles*.
- [21] I. Finnie, D. H. Mc Fadden, "On the velocity dependence of the erosion of ductile metals by solid particles at low angles of incidence," *Wear*, vol. 48, pp. 181-190, 1978.
- [22] I. Finnie, J. Wolak, Y. H. Kabil, "Erosion of metals by solid particles," 1967.
- [23] M. Naim, S. Bahadur, "The significance of the erosion parameter and the mechanisms of erosion in single-particle impacts.," *Wear*, vol. 94, pp. 219-232, 1984.
- [24] K. Cho, Y. C. Chi and J. Duffy, *Microscopic Observations of Adiabatic Shear Bands*, Division of Engineering, Brown University Providence, 1988.
- [25] C. Zener, J. H. Hollomon, "Effect of strain rate upon plastic flow of steel," *Journal of Applied Physics*, vol. 15, 1944.
- [26] J. Beatty, L. W. Meyer and Nemat-Nasser, *Shock-Wave and High-Strain-Rate Phenomena in Materials*, New York: Dekker, p 645, 1992.
- [27] F. R. Recht, "Catastrophic thermoplastic shear," *Journal of Applied Mechanics*, vol. 31, pp. 189-193, 1974.
- [28] G. Krauss, *Microstructures, Processing and Properties of Steels. Properties and Selection: Irons, Steels and High-Performance Alloys, Vol 1*, *ASM Handbook*, *ASM International*, 1990.
- [29] T. Ericsson, "Principles of Heat Treating of Steels," *ASM Handbook*, *ASM International*, vol. 4, no. Heat Treating, pp. 3-19, 1991.

- [30] G. Krauss, Physical Metallurgy and Heat Treatment of Steel, *American Society of Metals*, p 28-2 to 28-10, 1985.
- [31] R. A. Flinn and P. K. Trojan, Engineering Materials and their Applications, p 220-223, p 232-233, 1975.
- [32] H. K. D. H. Bhadeshia, Worked examples in the Geometry of Crystals, 1987.
- [33] G. Krauss, Steel: Heat Treatment and Processing Principles, *ASM International*, 1989.
- [34] S. Kalpakjian, Manufacturing Processes for Engineering Materials, *Illinois Institute of Technology*, 1997.
- [35] B. Akhavan, F. Ashrafizadch and A. M. Hassanli, Influence of Retained Austenite on the Mechanical Properties of Low Carbon Martensitic Stainless Steel Castings, *ISIJ International*, Vol 51, p 471-475, 2011.
- [36] Martensitic Structures, Metallography and Microstructures, *ASM Handbook, ASM International*, Vol 9, p 165-178, 2004.
- [37] A. R. Marder, A. O. Benscoter, G. Krauss, Microcracking Sensitivity in Fe-C Plate Martensite, *Metall. Trans.* Vol 1 p 1545-1549, 1970.
- [38] J. P. Materkowski and G. Krauss, Tempered Martensite Embrittlement in SAE 4340 Steel, *Metall. Trans.*, Vol 10A, p 1643-1651, 1979.
- [39] E. P. DeGarmo, J. Temple Black, R. Kohser, Materials and Processes in Manufacturing, 1988.
- [40] G. E. Totten, J. L. Dossett and N. I. Kobasko, Quenching of Steel, Steel Heat Treating Fundamentals and Processes, *ASM Handbook, ASM International*, Vol 4A, p 91-157, 2013.
- [41] A. J. Kaijalainen, P. P. Suikkanen, T- J. Limnell, L. P. Karjalainen, J. I. Kömi, D. A. Porter, Effect of austenite grain on the strength and toughness of direct-quenched martensite, *Journal of alloys and compounds*.
- [42] M. Isakov, "Strain Rate History Effects in a Metastable Austenitic Stainless Steel," TUT, Tampere, 2012.
- [43] S. Nemat-Nasser, Introduction to High Strain Rate Testing, Mechanical Testing and Evaluation, *ASM International, ASM Handbook*, p 427-428, 2000.
- [44] T. Vuoristo, "Effect of Strain Rate on the Deformation Behavior of Dual Phase Steels and Particle Reinforced Polymer Composites," TUT, Tampere, 2004.

- [45] A. Mardoukhi, "High Temperature High Strain Rate Behaviour of Superalloy MA 760," TUT, Tampere, 2013.
- [46] G. T. Gray, "Classic Split Hopkinson Pressure Bar Testing, Mechanical Testing and Evaluation," *ASM Handbook, ASM International*, p 462-476, 2000.
- [47] C. Bacon, "Separation of waves propagating in an elastic or viscoelastic Hopkinson pressure bar with three-dimensional effects.," *International Journal of Impact Engineering*, 22, 199.
- [48] F. Follansbee, C. Frantz, "Wave Propagation in the Split Hopkinson Pressure Bar," *Journal of Engineering Materials and Technology*, 1983.
- [49] D. A. Gorham, "A numerical method for the correction of dispersion in the pressure bar signals," *Journal of Physics E: Scientific Instrument* Vol 16, p 477-479, 1983.
- [50] D. Bancroft, "The velocity of longitudinal waves in cylindrical bars," *Physical Review* Vol 59, p 588-593, 1941.
- [51] L. D. Bertholf, C. H. Karnes, "Two dimensional analysis of the split Hopkinson pressure bar system," *Journal of the Mechanics and Physics of Solids* Vol 23, p 1-19, 1975.
- [52] E. D. H. Davies, S. C. Hunter, "The dynamic compression testing of solids by the method of the split Hopkinson pressure bar," *Journal of the Mechanics and Physics of Solids* Vol 11 p 155-179, 1963.
- [53] D. A. Gorham, "Specimen inertia in high strain-rate compression," *Journal of Physics D: Applied Physics* Vol 22, p 1888-1893, 1989.
- [54] J. Z. Malinowski, J. R. Klepaczko, "A unified analytic and numerical approach to specimen behavior in the split-Hopkinson pressure bar," *International Journal of Mechanical Sciences* Vol 28, p 381-391, 1986.
- [55] M. Apostol, "High velocity impactor - modeling and experimental verification of impact wear tests," Tampere, Finland, 2013.
- [56] M. Hokka, V-T. Kuokkala, P. Siitonen, J. Liimatainen, "Experimental techniques for studying the behavior of wear resistant materials under dynamical gouging and surface fatigue," in *ICEM12-12th International Conference on Experimental Mechanics*, Politecnico de Bari, Italy, 2004.
- [57] R. Madec, B. Devincre, L. P. Kubin, "From Dislocation Junctions to Forest Hardening," *Physical Review Letters*, vol. 89, 2002.

[58] A. Hurlich, "Low temperature metals," *General Dynamics*, no. Astronautics.